Characterization and Modeling of Woven Carbon Fiber Prepreg Plies for Automated Draping Processes

Krogh, Christian

Publication date:
2019

Document Version
Publisher's PDF, also known as Version of record

CHARACTERIZATION AND MODELING OF WOVEN CARBON FIBER PREPREG PLIES FOR AUTOMATED DRAPING PROCESSES

BY
CHRISTIAN KROGH

DISSERTATION SUBMITTED 2019

AALBORG UNIVERSITY
DENMARK

Characterization and Modeling of Woven Carbon Fiber Prepreg Plies for Automated Draping Processes

Christian Krogh

Department of Materials and Production
Solid and Computational Mechanics Research Group
Aalborg University, Denmark

PhD Thesis
2019

Dissertation submitted: October, 2019

PhD supervisor: Johnny Jakobsen, Associate Professor, PhD, M.Sc.
Department of Materials and Production
Aalborg University, Denmark

PhD committee: Jørgen Asbøll Kepler, Associate Professor (chairman)
Aalborg University

Giordano Bellucci, Stress Engineer
Alfa Romeo

Jesper Hattel, Professor
Technical University of Denmark

PhD Series: Faculty of Engineering and Science, Aalborg University

Department: Department of Materials and Production

ISSN (online): 2446-1636
ISBN (online): 978-87-7210-514-7

Published by:
Aalborg University Press
Langagervej 2
DK – 9220 Aalborg Ø
Phone: +45 99407140
aauf@forlag.aau.dk
forlag.aau.dk

Typeset in LaTeX and printed in Denmark by Rosendahls, 2019

Preface

This thesis has been submitted to the Faculty of Engineering and Science at Aalborg University in partial fulfillment of the degree of Doctor of Philosophy in Mechanical Engineering. The work has been carried out at the Department of Materials and Production at Aalborg University in the period from September 2016 to August 2019. This period includes a research stay abroad at the Advanced Composite Materials and Textile Research Laboratory at the University of Massachusetts Lowell, USA from February to July 2018.

The PhD project is part of the research project *FlexDraper - An Intelligent Robot-Vision System for Draping Fiber Plies* which has been funded by the Innovation Fund Denmark under grant number 5163-00003B.

Reader's Guide

The work conducted during the PhD study has been reported in three journal papers and four conference proceedings with the journal papers constituting the main contributions. The thesis takes the form of an extended summary with the journal papers appended.

In Chapter 1, Introduction to Characterization and Modeling of Fabrics, the topic of automated composite draping is introduced and motivated, and some relevant concepts and analysis tools related to modeling and characterization are briefly discussed. Readers already familiar with modeling of composite draping may go through this chapter casually, but are encouraged to visit Sections 1.2 and 1.7 covering a description of the overall research project and the PhD project objectives, respectively. Chapter 2, State-of-the-Art Literature Review, takes the reader through a survey of relevant publications from the scientific literature. Chapter 3, Results and Conclusions of the PhD Project, summarizes the results from the three journal papers, including some unpublished material from the studies. Based on the formulated research questions, an overall conclusion is drawn. Lastly, Chapter 4, Future Work, discusses possible extensions of the work presented, including some preliminary studies that were conducted.

Acknowledgements

There are a number of people to whom I owe my gratitude. My supervisor, Associate Professor Johnny Jakobsen, has been a valuable companion who has offered me his guidance through a fine balance of helping chart the course and letting me maneuver the ship. Jens Glud, who was affiliated with the research project during the first six months, was an esteemed resource who also helped me shape the PhD project.

I would also like to express my sincere gratitude to Professor James A. Sherwood for hosting my research stay at the University of Massachusetts Lowell. I appreciate the efforts he made for making my research stay a success. Together with his PhD student Kari White, we had some great discussions and, not to forget, a pleasant time at the ESAFORM 2019 conference in the Basque Country, Spain.

My colleagues, both at the Solid and Computational Mechanics Research Group at AAU and the Advanced Composite Materials and Textile Research Lab at UMass Lowell, also deserve an acknowledgment for providing an enjoyable working environment. To that end, I greatly appreciate the company of my AAU office mates Jacob Oest and Lasse Ledet. Likewise, I extend my thanks to the other FlexDraper project partners for their support and dedication to the project.

Finally, I am most grateful for the support and care of my family and friends. I value their interest in my project and as well as their commitment during my intricate explanations typically involving napkins or other fabric readily at hand at the dinner table.

Aalborg, August 2019

Christian Krogh

Contents

Abstract

Laminated composites are known for their superior mechanical properties and are increasingly being used, for instance in the aerospace, automotive and sporting goods industries. One major drawback is the cost associated with the manufacturing process. This drawback is especially true for small batch production which, to a wide extent, is based on manual labor. Thus, there is a need for a flexible, automatic system for manufacture of small batch composites.

The FlexDraper research project takes point of departure in the aerospace industry in which fairly simple, low-curvature parts occur frequently. The project considers the draping of entire plies of woven carbon fiber prepreg. The quality control is, however, not simple and the tolerances for misplacements and wrinkles on the mold are very tight. It is therefore crucial to be able to predict such defects before they occur in the robot cell. Further, the development of possible defects must be taken into account when programming the draping robot. To that end, a numerical framework is needed.

The present PhD project considers such a numerical framework. The prepreg material is first characterized experimentally in its major deformation modes: fiber direction tension, in-plane shear and out-of-plane bending. Special emphasis is placed on the shear deformation which is known to be the governing mode of deformation during composite draping. The results from the characterization is used as input for a rate-dependent fabric material model in a nonlinear finite element (FE) context. Together with a model of the mold and the robot tool, a given robot draping sequence can be simulated, and its validity with respect to the quality requirements can be assessed. As an aid in the draping sequence generation, the final configuration of the robot tool on the mold can be predicted using a kinematic draping algorithm. By testing simple draping sequences, it is found that wrinkles and misplacements can easily occur with the robot system, and that a proper choice of draping sequence is crucial to meet the industry requirements.

The issue of selecting a proper draping sequence is addressed by means of a computationally efficient prepreg fabric model used in an optimization framework. By means of the final known robot configuration the optimization framework can generate a draping sequence taking the fabric response in the intermediate steps into account. After validation using the FE model, the generated draping sequence can be implemented on the robot system.

Dansk Resumé

Laminerede kompositter er kendt for deres fortrinlige mekaniske egenskaber og bruges i stigende grad inden for eksempelvis luftfarts-, bil- og sportsudstyrsindustrierne. En betydelig ulempe er fremstillingsprisen. Denne ulempe kommer særligt til udtryk ved produktion af små serier, hvor der ofte anvendes manuel arbejdskraft. Der er derfor et behov for et fleksibelt, automatisk system til fremstilling af kompositter i små styktal.

Forskningsprojektet FlexDraper tager udgangspunkt i luftfartsindustrien, hvor relativt simple emner med svage krumninger ofte forekommer. Der fokuseres på drapering af hele lag af præ-imprægnerede kulfibervæv. Kvalitetskontrollen er dog langt fra simpel, og tolerancerne for nøjagtig placering samt foldedannelse på støbeformen er meget små. Det er derfor helt centralt at kunne forudsige sådanne defekter, før de opstår i robotcellen. Endvidere skal der tages højde for dannelsen af mulige defekter, når draperingsrobotten programmeres. I forlængelse heraf er det fordelagtigt med et numerisk beregningsværktøj.

Dette PhD-projekt omhandler et sådant beregningsværktøj. Kulfibervævet karakteriseres først eksperimentelt, opdelt i de dominerende deformationsmekanismer: træk i fiberretningerne, forskydning i planet og bøjning ud af planet. Der lægges særlig vægt på forskydning, som er kendt som den mest betydningsfulde deformationstilstand under drapering. Resultaterne fra karakteriseringen bruges som input til en materialemodel, som medtager effekterne af varierende deformationshastigheder af materialet. Materialemodellen anvendes i en ikke-lineær finite element (FE) model, som også omfatter en repræsentation af støbeformen og robotværktøjet. FE-modellen muliggør simulering af en given robotdraperingssekvens, hvormed validiteten af sekvensen i forhold til de fremsatte kvalitetskrav kan bedømmes. Som en hjælp til bestemmelse af draperingssekvenser benyttes en kinematisk draperingsalgoritme til beregning af robotværktøjets slutkonfiguration på støbeformen. Ved at teste simple sekvenser bliver det klart, at folder og placeringsunøjagtigheder let kan forekomme under drapering med robotten, og at et korrekt valg af draperingssekvens er altafgørende for at imødekomme kravene fra industrien.

Udfordringen med et korrekt valg af draperingssekvens undersøges ved hjælp af en beregningseffektiv model af kulfibervævet, som benyttes i sammenhæng med et optimeringsprogram. Ved hjælp af den kendte slutkonfigu-

ration for robotværktøjet kan optimeringsprogrammet generere en sekvens, hvor kulfibervævets respons undervejs i processen tages med i beregningerne. Efter validering med FE-modellen kan den genererede sekvens implementeres på robotsystemet.

Publications and Conferences

The following contains a list of the publications produced and the conferences attended during the PhD study.

Primary Publications in Journals

A) Krogh C, Glud JA & Jakobsen J (2019) Modeling the robotic manipulation of woven carbon fiber prepreg plies onto double curved molds: A path-dependent problem. Journal of Composite Materials, 53(15):2149-2164.

B) Krogh C, White KD, Sabato A & Sherwood JA (2019) Picture-frame testing of woven prepreg fabric: An investigation of sample geometry and shear angle acquisition. International Journal of Material Forming, in press.

C) Krogh C, Sherwood JA & Jakobsen J (2019) Generation of Feasible Gripper Trajectories in Automated Composite Draping by means of Optimization. Manuscript submitted.

Primary Publications in Proceedings

D) Krogh C, Glud JA & Jakobsen J (2017, October) Modeling of prepregs during automated draping sequences. In AIP Conference Proceedings (Vol. 1896, No. 1, p. 030036). AIP Publishing.

E) Krogh C & Jakobsen J (2017, October) Modeling of robot draping sequences with prepreg plies. In Proceedings of the 30th Nordic Seminar on Computational Mechanics (pp. 104-107).

F) Krogh C, Jakobsen J & Sherwood JA (2018, September) Development of a Computationally Efficient Fabric Model for Optimization of Gripper Trajectories in Automated Composite Draping. In International Conference on Engineering Optimization (pp. 1107-1118). Springer, Cham.

G) Krogh C, Dangora LM, White KD, Jakobsen J & Sherwood JA (2019, July) 256 shades of gray: Application of image processing to evaluate the effect of sample geometry and constant shear strain rates in the picture-frame test. In AIP Conference Proceedings (Vol. 2113, No. 1, p. 020001). AIP Publishing.

Other Publications

H) Krogh C, Jungersen MH, Lund E & Lindgaard E (2017) Gradient-based selection of cross sections: a novel approach for optimal frame structure design. Structural and Multidisciplinary Optimization, 56(5):959-972.

I) White KD, Krogh C & Sherwood JA (2019, July) Investigation of shear characterization of a UHMWPE unidirectional cross-ply for finite element simulation of composite processing. In AIP Conference Proceedings (Vol. 2113, No. 1, p. 020017). AIP Publishing.

J) Ellekilde L-P, Wilm J, Nielsen OW, Krogh C, Glud JA, Gunnarsson GG, ... & Petersen HG (2018) Design of automated robotic system for draping of prepreg composite fabrics. Manuscript submitted.

Conferences

The conferences with an oral presentation attended during the PhD study are shown in the figure below.

PhD conferences. In column-major order: ESAFORM 2017, Nordic Seminar on Computational Mechanics 2017, EngOpt 2018, DCAMM national symposium 2019 and ESAFORM 2019.

1

Introduction to Characterization and Modeling of Fabrics

> “ “Drape” and “drapability” are terms for that property of textile materials which allows a fabric to orient itself into graceful folds or pleats when acted upon by force of gravity. Hence, a fabric is said to have good draping qualities when the configuration is pleasing to the eye. ”
>
> – Chu et al. (1950)

While a carbon fiber layup certainly can be pleasing to the eye, the introduction of “graceful folds” is highly problematic when manufacturing components for the aerospace industry. Thus, the term *draping* is ambiguous and the meaning depends on whether the context is the garment industry (as with the above quote) or laminated composites which is the focus in this thesis. Nonetheless, both types of applications basically concern fabrics whose behavior can be characterized, modeled and simulated. Because the garment industry predates the composite industry, early developments in terms of characterization and modeling were in fact with cotton rather than carbon fibers in mind. And while graceful folds or *wrinkles* must be avoided when draping composites, an accurate prediction is quite essential.

Before going into detail with the properties of fabrics and modeling, it is appropriate to introduce the draping process in a composite context as well as the FlexDraper research project.

1.1 Composite Draping

Laminated fiber-reinforced polymers (FRP) consist of layers of aligned fibers embedded in a polymer matrix material, i.e. resin. An example of a laminated panel from an aircraft wing is sketched in Fig. 1.1. The fibers can for instance be made from glass, carbon or even polymer. Such composites exhibit high strength-to-weight and stiffness-to-weight ratios compared to metals and find widespread use in e.g. the automotive, aerospace, and sporting goods industries (Jones, 1999). The fiber plies exist as either "dry", in which case the resin is added subsequently, or as "prepreg", i.e. pre-impregnated with a partially cured resin. The latter gives a better control of the resin content in the composite and is often used in the aerospace industry. This study considers prepreg fabrics.

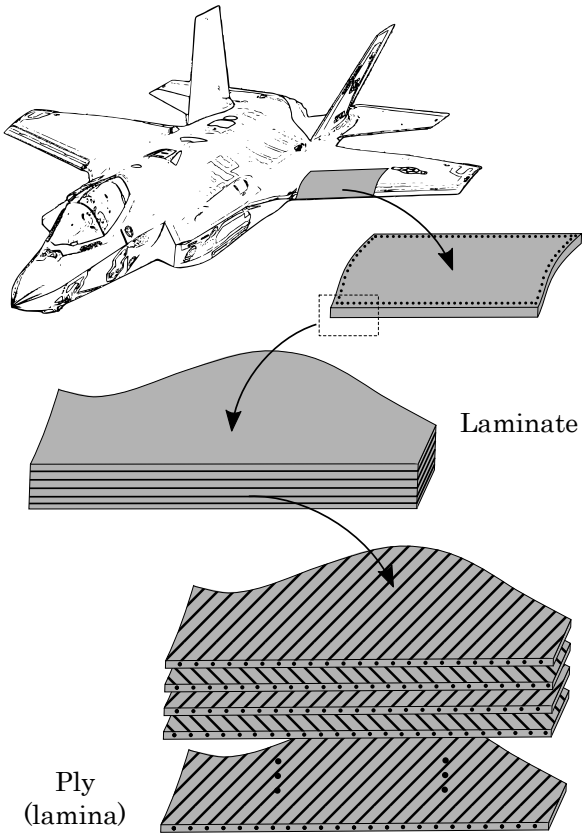

Fig. 1.1: Constituents of a laminated aircraft wing panel. The panel is attached by means of mechanical fasteners and adhesive bonding. Reworked from photo by Master Sgt. Donald R. Allen, U.S. Air Force (`www.dvidshub.net`).

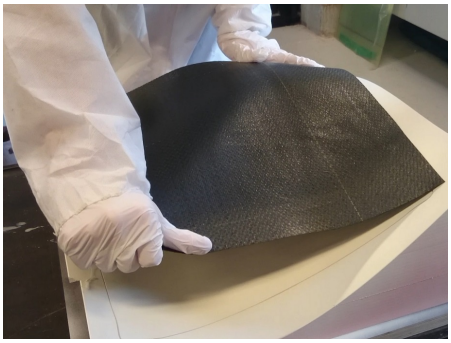

(a) Manual layup.

(b) Automated fiber placement. Photo by Fraunhofer IPT (`www.ipt.fraunhofer.de`).

Fig. 1.2: Manufacturing methods for layup of laminated prepreg composites.

Composites made from prepregs can be manufactured in a number of ways, but common to all methods is the fact that the fiber plies must be formed or *draped* to match the desired part geometry before the resin is cured or solidified. When the forming is achieved by placing the fibers on a mold surface, the process is denoted *layup*. Alternatively, the plies can be formed by compression between a male and female mold which is denoted *molding*. The choice of manufacturing method depends on the configuration of the fibers, the manufacturing volume and the complexity of the part (Jones, 1999).

The traditional and most versatile manufacturing method is *manual layup* as shown in Fig. 1.2(a), a process by which one or more operators manipulate the ply onto the mold by hand. While this method is flexible, the production costs are high due to the cost of manual labor, and complex parts in general require some operator skill (Elkington et al., 2015).

In the 1970s, an automatic layup system, automated tape laying (ATL), was developed. As the name suggests, it comprises a robot with the ability to deliver a strip of uni-directional prepreg tape onto the mold. A decade later, automated fiber placement (AFP) was introduced in which a number of narrow prepreg slices are brought together and aligned by the robot before being delivered to the mold as a single unit. An AFP system is depicted in Fig. 1.2(b). In general, by means of the multiple slices, AFP can handle more complex parts compared to ATL. Notice, though, that both ATL and AFP are restricted to uni-directional prepreg material (Lukaszewicz et al., 2012). That is, the fibers of each layer deposited on the mold by the robot are oriented in the same direction. Another fiber configuration, often found in the aerospace industry, is woven fabric with two fiber directions in each layer. In this study, the topic is composite manufacturing with woven prepreg plies by means of layup. Therefore, this process is elaborated in the following.

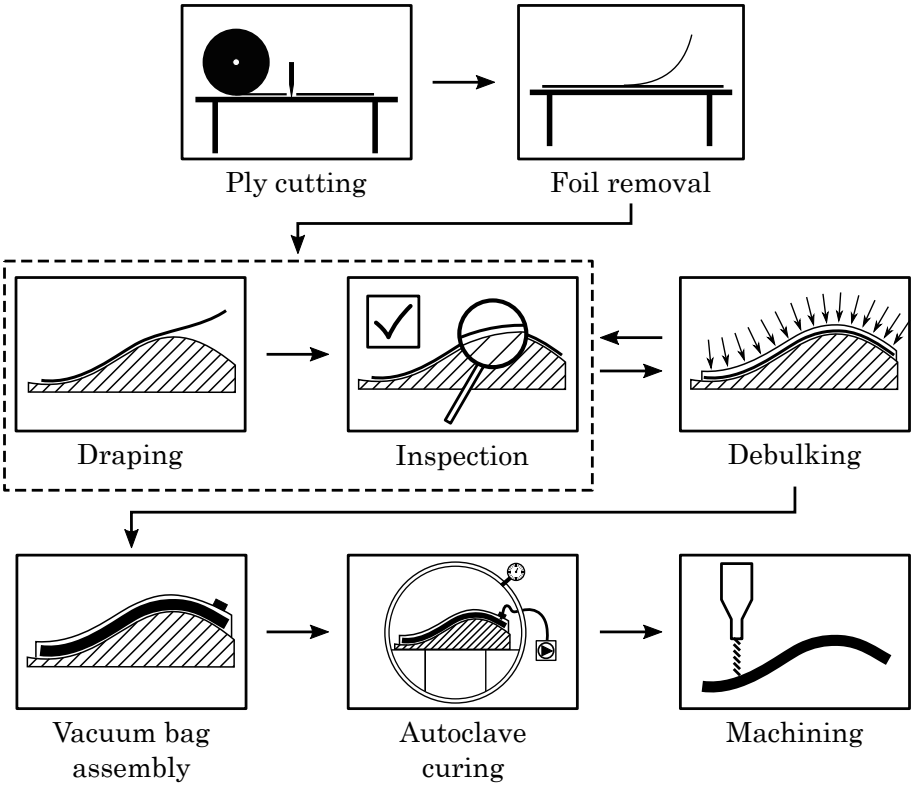

Fig. 1.3: The steps in manufacturing of composites made from woven prepreg.

1.1.1 Manufacturing of Composites with Woven Prepreg

The manufacturing of composites made from woven prepreg consists of several steps prior and subsequent to the draping as illustrated in Fig. 1.3. The prepreg material is stored in rolls with backing foil on each side. The first step is to unroll the ply on the cutting table. The cutting is carried out by means of a computer-controlled cutting head, and a conveyor belt advances the ply. Before draping, the backing foil must be removed. Then, each ply is draped on the mold followed by a manual quality inspection. After a certain number of plies - typically 10 - the layup must be *debulked* by means of vacuum. This process removes any entrapped air. When all plies are draped, some auxiliary materials are typically added. This could include a *breather*, which is a permeable fabric helping to ensure an even pressure distribution, and a *release film* which facilitate easier removal of the auxiliary materials. The layup and auxiliary materials are now enclosed in a vacuum bag, and the assembly is placed in an *autoclave*. Here, the composite is cured at high pressure and elevated temperature. After curing, the assembly is de-bagged

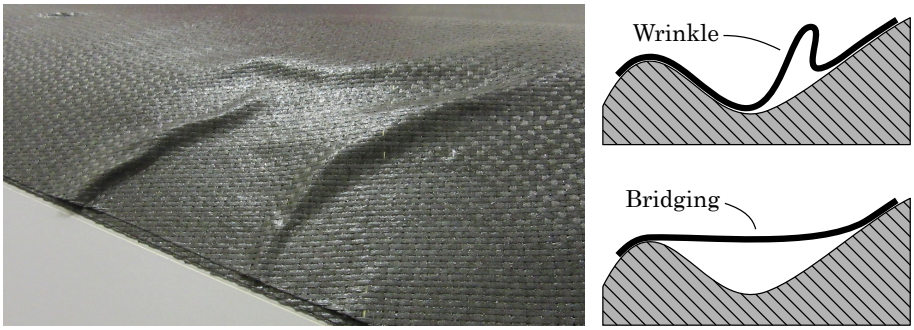

(a) Wrinkling and boundary misalignment. **(b)** 2D illustration of defects.

Fig. 1.4: Defects in woven carbon fiber prepreg layup.

and de-molded. The final step is machining in which the edges are trimmed and holes can be drilled. Naturally, the finished part is subjected to elaborate testing of dimensions and possible defects (Pansart, 2013).

This study focuses on the draping step in which the plies are formed to the mold surface. A requirement to the outcome of the draping process is that the draped plies must conform closely to the mold surface and thereby not include wrinkles. Further, the boundary of the ply must match a prescribed boundary. These requirements are checked in the "Inspection" step in Fig. 1.3. An example of an infeasible draping process is shown in Fig. 1.4(a). The concepts of a wrinkle and bridging is sketched in Fig. 1.4(b). In general, a wrinkle is an out-of-plane deformation, which in the draped configuration typically results in excess ply material compared to the mold surface area beneath it. The formation of wrinkles is a complicated mechanism, and it will be revisited in Chapter 2. Bridging is a shortage of ply material compared to the mold surface area beneath it. In the 2D sketch in Fig. 1.4(b), it is demonstrated that the length of the ply material, which is not in contact with the mold, is respectively longer (wrinkling) and shorter (bridging) than the arc length of the mold beneath it. Defects such as those in the figure would significantly deteriorate the mechanical properties of the final product. As a consequence, if the part was cured without correcting the layup defects, scrapping would be necessary.

1.2 The FlexDraper Research Project

The present PhD project is part of the research project *FlexDraper - An Intelligent Robot-Vision System for Draping Fiber Plies*. The purpose of the research project is to develop an automatic layup solution for entire plies of woven prepreg fabric. It is intended to operate on double curved mold surfaces of

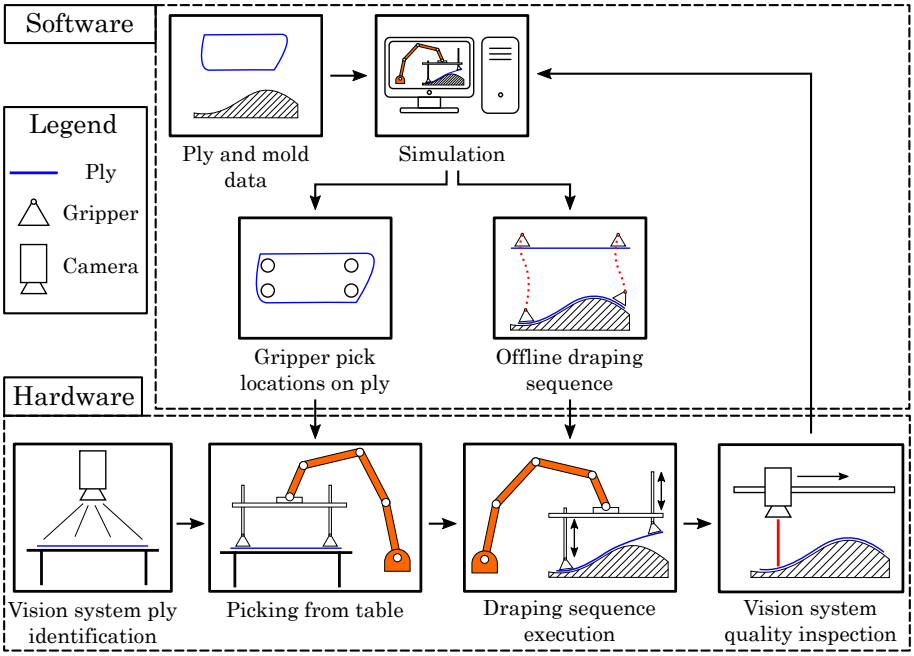

Fig. 1.5: Software and hardware components of the FlexDraper robot system.

low curvature which occur frequently in the aerospace industry. The project addresses the issue of the high cost associated with manual layup and additionally includes the prospect of increased and consistent part quality. A consortium of Danish universities as well as Danish and international industrial partners makes up the research project. The project partners are: Aalborg University, University of Southern Denmark, Technical University of Denmark, RoboTool A/S, Netherlands Aerospace Centre (NLR) and Terma Aerostructures A/S (Terma).

The project takes as its point of departure the current production of carbon fiber composites at Terma. The company is a subcontractor of US aircraft manufacturer Lockheed Martin and its product portfolio includes parts for the F-35 Lightning II fighter jet. The current layup process at Terma is performed manually and the idea is that the developed automated solution can be a direct substitute of the manual operation. Currently, Terma produces more than 100 composite parts for the F-35 program, and it is estimated that 75% can be automated. However, with the high number of different parts and also fairly low batch sizes, the system must be flexible and reconfigurable.

A schematic representation of the system setup is shown in Fig. 1.5. The robot is able to manipulate a ply by means of an end effector consisting of an array of actuated suction cups, i.e. grippers. First, the flat ply located

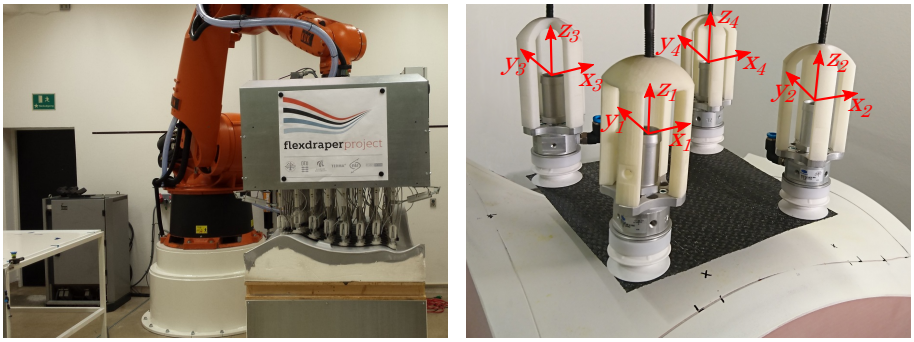

(a) The FlexDraper robot cell.

(b) The concept of the MiniDraper tool.

Fig. 1.6: Robot systems in the FlexDraper research project.

on a table is identified by means of a vision system. The ply is picked by the robot grippers at some computed pick points. The robot then moves the end effector into position over the mold and the grippers manipulate the ply onto the mold according to a computed draping sequence. It is crucial that the draping sequence places the ply inside a prescribed boundary and avoids wrinkling and other defects. The quality control is carried out by means of the vision system. The result can e.g. be fed back to the software for evaluation of the simulation.

Two robot end effector concepts were developed during the project. The FlexDraper, Fig. 1.6(a), and the MiniDraper, Fig. 1.6(b). In the FlexDraper robot cell, each gripper is actuated in the vertical direction while a system of links and joints enables the gripper grid to passively adapt to a double curved mold surface. In this way, not all degrees of freedom (DOF) are constrained. The grippers of the MiniDraper tool are actuated in all translational DOF. This setup allows for direct control of the gripper positions, but it also complicates the hardware.

An essential part of the FlexDraper research project is to generate feasible draping sequences for the robots. To this end, an understanding of the material behavior through experimental characterization is important. Next, a number of models of varying fidelity capable of aiding in the generation of the feasible draping sequences is of interest. This is exactly the motivation for the following sections.

1.3 Mechanics of Woven Fabrics

To understand the challenges associated with characterization and modeling of woven prepreg fabric, a discussion of the mechanical behavior is convenient. As introduced in Section 1.1, the prepreg fiber plies considered in this

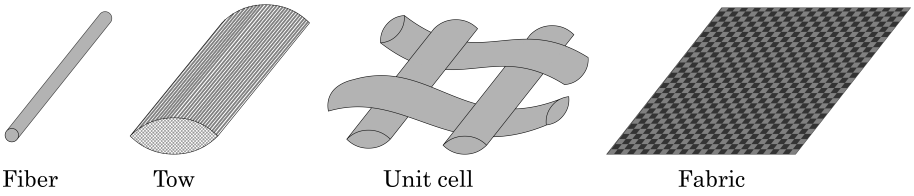

Fig. 1.7: Constituents of woven fabric at different length scales.

study consist of two different materials, i.e. the carbon fibers and the resin. This kind of material system spans several length scales, namely micro, meso and macro as sketched in Fig. 1.7. A single carbon fiber is approximately 6 μm in diameter, and by bundling several thousands of these fibers, a yarn or *tow* is formed. This is referred to as the microscale. Next, the tows are weaved in a specific pattern to form *unit cells* on the mesoscale. During weaving, the *weft* tows are held tensioned and straight, while the *warp* tows are pulled through and inserted over-and-under as determined by the weave pattern. The weave pattern shown in Fig. 1.7 is known as plain weave, and the side length of the unit cell is typically in the order of millimeters. Finally, the arrangement of all unit cells constitute the fabric on the macroscale (Boisse et al., 2008).

The macroscopic response of fabric is very different from that of continuous materials, such as metals or polymers. This difference occurs because of interactions at the micro and meso length scales. A single carbon fiber is very stiff with a Young's Modulus of typically 200-500 GPa (Minus and Kumar, 2005), and thus it can be considered quasi-inextensible. Because the fibers are thin and can move relative to one another inside the tow, the fabric bending stiffness, however, is relatively low.

At mesoscopic level, the tows are crimped due to the weaving. This means that if the unit cell is stretched in one fiber direction, the tows in that direction must straighten out, and at the same time, the tows in the other direction must be compacted. This behavior is known as *fiber straightening* and is sketched to the left in Fig. 1.8. As a result, the tensile response of the fabric is different from that of a single tow. In the unit cells, the tows can also move relative to each other. These movements include rotation at the cross-over points which is known as *shearing* as well as slipping of the cross-over points (Fig. 1.8 center and right). Ultimately, the deformation modes of the fabric facilitates the draping process without damaging the fibers. To this end, shearing is the dominant deformation mechanism when the initially flat fabric conforms to a double curved surface (Boisse et al., 2018).

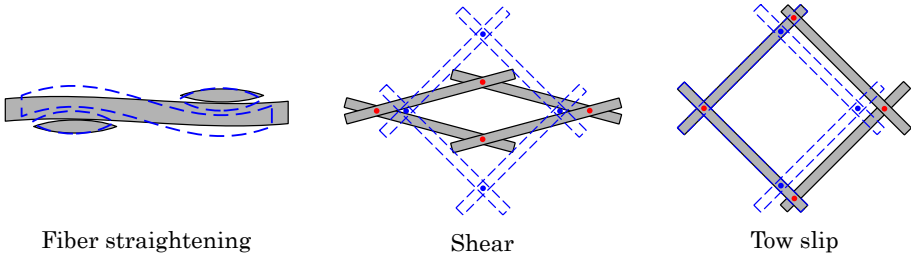

Fig. 1.8: Some deformation modes of woven fabric at the meso/unit-cell level. The blue dashed lines indicate the undeformed configuration.

The fabric is impregnated with a resin in which the hardener is present. This means that curing is invariably in progress, and that the prepreg has a limited lifetime. To extend this lifetime, prepregs are stored in a freezer to slow down the curing reaction (Pansart, 2013). Apart from complicating the handling of the prepreg material, the resin also causes the plies to behave *viscoelastically*, i.e. a combination of elastic and viscous behavior. The resin will somewhat stabilize the fabric, i.e. diminish some of the deformations at micro and meso levels compared to dry fabrics. Specifically, the slippage of the tows in the unit cells is reduced (Laroche and Vu-Khanh, 1994).

1.4 Fabric Test Methods

As discussed in the previous section, a woven fabric has numerous deformation modes at different length scales, and thus all of these modes can be characterized. The motivation for experimental testing is often to provide input to a simulation model, which thereby will dictate the appropriate experimental setup. Common to the tests applied to prepreg material is that the rate of deformation should be considered due to the viscoelasticity. Here, the focus is three major deformation modes on the macroscopic level, i.e. fiber direction tension, in-plane shear and out-of-plane bending. The section will conclude with an introduction to image processing as a tool to measure deformation in the test samples.

1.4.1 Fiber Direction Tension

The force vs. elongation characteristic of the fabric in the fiber direction can be measured by means of a uniaxial tensile test. A strip of the ply is mounted between the grips of a universal testing machine and extended. The fibers must be oriented along the loading direction. Recall from Section 1.3 that a tensile force applied in the fiber direction of a woven fabric will result in straightening of the crimped tows with an accompanied compaction of the

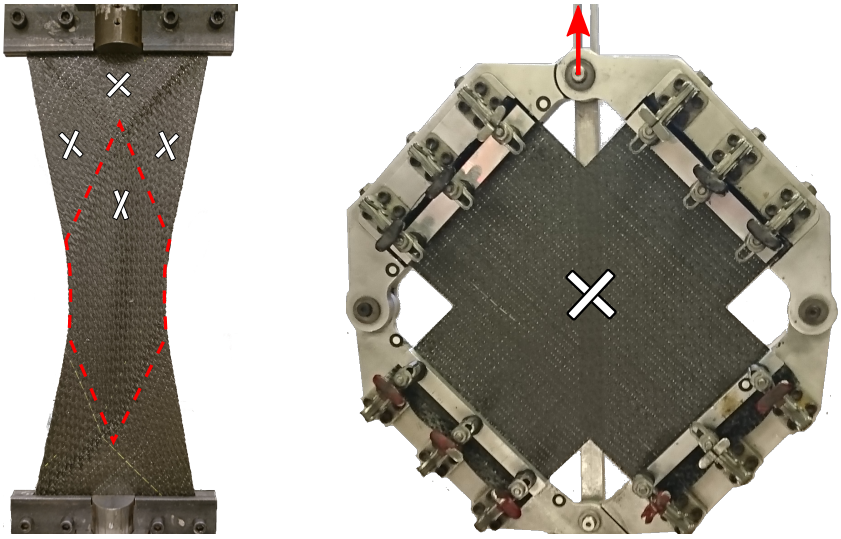

(a) Bias-extension test during deformation. The red dashed line enclose the pure shear zone.

(b) Picture-frame test in the undeformed configuration. The red arrow indicate the displacement of the upper joint during deformation.

Fig. 1.9: Test methods for shear characterization of fabric. White crosses indicate the tow directions of the sample.

tows in the other direction. As a consequence, the force response is nonlinear in the deformation. In addition, because of the tow interaction in the unit cells, the tensile state of one fiber direction in fact couples with the tensile state of the other direction. For this reason, a biaxial tensile test gives a more accurate characteristic of the fiber direction tension (Gereke et al., 2013). Biaxial testing is discussed in Section 2.1.1.

1.4.2 In-Plane Shearing

As previously noted, shearing is the dominant deformation mechanism during draping, and thus its characterization has received considerable attention. Two methods that are commonly applied for shear characterization are depicted in Fig. 1.9: the *bias-extension test* and the *picture-frame test* (Cao et al., 2008).

The bias-extension test involves a rectangular fabric sample cut in the bias direction, i.e. with the fibers oriented $\pm$ 45 degrees to the edges of the sample. The sample is clamped at the top and bottom using wide grips which are mounted in a universal testing machine. Extending the sample, a distinct, heterogeneous deformation field is created where a pure shear zone will exist in the center of the sample. A number of conditions must be satisfied for the test to be valid. Most importantly, because the tows shearing in the center of

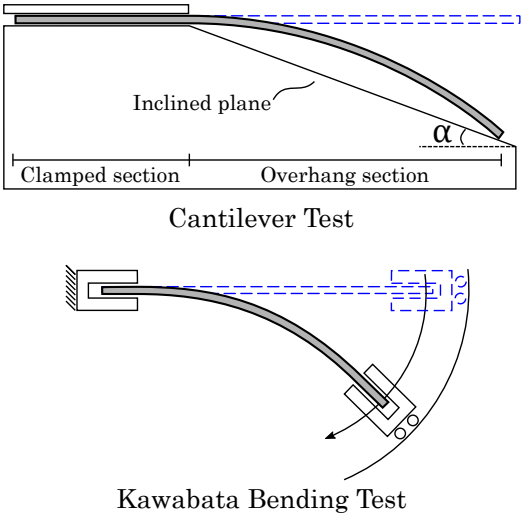

(a) Schematics of tests. The blue dashed lines indicate the undeformed configuration.

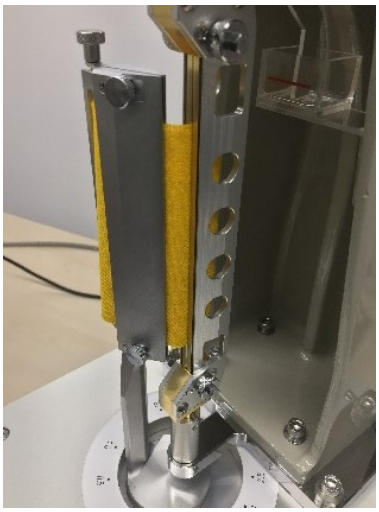

(b) Kawabata bending test machine. Photo by Kato Tech (`www.keskato.co.jp`).

Fig. 1.10: Standard bending tests for fabrics.

the sample are unclamped, slipping must be negligible (Boisse et al., 2017).

The picture-frame test relies on a square frame hinged at its corners. A sample is clamped in the frame with the fibers oriented parallel and perpendicular to the frame arms, respectively. By means of a universal testing machine, the lower joint is fixed in position, and the upper joint is displaced upwards. During this displacement, the frame transforms into a rhombus whereby a pure shear condition is imposed on the sample (Nguyen et al., 1999).

The picture-frame test requires a more complicated test setup compared to the bias-extension test, but it also avoids the nonuniform shear deformation field. Because of this nonuniformity, the data processing of the bias-extension comes with more uncertainty than the picture-frame test. Other issues, data processing approaches and modifications to the two tests are discussed in Sections 2.1.3 and 2.1.4.

1.4.3 Out-Of-Plane Bending

The out-of-plane bending properties are traditionally determined with one of two simple standardized tests (de Bilbao et al., 2010): The *cantilever test* first due to Peirce (1930) and the *Kawabata evaluation system (KES) bending test* (Kawabata, 1980) illustrated in Fig. 1.10(a). These tests were originally developed to measure the "feel" of textiles for the garment industry. Currently, they serve as the basis for more advanced bending tests recently developed

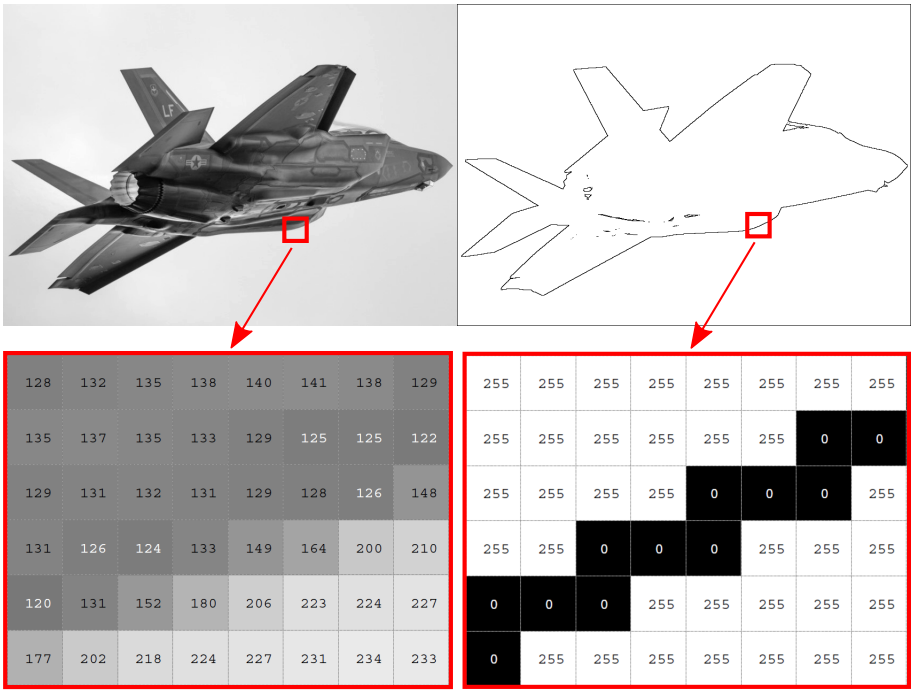

Fig. 1.11: Edge detection using a global threshold value of 191, i.e. 75% of the grayscale range. Photo by Senior Airman Alexander Cook, U.S. Air Force (`www.dvidshub.net`).

which are discussed in Section 2.1.5.

In the cantilever test, a horizontal strip of fabric is cantilevered under the influence of gravity. Based on the overhang length which the deflecting strip makes on a downwards inclined plane, a bending stiffness constant can be determined. Thus, the cantilever test assumes linear elastic behavior. The Kawabata test, Fig. 1.10(b), works by installing the two ends of a fabric strip in a stationary and moving clamp, respectively. Sliding is possible in the stationary clamp. The moving clamp describes a circular motion at a fixed rate whereby the bending moment vs. curvature can be measured. The test, however, requires a specific test machine which is costly (Lomov et al., 2003).

1.4.4 Measurements using Image Processing

By means of digital images, the test samples can be analyzed for deformation. In this study, grayscale images are used. A digital grayscale image consists of a 2D array of picture elements or *pixels* where each pixel has a specific color. An 8-bit image is able to represent 256 colors and thereby *256 shades of gray*. Therefore, each pixel in the image has a value in the range between 0 and 255 (Marques, 2011).

Digital image processing involves applications of varying complexity. A fairly simple example is edge detection of a planar object. If the contrast between the object and the background is sufficiently high, the object edge can for instance be detected by means of *global thresholding*. The method works by defining a tolerance or threshold of grayscale values. Next, a rounding is performed such that all values below the threshold are set to 0 (black) while all values above the threshold are set to 255 (white). Pixels on the edge of the object are then defined as having a value of 0 while being connected to at least one pixel with a value of 255. An example of edge detection using thresholding is provided in Fig. 1.11.

A more advanced example of image processing is that of digital image correlation (DIC) which has been successfully applied for deformation measurements in textile materials (Lomov et al., 2008). The method relies on a random *speckle pattern* on the surface of the sample. A reference image of the sample is taken before deformation, and subsequently images of the deformed sample are taken at intervals during the test. During processing of the acquired images, the reference image is divided into small *subsets*. Due to the random speckle pattern, each subset will have a unique combination of grayscale values. The idea is now to track each subset in the deformed images. This tracking is achieved by a *correlation criterion*, i.e. a criterion that compares greyscale values. The result is a displacement field for the sample. By differentiation, the strain field can be obtained (Lomov et al., 2008). The accuracy of the method can be assessed by taking two reference images and carrying out the correlation. Any calculated deformation is due to noise.

1.5 Modeling Approaches

The three length scales introduced in Section 1.3, i.e. micro, meso and macro, also represent three approaches to modeling of fabrics. Models on the microscale, however, are not suitable to predict the macroscopic ply behavior due to the high number of fibers and thereby the computational cost required (Boisse et al., 2008). Therefore, the remaining part of this section will consider modeling based on the meso- and macroscale which is denoted *discrete* and *continuous* modeling, respectively, as sketched in Fig. 1.12.

Discrete modeling refers to the fact that the discrete constituents or deformation modes of the fabric on mesoscale are considered separately. The idea is that the behavior of each discrete component in the model can be represented with simple properties. For instance, the most basic approach is to consider the tows as inextensible straight lines. These lines are connected at the crossover points in the weave where they are free to rotate, i.e. pin-jointed. In effect, the shear stiffness becomes zero. This model was proposed by Mack and Taylor (1956) and is known as the *pin-jointed net* model. Because

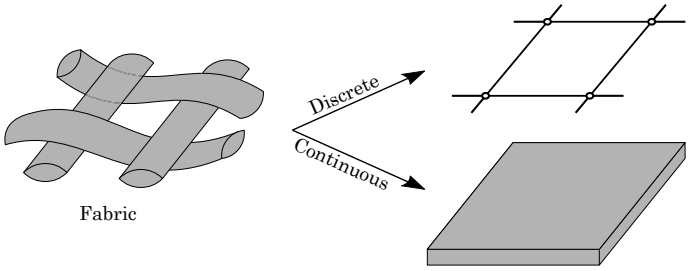

Fig. 1.12: Modeling abstractions for woven fabric.

it does not consider the material properties of the ply, it is also referred to as a kinematic model. Subsequently, discrete models that take the mechanical properties of the ply into account have been developed and recent advances are discussed in Section 2.2.2.

Continuous modeling of the ply relies on homogenized material properties. The idea is to capture only the macromechanical response, i.e. to "smear out" the response of the underlying length scales. The challenges with regard to the continuous modeling approach are to establish a link between experimental data and the homogenized formulation as well as update the instantaneous material properties in the model when the fabric deforms (recall the coupling effects discussed in Section 1.3). The benefit of the continuous approach is that the model is usually less time-consuming to evaluate compared to the discrete approach (Boisse et al., 2008). An example of the continuous approach is to consider the ply as a thin, flexible plate with linear elastic orthotropic properties as e.g. done by Kang and Yu (1995). More advanced continuous models are also discussed in Section 2.2.1.

Mechanical models, both discrete and continuous, are most often solved using the finite element (FE) method. In this study an *explicit dynamic* formulation is used, which is briefly introduced in Section 1.5.2. First, the application of kinematic models is elaborated.

1.5.1 Kinematic Mapping of Woven Fabric

Kinematic representations in the form of the pin-jointed net idealization are simple but have traditionally found widespread use to predict the draped configuration. In that sense, it works as a map from the ply in a flat configuration to the ply draped on the double curved mold (Akkerman et al., 2018). The ply is first divided into a pin-jointed grid of squares. A starting point or *seed point* and the two initial tow directions on the mold surface are chosen to constrain the first square. The remaining squares are now progressively laid onto the mold, one joint at the time as sketched in Fig. 1.13. In the simple case of an analytical mold surface equation specified by $F(x, y, z) = 0$, the

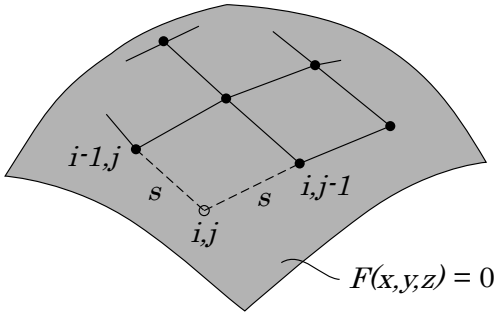

Fig. 1.13: Mapping of a ply onto a mold using the pin-jointed net model. Adapted from Wang et al. (1999).

problem of locating the joint i, j is defined by the following set of equations (Laroche and Vu-Khanh, 1994):

$$(x_{i,j} - x_{i-1,j})^2 + (y_{i,j} - y_{i-1,j})^2 + (z_{i,j} - z_{i-1,j})^2 = s^2 \tag{1.1}$$

$$(x_{i,j} - x_{i,j-1})^2 + (y_{i,j} - y_{i,j-1})^2 + (z_{i,j} - z_{i,j-1})^2 = s^2 \tag{1.2}$$

$$F(x_{i,j}, y_{i,j}, z_{i,j}) = 0 \tag{1.3}$$

The first two equations state that the distances between the neighboring joints must be equal to the grid spacing s, which is predefined. The third equation constrains the joint i, j to be on the mold surface.

Initiating the algorithm from the seed point and the two initial tow directions does not produce a unique solution. Remedies have been proposed in the scientific literature and are discussed in Section 2.3.1.

1.5.2 Explicit Dynamic Finite Element Analysis

The FE method is an approximate numerical method for solving field problems, i.e. the determination of the spatial distribution of some field variable. The method is versatile because it can handle arbitrary geometries and boundary conditions. It is often applied within the field of structural mechanics where the field variable is displacements. The basic idea is to divide the structure or part into a number of *elements* which are connected at *nodes*. Within each element, the field variable is approximated by interpolation of the nodal values by means of *shape functions*. Thus, the field problem can be converted into a set of algebraic equations in which the unknowns are the nodal values (Cook et al., 2002). For transient problems, the FE equilibrium

equation is given as:

$$[\mathbf{M}]\ddot{\mathbf{D}} + [\mathbf{C}]\dot{\mathbf{D}} + \mathbf{R}^{\mathbf{int}} = \mathbf{R}^{\mathbf{ext}} \tag{1.4}$$

Here $[\mathbf{M}]$ is the mass matrix, $[\mathbf{C}]$ is the damping matrix, and $\mathbf{D}$ is a vector of nodal displacements. An overdot implies the time derivative. The quantities $\mathbf{R}^{\mathbf{int}}$ and $\mathbf{R}^{\mathbf{ext}}$ are vectors of internal material forces and externally applied forces, respectively. For linear elastic materials, the internal forces, $\mathbf{R}^{\mathbf{int}}$, can be calculated based on a stiffness matrix $[\mathbf{K}]$:

$$\mathbf{R}^{\mathbf{int}} = [\mathbf{K}]\mathbf{D} \tag{1.5}$$

For nonlinear materials, some constitutive relation will provide the element stresses, $\boldsymbol{\sigma}^{\mathbf{e}}$, as function of the displacements, based on which the internal forces can be computed as follows:

$$\mathbf{R}^{\mathbf{int}} = \sum \mathbf{r}^{\mathbf{int}} \qquad , \ \mathbf{r}^{\mathbf{int}} = \int_V [\mathbf{B}]^{\mathrm{T}} \boldsymbol{\sigma}^{\mathbf{e}} \, \mathrm{d}V \tag{1.6}$$

In the equation, the summation indicates the assembly from element level to global level. $[\mathbf{B}]$ is the strain-displacement matrix, i.e. a matrix containing derivatives of the element shape functions with respect to the spatial coordinates. By means of *direct time integration*, the equilibrium equation is solved at discrete time intervals $n\Delta t$:

$$[\mathbf{M}]\ddot{\mathbf{D}}_n + [\mathbf{C}]\dot{\mathbf{D}}_n + \mathbf{R}_n^{\mathbf{int}} = \mathbf{R}_n^{\mathbf{ext}} \tag{1.7}$$

Either *implicit* or *explicit* time integration can be applied, with this study focusing on the latter. By means of Taylor series expansions for $\mathbf{D}_{n+1}$ and $\mathbf{D}_{n-1}$, 2nd order accurate expressions for the first and second derivatives of $\mathbf{D}_n$ are obtained:

$$\dot{\mathbf{D}}_n \approx \frac{1}{2\Delta t} \left(\mathbf{D}_{n+1} - \mathbf{D}_{n-1} \right) \tag{1.8}$$

$$\ddot{\mathbf{D}}_n \approx \frac{1}{2\Delta t^2} \left(\mathbf{D}_{n+1} - 2\mathbf{D}_n + \mathbf{D}_{n-1} \right) \tag{1.9}$$

Inserting the approximations from Equations (1.8) and (1.9) into Equation (1.7) (discrete FE equilibrium), the following is obtained after a minor reordering:

$$\left(\frac{1}{\Delta t^2}[\mathbf{M}] + \frac{1}{2\Delta t}[\mathbf{C}] \right) \mathbf{D}_{n+1} = \\ \mathbf{R}_n^{\mathbf{ext}} - \mathbf{R}_n^{\mathbf{int}} + \frac{1}{\Delta t^2}[\mathbf{M}](2\mathbf{D}_n - \mathbf{D}_{n-1}) + \frac{1}{2\Delta t}[\mathbf{C}]\mathbf{D}_{n-1} \tag{1.10}$$

This is the classical explicit difference equation at time step n in which the unknown quantity is the vector of nodal displacements at time step $n+1$, i.e. $\mathbf{D}_{n+1}$. If the mass and damping matrices, $[\mathbf{M}]$ and $[\mathbf{C}]$, are diagonal, the system of equations becomes decoupled making it very efficient to solve. A consistent mass matrix is not diagonal, but different "lumping" schemes exist that will yield an approximate diagonal matrix. Usually, the damping matrix is taken as the mass matrix multiplied by some constant α, i.e. $[\mathbf{C}] = \alpha[\mathbf{M}]$. This is known as mass proportional Rayleigh damping.

The explicit method is only *conditionally stable*, and it requires that $\Delta t \leq 2/\omega_{max}$, with ω_{max} being the highest eigenfrequency of the model. The time step can somewhat be related to wave propagation through the elements which is approximated by the *CFL condition*:

$$\Delta t \leq \frac{L}{c} \tag{1.11}$$

In the equation, L is the effective element length, and c is the speed of sound in the material which for linear elastic materials can be calculated using Young's Modulus, E, and the density, ρ, as $c = \sqrt{E/\rho}$ (Cook et al., 2002). Thus, it is evident that the stable time increment can be increased by increasing the element sizes or artificially increasing the density (mass scaling).

The explicit approach has both advantages and disadvantages compared to implicit time integration. It is very robust and handles nonlinearities well. It is also algorithmically simple, i.e. easy to apply when implementing new formulations. Finally, the memory requirements are lower. The issue is the conditional stability leading to small time steps which causes long solution times. The aforementioned robustness, however, means, that convergence issues are less frequent than with implicit time integration which can also add to the time spent with an analysis. A final issue is the accuracy, which can be affected by both round-off error due to many time steps and also force unbalances due to the fact that the method uses only historical information (Cook et al., 2002).

1.6 Robot Motion Planning

As mentioned in Section 1.2, an essential part of the FlexDraper research project is to generate feasible draping sequences. More specifically, to determine the *trajectories* of the grippers in the robot tool such that the fiber plies are draped in a manner which satisfies the quality requirements. A robot can for instance be programmed by *manual teaching*. This way of programming can be achieved by moving the robot along the desired trajectory, e.g. by means of a joystick. The manual approach is, however, time-consuming and inhibits the use of the robot system during programming which is why

offline programming, relying on a process model, is more suitable. Here, the trajectories can be calculated on a computer and subsequently transferred to the robot control software.

In this study, *optimization* is utilized to generate the gripper trajectories offline. For this reason, a brief introduction to the topic is provided in the following section.

1.6.1 Optimization Methods

Optimization is a mathematical discipline concerned with finding the optimal set of parameters, i.e. *design variables*, that minimize or maximize some *objective function* while satisfying a set of *constraints* (Arora, 2012). An example of application within the field of mechanical engineering could be a fighter plane. Here, the design engineers want the plane to be as light as possible while ensuring the structural integrity. The first step is to build a representative simulation model of the plane. Next, the objective function to be minimized is chosen as the mass of the plane subject to structural constraints, such as stresses evaluated at various critical locations in the structure. This minimization is achieved by altering the design variables which control the thicknesses of the composite panels in the simulation model.

An optimization problem with design variables stored in the vector $\mathbf{x}$ can be written in the following standard form:

$$\begin{aligned} \underset{\mathbf{x}}{\text{minimize}} \quad & f(\mathbf{x}) \\ \text{subject to} \quad & g_i(\mathbf{x}) \leq 0 \quad , \; i = 1, ..., p \\ & h_j(\mathbf{x}) = 0 \quad , \; j = 1, ..., m \end{aligned} \tag{1.12}$$

Here $f(\mathbf{x})$ is the objective function, and $g_i(\mathbf{x})$ and $h_j(\mathbf{x})$ are inequality and equality constraints, respectively. The criterion functions, i.e. $f(\mathbf{x})$, $g_i(\mathbf{x})$ and $h_j(\mathbf{x})$ can be anything from simple linear, analytical expressions to implicit results from a complex simulation model. The latter would be the case in the above example with the fighter plane.

The choice of algorithm to solve the optimization problem in Eq. (1.12) depends, among others, on the nature of the criterion functions and the number of constraints. One family of algorithms rely on *gradients* of the criterion functions. A gradient is a vector of partial derivatives, which thereby contains information about how a criterion function changes if a given design variable is changed. By way of example, for a function of one variable, the gradient is equal to the slope of the function. Naturally, to decrease the value of the objective function, the design variables must change according to the gradient of the objective function, $\nabla f(\mathbf{x})$.

For gradient-based algorithms, an important part of the implementation

is the *design sensitivity analysis*, i.e. the calculation of derivatives. Depending on the nature of the criterion functions it can be implemented more or less analytically or approximated numerically using *finite differences*. The latter is sometimes necessary with implicit criterion functions. For a function of one variable, the first order accurate finite difference approximation is given as:

$$\nabla f(x) \approx \frac{f(x+h) - f(x)}{h} \tag{1.13}$$

Here h is the perturbation which must be chosen. The finite difference approximation involves multiple function evaluations, and the results are dependent on the chosen value of h. Therefore, analytical or semi-analytical gradients are usually faster to evaluate and more robust (Arora, 2012).

1.7 Objectives of the PhD Project

The preceding sections of this chapter have discussed the challenges related to automated draping processes for woven carbon fiber prepreg plies and also outlined some relevant methods and tools. This discussion leads to the following overall research hypothesis:

"Numerical analysis can provide quantitative information about automated draping of prepreg plies in terms of predicting possible defects as well as feasible draping sequences".

The motivation for a numerical simulation model is that it can be evaluated and also reconfigured more easily than by operating the physical robot system. The research hypothesis suggests two purposes of the numerical simulation. The first purpose is to be able to predict possible defects such as wrinkles or bridging. The idea is that some generated draping sequence can be simulated before being executed on the robot system. This approach allows to detect possible flaws with the draping sequence at an early stage. Such a high fidelity model must include important physical effects of the ply material and the tool, and therefore it relies on material characterization.

The second purpose is to predict a drape pattern or draping sequence that will meet the quality requirements. Due to the high number of possible - but not necessarily feasible - gripper paths, the prediction of draping sequences will require a large amount of model evaluations with different gripper configurations, for instance by means of optimization. Therefore, a simulation model used for draping sequence prediction must be computationally inexpensive to evaluate.

Specific objectives in the form of research questions are formulated below:

1. Which experimental test methods are suitable to characterize the deformation mechanisms of prepreg ply?
2. How can the ply material behavior and the kinematics of the FlexDraper tool be captured in a high fidelity predictive simulation model?
3. What are the important ply deformation mechanisms to account for in an approximate model?
4. How can gradient-based optimization be utilized for determining robot draping sequences?

To ensure that the most relevant and up-to-date methods are applied for finding answers to the research questions, the state-of-the-art literature is reviewed in the next chapter.

2

State-of-the-Art Literature Review

> “ Nevertheless wrinkling is a global phenomenon and there is no simple relation between the shear angle and the wrinkles. Wrinkles are due to all strains and rigidities of the fabric (tension, in-plane shear and bending) and to boundary conditions. ”
>
> – Boisse et al. (2011)

Wrinkles and their prediction is a critical topic in the context of composite draping. Therefore, wrinkles also play an important role in the many scientific publications on the topic characterization and modeling of fabrics. This chapter presents a review of some relevant publications and is divided into sections covering experimental characterization, mechanical modeling and approximate modeling. The emphasis is placed on methods and approaches applicable to simulation of woven prepreg fabric draping. The chapter is concluded with a brief summary.

2.1 Experimental Characterization

Many studies based on the test methods introduced in Section 1.4 have been conducted and reported. The test methods in question can characterize the tensile, in-plane shear and out-of-plane bending response of fabrics.

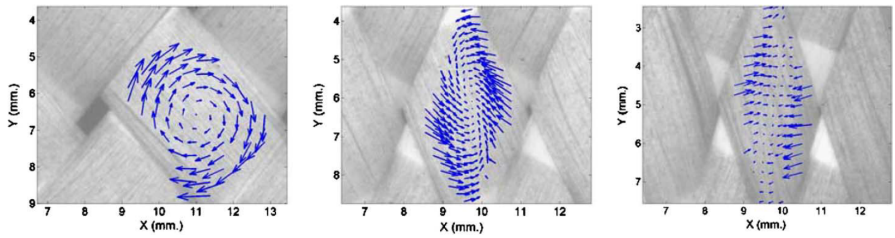

Fig. 2.1: Displacement field of tows during shearing obtained using DIC. Left: before locking angle. Middle: at onset of locking. Right: After locking angle. Reprinted from Zouari et al. (2006) with permission from Elsevier ©.

2.1.1 The Biaxial Tension Test

The uniaxial tensile test for evaluating the fiber direction tension is a fairly common test and will not be treated further. Instead, the focus is on the biaxial tensile test. Bassett et al. (1999) reviewed and discussed various approaches for the test setup. A major concern is how to allow the fabric to undergo tensile strain in a direction along the clamps. Two remedies have been applied. The first remedy is to design the clamps such that the fabric can move freely parallel to the gripped edge. The second remedy is to use a cruciform sample, and Bassett et al. (1999) additionally suggested to remove the transverse tows. This sample configuration was used by Boisse et al. (2001) for their biaxial tensile tests on dry fabrics. A specially designed test rig was applied in which the ratio between weft and warp strains can be adjusted. Based on the tests, the authors generated a surface of fabric load vs. the strain in the weft and warp directions. Using Digital Image Correlation (DIC), Lomov et al. (2008) showed that the removing of the transverse tows in the arms of their tested samples did not affect the uniformity of the strain field, and that the shear induced in the sample was negligible.

2.1.2 In-Plane Shear Characterization

As previously noted, in-plane fabric shear is the dominant deformation mechanism during draping. Shearing of the fabric at a macroscopic level corresponds to rigid tow rotations at the cross-over points, i.e. at mesoscopic level. The tows can rotate until they come in contact with the neighboring tows which inhibits further tow rotation. This phenomenon is generally referred to as jamming and the corresponding degree of shear as the *locking angle* (Lindberg et al., 1961; Grosberg and Park, 1966). Using DIC on a unit cell of a dry woven fabric, Zouari et al. (2006) verified, as shown in Fig. 2.1, that shearing corresponds to rigid body rotation of the tows followed by a lateral compression when the locking angle is reached.

Many researchers have applied the bias-extension test and the picture-

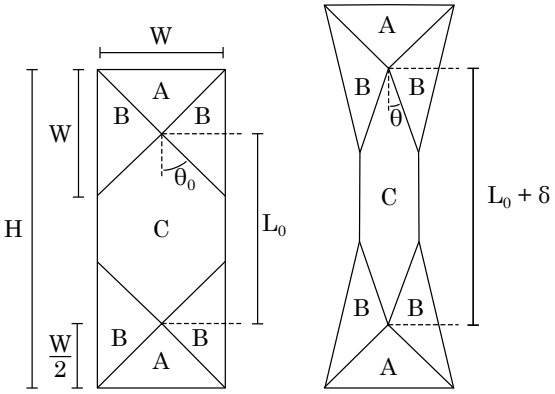

Fig. 2.2: Bias-extension sample before and after deformation. Adapted from Lebrun et al. (2003).

frame test to characterize this shear behavior. It can be mentioned that a third common test exists as part of the Kawabata evaluation system (KES) (Kawabata, 1980) which originates from the garment industry. In this test, a rectangular sample is clamped in the top and bottom. The lower clamp is fixed while the upper clamp is displaced horizontally, thus imposing a condition of simple shear. As with the Kawabata bending test, it only considers fairly small deformations, and in addition the shear state in the sample is not uniform (Hu and Zhang, 1997). The test was applied by Lomov et al. (2003) whose focus was the low-load regime.

2.1.3 The Bias-Extension Test

The bias-extension test has been developed since the 1960's (Boisse et al., 2017). An important requirement is that the height H of the rectangular sample is at least twice the width W (Wang et al., 1998). If this aspect ratio is fulfilled, three distinct deformation zones develop in the test sample during deformation (Lebrun et al., 2003) as sketched in Fig. 2.2.

In zone A all tow ends are fixed by the clamping and thus no shear deformation takes place. In zone C both families of tows have free ends and theoretically, a pure shear zone will exist with the shear angle being denoted γ. In zone B one family of tow ends is fixed, and the other family is free whereby shearing with half the value of γ occurs.

To process the force vs. elongation output from the universal testing machine, two relations are necessary: a relation between the elongation and the shear angle, and a relation between the crosshead force and the shear force on the gage area. Assuming that the tows are inextensible, that no slipping occurs and that the in-plane tow bending stiffness is zero, the shear angle

relation can be derived from Fig. 2.2 using trigonometry (Lebrun et al., 2003):

$$\cos\theta = \frac{L_0 + \delta}{2L_0 \cos\theta_0} = \frac{L_0 + \delta}{\sqrt{2}L_0} \tag{2.1}$$

$$\gamma = 90^\circ - 2\theta \tag{2.2}$$

Here, δ is the elongation of zone C which corresponds to the elongation of the sample because zone A remains undeformed.

Next, for the shear force relation, the shear deformation in zone B must be taken into account as well, because it also contributes to the measured crosshead force. By considering the power dissipated in shearing zones C and B and equating that to the power generated by the moving crosshead, a rate-independent expression for the shear force per unit width, $F_{\text{sh,norm}}$ was derived (Launay et al., 2008; Cao et al., 2008):

$$F_{\text{sh,norm}}(\gamma) = \frac{1}{(2H - 3W)\cos\gamma}\left[\left(\frac{H}{W} - 1\right) F\left(\cos\frac{\gamma}{2} - \sin\frac{\gamma}{2}\right) - W F_{\text{sh}}\left(\frac{\gamma}{2}\right)\cos\frac{\gamma}{2}\right] \tag{2.3}$$

In the formula F is the crosshead force. The expression gives $F_{\text{sh}}(\gamma)$ incrementally since the shear force at a shear angle γ depends on the shear force evaluated at $\gamma/2$. A viscous alternative was developed by Harrison et al. (2004) assuming Newtonian fluid behavior:

$$F_{\text{sh,norm}} = \frac{\frac{H}{W} - 1}{2\frac{H}{W} - 3 + 2X}\frac{F}{\frac{\sqrt{2}}{2}W} \quad , \; X = \frac{1}{4}\left[\frac{\cos^2\gamma\left(1 + 3\sin^2\frac{\gamma}{2}\right)}{\cos^2\frac{\gamma}{2}\left(1 + 3\sin^2\gamma\right)}\right] \tag{2.4}$$

A Newtonian fluid has a constant viscosity independent of strain rate. Therefore, this assumption also introduces errors because material systems with a viscous matrix material in general exhibit a rate-dependency (Harrison et al., 2004; Machado et al., 2016b).

The above assumptions regarding the shear angle calculation in (2.1) and (2.2) have been tested by a number of authors. Slipping of tows in dry fabrics was for instance investigated by Wang et al. (1998). They concluded that slipping in zone C is negligible before the locking angle is reached. However, this observation did not apply to the whole sample. Slipping was observed at the boundaries between the deformation zones of the samples - predominantly in carbon fiber fabrics - which led the authors to the conclusion that the in-plane bending stiffness could influence the slipping mechanism. Usually, tow slipping does not become significant until a certain shear angle. For the thermosetting prepreg tested at room temperature by Harrison et al. (2004), the

limiting shear angle was approximately 40°.

To take the possible tow slip into account, the shear angles of the samples can also be determined optically. One simple approach is manual measurements on images taken during the test (Harrison et al., 2004), or by using DIC (Zouari et al., 2003; Lomov et al., 2008). Recently, Pasco et al. (2019) proposed a shear angle measurement algorithm based on tracking of dots painted on the sample. It proved useful up to high shear angles for which DIC can fail due to the compaction of tows and thereby the speckle pattern. Also, advanced commercial laser measurement systems exist, as e.g. employed in the study by Krieger et al. (2015).

Wrinkling in the gage area is common in the bias-extension test, but as demonstrated by Alsayednoor et al. (2017) it can lead to overestimations of up to 20% of the actual shear angle when using 2D optical measurement techniques. The same authors also investigated the effect of pre-shearing, i.e. unintended shearing of the sample prior to testing. This effect can also lead to severe inaccuracies during the calculation of the shear force vs. shear angle. To circumvent wrinkling, Harrison et al. (2018) investigated the use of so-called anti-wrinkle plates mounted in the front and in the back of dry fabric samples with a gap of 2 mm between them. The authors reported that the plates significantly improved the repeatability and accuracy of kinematic measurements with only a slight increase in the crosshead force due to friction. While the technique in its current form is unsuitable for prepregs due to the adhesion, the authors did discuss possible extensions, such as lubrication of the plates.

Modifications of the bias-extension sample geometry has also been studied. In an effort to limit the slipping of tows, Wang et al. (1998) suggested to use samples with the width extending beyond the clamps. Thereby the free tows in the sample will have a higher frictional restraint and greater resistance to slippage. See also the study by Potluri et al. (2006) in which the authors concluded that the use of the wide samples yielded better results compared to the conventional samples. A biaxial bias-extension test has also been suggested to study the influence of tensions during shear (Sharma et al., 2003). Harrison et al. (2012) conducted a number of such tests on plain woven glass fabric and concluded that the increase in tow tensions delays the onset of wrinkling as well as leads to a significant increase in shear load.

2.1.4 The Picture-Frame Test

Apart from the bias-extension test, the application of the picture-frame test shown in Fig. 2.3 has also received attention in the literature. Analytical formulas have been developed to relate the crosshead displacement, δ, and crosshead force, F, to the frame angle, θ, and the shear force, F_{sh}, on the

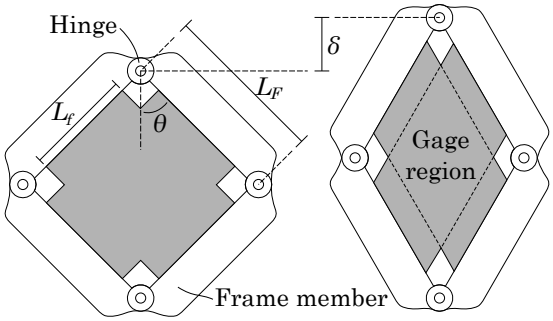

Fig. 2.3: The picture-frame test before and after deformation.

sample (Cao et al., 2008):

$$\cos\theta = \frac{\sqrt{2}L_F + \delta}{2L_F} \tag{2.5}$$

$$F_{\text{sh}} = \frac{F}{2\cos\theta} \tag{2.6}$$

Here, the frame angle θ is related to the theoretical shear angle of the sample, γ, according to Equation (2.2). The mass of the frame contributes to the measured crosshead force, and for this reason the force measurement of an empty frame should be subtracted before application of Equation (2.6). The shear angles can - like in the bias-extension test - be measured optically. Lomov et al. (2008) conducted such measurements on a range of fabrics and concluded that the shear strain field was reasonably homogeneous, and that the average of shear angles was within a couple of degrees of the theoretical shear angle from the frame kinematics.

The sample is square but typically the corners are cut (see Fig. 2.3) to allow free deformation of the frame without inducing wrinkles in the fabric (Liu et al., 2005). In effect, the sample shape becomes cruciform. The gage region is normally considered the central square of the cruciform. These considerations regarding the sample geometry come into play when discussing normalization of the shear force. That is, to obtain the normalized shear force, $F_{\text{sh,norm}}$, which is independent of the dimensions of the sample and the frame. Harrison et al. (2004) proposed to divide the shear force by the side length of the frame. This expression was based on energy considerations but also that the fabric was of the same side length as the frame. Another normalization, also based on energy, was proposed by Peng et al. (2004) taking the possible

difference of frame and sample into account:

$$F_{\text{sh,norm}} = F_{\text{sh}} \frac{L_F}{L_f^2} \tag{2.7}$$

Here L_F and L_f are the length of the frame and the fabric, respectively as indicated in Fig. 2.3. A final remark is that the normalization scheme in Equation (2.7) was developed assuming no contributions from the arms of the cruciform. For dry fabrics, some researchers target this condition by removing the cross tows (Cao et al., 2008).

In the picture-frame test, the boundary conditions of the sample are important. Unlike the bias-extension test, the ends of the shearing tows are clamped which can affect the tension in the tows as well as their rotations. Basically, if the tension is too low, the sample will not shear to the same extent as the frame, but a high tension will increase the shear load. The latter is especially true in the case of misalignments of the fiber directions with respect to the frame (Harrison et al., 2004). These issues have led researchers to experiment with alternative clamping designs. Launay et al. (2008) developed a clamping device for a picture-frame test rig which allowed them to adjust and measure tensions along the fiber directions. The authors confirmed that for the tested dry plain-weave samples, the shear load increased with increasing initial tow tension which is due to the increase in friction. Surprisingly, the authors also showed that for a zero initial tension, nonzero tensions could still be measured during the test. See also the study by Nosrat-Nezami et al. (2014) who, in addition to the controlled tensions, used needles to pin the fabric tows to the frame. Milani et al. (2010) proposed a modified picture-frame test in which only the corners of a square sample was clamped to the frame. Using dry fabric, they showed that the modification made the test less sensitive to misalignments.

2.1.5 Out-of-Plane Bending Test Setups

Early works on draping of fabrics focused on shear locking as the main cause of wrinkle formation and disregarded bending (Boisse et al., 2011). As the quote in the beginning of this chapter outlines, the bending behavior of fabrics is also important and particularly for the shape of the wrinkles. To this end, a number of testing procedures have been discussed in the literature. The basis is the simple bending tests introduced in Section 1.4.3.

de Bilbao et al. (2010) suggested an extension of the classical cantilever test. To account for nonlinear bending behavior of fabrics, the test is repeated with a number of different fabric overhang lengths. The outcome is successive quasi-static measurements obtained for different load cases. An optical measurement system was used to capture the shape of the deflecting spec-

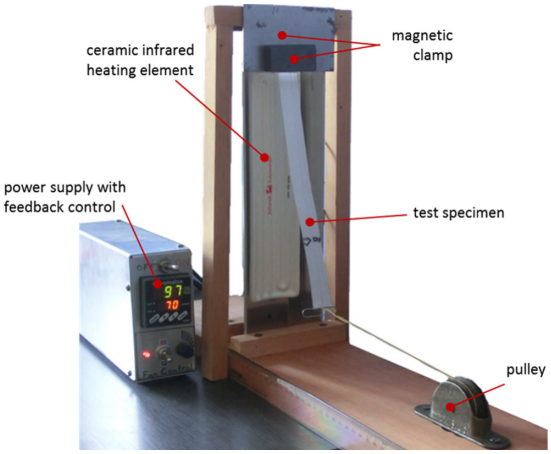

Fig. 2.4: Vertical cantilever test setup with heating element used by Dangora et al. (2018). Reprinted with permission from Springer Nature ©.

imen. Based on the test, a plot of the moment vs. curvature for the fabric can be generated. Liang et al. (2014) presented a cantilever test in which the fabric strip can deflect freely, i.e. without the inclined plane. They placed the test setup in an environmental chamber which allowed them to test the temperature dependency of their prepreg samples. A possible issue with the samples deflecting under gravity is twisting which can be alleviated by using a vertical test (Soteropoulos et al., 2011; Dangora et al., 2015). The sample is loaded at the end by means of the attachment of a string tied to a mass. In a later study, shown in Fig. 2.4, the test was expanded to characterize a thermoplastic cross-ply at elevated temperatures by positioning an infrared heater behind the test sample (Dangora et al., 2018). The actuation system of the test setup was refined by Alshahrani and Hojjati (2017) who included an actuator and a load cell for improved control of the force and deflection. This addition, for instance allows for measuring stress relaxation.

An advanced test apparatus resembling the Kawabata bending test has also been developed (Sachs and Akkerman, 2017). The setup relies on a rotational rheometer by means of which the moment vs. rotation angle is recorded. See also the study by Poppe et al. (2019) which includes a comparison of the rheometer test and the cantilever test. To this end, discrepancies are observed and discussed. Also, a buckling test was suggested by Wang et al. (2010). The advantage of the test is that it can easily be carried out with a standard universal testing machine.

2.2 Mechanical Modeling

Advanced predictive simulation models of the draping process are based on the physics of the ply material and often accomplished using explicit finite element (FE) analysis. Some models, particularly early works, have disregarded the bending stiffness of the fabric, which can lead to unphysical buckling as well as poor wrinkle prediction (Harrison, 2016). As discussed in Section 1.5, the modeling can be accomplished as either *continuous* or *discrete*. The former concerns a homogenization on macroscopic level whereas the latter is based on the discrete constituents of the fabric.

2.2.1 Continuous Modeling

A continuous ply model can be implemented in standard finite elements such as membranes or shells. The difficulty lies in the homogenization theory, i.e. a constitutive relation that can provide the element stresses based on the deformation (cf. Section 1.5.2). A major concern is to take the effect of the changing fiber directions into account (Boisse et al., 2008).

Early continuous models assumed linear elastic material behavior, such as the work by Dong et al. (2001) which introduced a simple updating scheme to account for the changing fiber directions. In the model, a rotated orthotropic stiffness tensor was assigned to each family of tows. A homogenized stiffness tensor was then obtained by simply adding the two individual stiffness tensors. The rotation angles were updated as shear developed.

Recent developments capture the inherent material nonlinearities of the fabric. To that end, the constitutive formulations are typically based on either *hypoelasticity* or *hyperelasticity*, i.e. general nonlinear solid mechanics theories.

A hypoelastic or rate-constitutive law takes the following form:

$$\boldsymbol{\sigma}^{\nabla} = \mathbf{C} : \mathbf{D} \tag{2.8}$$

Here, $\boldsymbol{\sigma}^{\nabla}$ and $\mathbf{D}$ are the stress and strain rate tensors, respectively. $\mathbf{C}$ is the constitutive tangent tensor, which can depend on the state of stress. The stress rate, $\boldsymbol{\sigma}^{\nabla}$, must be independent of rigid body rotation. It can be shown that the time derivative of Cauchy stress does not fulfill this criteria for which reason so-called objective stress rates are used (Belytschko et al., 2000).

To account for the changing fiber directions, non-orthogonal models were developed, see e.g. Yu et al. (2002) and Peng and Cao (2005). Here, coordinate axes follow the changing weft and warp fiber directions. In the latter reference, a fiber tracking scheme was presented based on the initial fiber directions, the rigid body rotation and the deformation gradient tensor. Bending stiffness was considered by Yu et al. (2005) who used an asymmetric modulus to make the compressive stiffness weaker than the tensile counterpart. A

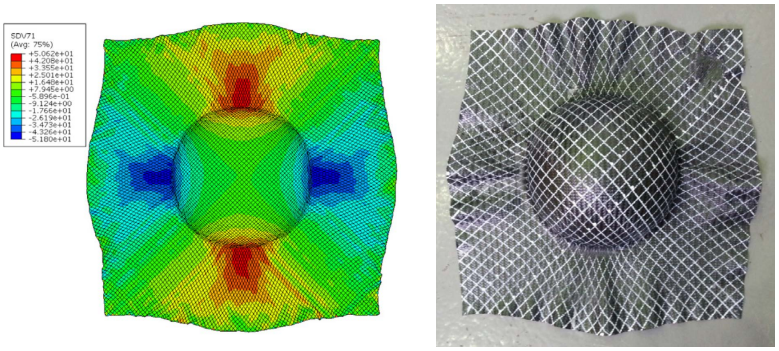

Fig. 2.5: Hemispherical punch forming of prepreg fabric. Left: numerical simulation using hypoelastic model. Right: experimental result. Reprinted from Khan et al. (2015) with permission from Elsevier ©.

non-orthogonal model was further developed by Lee et al. (2008) to include the effect of tow tensions on the shear behavior.

Komeili and Milani (2016) implemented shear-tension coupling in the built-in *Abaqus fabric* material model using a user subroutine VFABRIC. They studied press forming with a punch and blank holder on three different geometries and concluded that the overall shear angle distribution was not notably affected by the coupling mechanism. The stress distribution was, however, affected which could have an effect on the residual stresses after curing.

The objective stress rates typically employed in FE formulations are based on the rigid body material rotations. These formulations have proven successful for e.g. sheet metal forming simulations in which the anisotropy does not change significantly during processing (Boisse et al., 2008). It can, however, be shown that the conventional objective stress rates can cause spurious stresses when considering fabric materials (Badel et al., 2008). It was therefore proposed by the authors to use the fiber rotation as the basis for the objective stress rate. The authors presented simple studies of UD composites to highlight the issues. The formulation with a stress rate based on fiber rotations was later extended to two families of fibers by Khan et al. (2010). For the purpose of simulating prepregs, the model was further developed by superimposing to families of membrane elements (Khan et al., 2015). One family has the fibrous properties whereas the other family can be either elastic or viscoelastic representing the resin behavior. According to the authors, the advantage of the proposed model is that the resin content can be accurately controlled. A comparison between simulation and experimental forming from the paper is shown in Fig. 2.5.

Recently, Machado et al. (2016a) developed a non-orthogonal model for thermo-plastic composite forming simulations in which the shear stress is dependent on the rate of deformation. The shear data were input in the model

as a polynomial surface fit obtained from a number of bias-extension tests.

A challenge with a hypoelastic formulation is that it does not always allow complete recovery when the loading follows a closed loop path (Aimene et al., 2010).

The hyperelastic models are defined from a energy potential ψ. The current state of stress is the partial derivative of the potential with respect to the strain:

$$\mathbf{S} = 2\frac{\partial \psi}{\partial \mathbf{C}} \tag{2.9}$$

In the equation, $\mathbf{S}$ is the 2nd Piola-Kirchhoff stress, and $\mathbf{C}$ is the right Cauchy-Green deformation tensor. The Cauchy stress can be computed using the deformation gradient, $\mathbf{F}$, and its Jacobian:

$$\sigma = J^{-1}\mathbf{F}\mathbf{S}\mathbf{F}^{\mathrm{T}} \tag{2.10}$$

Because of the energy potential, hyperelastic models are per definition path independent. Further, the frame-invariance can be taken into account in the energy potential (Belytschko et al., 2000).

Aimene et al. (2010) developed a hyperelastic model for dry fabrics. The energy potential is composed of the energies from weft and warp fiber extensions plus shear. The energies were formulated as function of invariants of the right Cauchy-Green deformation tensor: fiber stretch in the warp direction, fiber stretch in the weft direction and angle variation between the fibers. Experimental data expressed as polynomials as a function of the invariants was used to calibrate the model. The validity of the model was then confirmed by checking its ability to fully recover after a closed-loop loading. Finally, a simulation of a hemispherical forming process was compared to experimental data with good agreement. See also the hyperelastic model by Peng et al. (2013).

A hyperelastic model for simulation of prepreg thermoforming was developed by Gong et al. (2016). Experimental data obtained at the forming temperature was used for model calibration. An additional term was added to the energy potential to account for the matrix material.

In the visco-hyperelastic model by Guzman-Maldonado et al. (2015), the energy potential has the original three in-plane terms related to dry fabrics. It was extended with a term accounting for out-of-plane bending. Further, a viscoelastic model was added to the shear deformation.

A special purpose 3-node membrane finite element using the so-called *semi-discrete* modeling approach was presented by Hamila and Boisse (2007). It was later extended to a shell element formulation to account for out-of-plane

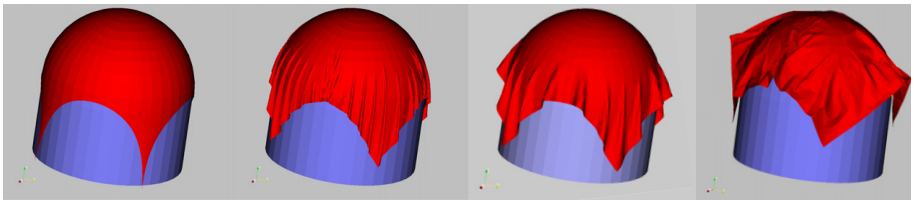

Fig. 2.6: Influence of shear and bending rigidity on the draping process. From left to right: tensile rigidity only; tensile and shear rigidities; tensile, shear and bending rigidities; isotropic membrane model. Reprinted from Boisse et al. (2011) with permission from Elsevier ©.

bending (Hamila et al., 2009). The element formulation is derived using the principle of virtual work, and the energies stem from fiber extensions, shear and out-of-plane bending of a discrete number of woven unit cells. Calibration with experimental tests is also simple due to the separation of the deformation modes. The element is numerically efficient because only the physical quantities related to fabrics are computed, and because rotational degrees of freedom are omitted. Element curvatures for bending moment calculations are instead obtained from neighboring elements. The element was used by Boisse et al. (2011) to analyze the influence of shear and bending rigidities on the draping of a fabric onto a hemispherical mold. A result from the paper is reproduced in Fig. 2.6. It was concluded that large shear angles can induce wrinkles, but that wrinkling in general is a global phenomenon for which the bending stiffness is important for the wrinkle shapes.

Allaoui et al. (2011) conducted a benchmark study on press forming with a tetrahedral shape to provoke wrinkling. The process was simulated with the semi-discrete approach and the built-in Abaqus fabric material model. The latter performed reasonably compared to the semi-discrete approach concerning shear angle and wrinkle prediction. Another modeling approach using internal unit cells was proposed by Kaiser et al. (2019). Here, the element stresses of the finite elements are computed based on a unit cell of crossing beam elements.

Most of the models in the literature consider the fabric as elastic, and as noted by Boisse et al. (2008), the forming process is typically more or less monotonous. Yet, dissipation does occur which was addressed by Denis et al. (2018). The dissipation was considered to arise from friction between crossing tows during shearing. Model calibration data was obtained by means of cyclic picture-frame tests.

Another enhancement of the continuous models concerns the so-called second-gradient theory (Ferretti et al., 2014). For instance, in a hyperelastic formulation, the energy potential is a function of the right Cauchy-Green deformation tensor, $\mathbf{C}$. By including contributions from its gradient, $\nabla\mathbf{C}$, the

local bending stiffness of the fibers can be taken into account. This ensures a more realistic course of the tows and for instance allows for modeling the transitions between the different shear zones in the bias-extension test (Boisse et al., 2017).

A very recent achievement was made by Iwata et al. (2019) who combined macroscopic and mesoscopic modeling in an "macro-meso zoom" approach. The draping process is simulated using a traditional continuous approach, and e.g. in areas of high curvature where defects are prone to occur, a local mesoscopic model is evaluated using boundary conditions from the continuous model. The mesoscopic model considers each tow individually. This enabled the authors to model tow slippage and buckling with a high level of detail which would otherwise not be feasible with a full-scale draping simulation.

2.2.2 Discrete Modeling

A number of discrete models for predicting the macroscopic ply behavior have been proposed in the literature. The idea is to use a combination of structural finite elements, such as beams or trusses, to represent the tows in combination with for instance springs or membrane elements to account for the tow interaction and possible resin. The tow elements are initially organized in an orthogonal grid. The model proposed by Cherouat and Billoët (2001) for prepreg fabric consists of nonlinear truss elements and isotropic, viscoelastic membrane elements. The model was validated using in-plane tensile tests at various fiber orientations with respect to the loading direction and by draping experiments. In the model by Sidhu et al. (2001) for dry fabric, a combination of truss and shell elements are used. The two families of tows are not directly connected to each other, but instead loads are transferred via the shell elements. This allows for modeling tow interactions, such as sliding and locking. The model predictions were compared to stamping tests, and good agreement was found.

Discrete models using only truss elements have also been developed. Here, diagonal trusses in the grid represent the tow interaction. This approach was for instance taken for modeling dry fabrics by Sharma and Sutcliffe (2004) who used a bias-extension test to calibrate the behavior of the diagonal truss elements. The model unit cell is shown in Fig. 2.7(a). In the work by Skordos et al. (2007), a prepreg truss model was developed. A bilinear material model was used for the tow trusses, and a rate-dependent, nonlinear elastic-viscoplastic material model was used for the shear trusses. Wrinkle formation was taken into account by deactivating tow elements subjected to compression.

The discrete models in the previously mentioned references have disregarded the out-of-plane bending stiffness. This effect can be taken into ac-

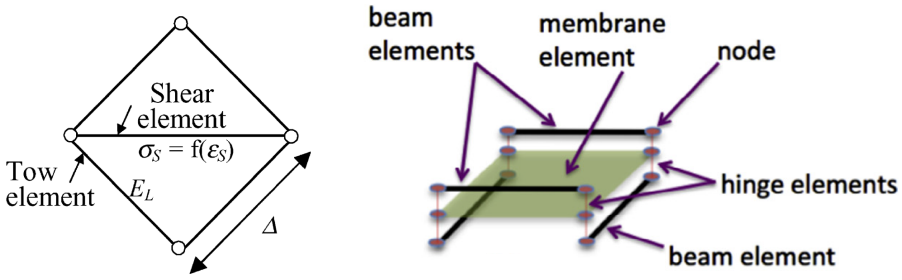

(a) Truss model due to Sharma and Sutcliffe (2004). Reprinted with permission from Elsevier ©.

(b) Beam and membrane model due to Harrison (2016). Source licensed under CC BY 4.0.

Fig. 2.7: Different approaches to discrete modeling.

count by for instance letting beam elements represent the tows (Jauffrès et al., 2010; Dangora et al., 2015). A vertical cantilever bending test was used to obtain the bending properties. The model was validated using a compression test which provided excellent agreement with a simulation. In addition to the out-of-plane bending, in-plane bending was also studied by D'Agostino et al. (2015). The two families of tows in the model are connected by frictionless hinges such that shear can take place while keeping C^1 continuity of the beams. This allowed the model to represent the transition between the different zones in a bias-extension test well. The effect is analogous to the second-gradient theory for continuous models.

Recently, Harrison (2016) developed a model consisting of beam elements to represent the tows and membrane elements to represent the shear behavior. Likewise, the two families of beam elements were connected by frictionless hinges as shown in Fig. 2.7(b). The approach allowed the author to independently control the major deformation modes, and in order to do so, a specific homogenization theory was derived. The model was used to study the effect of bending stiffness on the deformation field of the bias-extension test.

The advantage of the discrete approach is that a simpler material model can be applied to each type of element compared to the continuous approach. Thus, each deformation mode can be controlled more directly. Also, the effect of the changing fiber directions is explicitly taken into account. The disadvantage is that a custom mesh is required which further complicates the use of adaptive meshing as well as application of symmetry (Harrison, 2016). Typically, the mesh size, i.e. distance between tow elements, follows the unit cell size of the fabric. Jauffrès et al. (2010) did, however, report that different mesh sizes would also produce realistic results. In this case, the cross-sectional area and bending stiffness were changed accordingly. Still, more degrees of freedom are necessary in the discrete approach compared to the continuous ap-

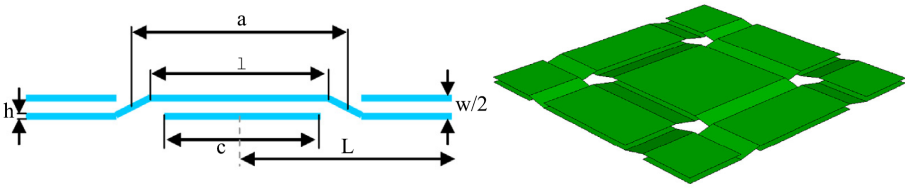

Fig. 2.8: Mesoscopic modeling using a succession of shell element for the tows. Left: Schematic side view. Right: FE unit cell. Reprinted from Gatouillat et al. (2013) with permission from Elsevier ©.

proach which increases the computational cost (Boisse et al., 2008).

A special case of discrete or mesoscopic modeling was presented by Gatouillat et al. (2013). Tows are modeled as a succession of shell elements, and the crimping effect is taken into account in a coarse manner by means of straight lines (see Fig. 2.8). A contact formulation between the elements describes the frictional properties but allows slippage. The mechanical and geometrical parameters in the model were calibrated using the typical uniaxial tension, cantilever bending and picture-frame tests. In a simulation of the bias-extension test, the model's ability to account for slippage was demonstrated. The computational cost is, however, high compared to the other modeling approaches.

2.3 Approximate Modeling

The mechanical models discussed in the previous section typically require an elaborate amount of input data as well as a significant computational effort. Approximate models have also been the focus of some researchers and are discussed in the following.

2.3.1 Kinematic Modeling

The predecessor of the mechanical models is a kinematic representation of the woven fabric. A kinematic model requires little computational effort but can be used to predict the draped configuration of a fabric. The basic idea of the *pin-jointed net* idealization proposed by Mack and Taylor (1956) was introduced in Section 1.5, and extensions of the method are discussed here.

Basically, a fabric modeled as a grid of pin-jointed cells on a mold can be considered as a mechanism which needs constraints to yield a unique solution (Bergsma, 1995). The first set of constraints is the seed point and the fiber directions in the seed point. One typical way of specifying additional constraints is to determine a weft and warp tow path on the mold before the fabric grid is laid out on the mold. The tow paths must pass through

the seed point and can be computed in two ways. The first way is to project the initial tow directions in the seed point onto the mold. The second way is to use geodesic lines emanating from the seed point. A geodesic line can be considered as the straightest possible path on a curved surface. While the former method is simple and gives good predictions for rotationally symmetric molds, it is generally inferior to the latter (Wang et al., 1999).

Other approaches were investigated by Bergsma (1995) and denoted "strategies". One strategy is an iterative procedure involving the difference in angles between adjacent grid cells. A further extension was the implementation of the fabric locking angle as a limit. The angle method and the geodesic line approach were in general found to give good predictions by Wang et al. (1999). It was noted that situations can occur in which the geodesic lines will not constrain the entire area of the fabric in which case the angle method can be applied.

The pin-jointed net model can be implemented using various algorithms. A selection of algorithms together with predefined geodesic tow paths were described and benchmarked by Van Der Weeën (1991). It was found that using linear finite elements and an energy approach based on minimization of the warp and weft strain energy was the most efficient. The kinematic mapping method has also been benchmarked against experimental data, e.g. for draping of prepregs on a cone (Laroche and Vu-Khanh, 1994) and dry and prepreg fabrics on various industrial geometries (Wang et al., 1999). In both studies, good agreements were found. The latter study did see some effects of tow bending with carbon fabrics causing slippage which is not accounted for in the kinematic model.

In the work by Sharma and Sutcliffe (2003), a model framework was proposed in which a combination of kinematic and FE modeling was employed. The authors presented an example with deep drawing of a helmet. In the framework, the fabric was progressively draped in small steps using the kinematic model and subsequently adjusted by means of the FE model.

2.3.2 Fast Process Models

Due to the high computational cost associated with the mechanical models, an effort has also been made to develop faster alternatives that can still take some physical effects into account. This development is closely related to the automation of fabric handling and draping.

Newell and Khodabandehloo (1995) studied the placement of a sheet of prepreg fabric using a robot. It was considered as a 2D problem. For this purpose a large-deflection Bernoulli-Euler beam model was developed to predict the deformed shape. The model evaluation requires an iterative determination of two parameters, which the authors reported took 0.1 s on a personal computer. The overall framework of the research project is described by Buck-

ingham and Newell (1996) who also discuss some gripping and draping strategies. The authors suggest that the plies should be draped in a wave-shape motion away from some initial touch-down point in the middle of the mold.

A type of approximate model often employed for simulating garment fabric consists of particles, i.e. masses connected by springs. See for instance the work by Breen et al. (1994) who used the Kawabata Evaluation System to provide physical input data to their static model. A dynamic particle model was later developed by Eberhardt et al. (1996).

Ben Boubaker et al. (2007) presented a model consisting of a grid of bars connected by springs at the cross-over points. The model can account for tool contact and is evaluated by minimizing the total potential energy. Although it gives realistic predictions, it is also computationally expensive to evaluate due to many DOF.

A large-deflection orthotropic plate model for robot manipulation of fabrics was evaluated using the finite-difference method in the study by Do et al. (2006). The model is flexible in terms of boundary conditions from grippers and the mold. The trade-off between accuracy and computational effort can be controlled by adjusting the finite difference grid spacing. In the validation, a rectangular ply was free-hanging from the grippers, and it proved reasonably accurate in comparison to experimental data.

Lin et al. (2009) presented a large deflection shell model for real-time prediction of the ply deformation during robot manipulation. The model is linear elastic and can be evaluated analytically for some boundary conditions. A comparison with an FE model showed good agreement for three cases of boundary conditions.

A force-based robotic framework was developed by Flixeder et al. (2017) for draping strips of fabric onto single-curved molds. The fabric is gripped in both ends, and the draping is assisted by means of a consolidation roller. To this end, the authors applied a catenary model to predict the fabric shape online. A catenary model was e.g. also employed by Larsen et al. (2017) for robot motion planning of fabric manipulation.

2.4 Summary of Literature Review

The literature review presented in this chapter has revealed numerous publications relevant to the characterization and modeling of prepregs for automated draping processes. Experimental test methods for the major deformation modes have been investigated, and many studies deal with the issue of improving the validity of the tests and their associated data treatment procedures. As previously stated, the choice of a particular test is strongly linked to the simulation model to which it will provide input. Many different modeling approaches have been reported. To that end, the advanced state-of-the-art

mechanical models reviewed can take the following effects into account:

- In-plane extension.
- In-plane shear.
- Out-of-plane bending.
- In-plane bending.
- Rate-dependency or viscoelasticity.
- Shear-tension coupling.
- Plasticity or hysteresis.
- Tow slip or unweaving.

It must, however, be mentioned that all of the above effects have not been implemented in a single model, which would also increase the computational cost immensely.

The publications reviewed in this chapter will serve as the foundation to address the research questions from Section. 1.7, which is the topic of the following chapter.

3

Results and Conclusions of the PhD Project

> “ Both of the simulated draping sequences resulted in wrinkles but the wave shape strategy performed slightly better. ”
>
> – Krogh et al. (2019a), Paper A

As an appetizer for the chapter, this quote encapsulates some core keywords of the PhD project: “simulation”, “wrinkles” and “wave shape strategy”. On the basis of the project objectives presented in Section. 1.7 and the literature review in the previous chapter, the results and conclusions of the PhD project are now presented. First, a description of each journal paper and its contributions are given. This is followed by an overall conclusion of the project.

3.1 Description of Papers

The following sections provide a summary of the three appended journal papers which constitute the backbone of the thesis. In short, Paper A establishes the numerical framework for modeling the prepreg plies during draping, Paper B examines the shear properties of the prepreg ply more closely and Paper C deals with the concept of draping sequence generation using optimization.

3.1.1 Paper A

Modeling the robotic manipulation of woven carbon fiber prepreg plies onto double curved molds: A path-dependent problem

In Krogh et al. (2019a), a numerical framework or *Virtual Draping Environment* (VDE) for planing and simulating draping sequences for the FlexDraper system is established. In the paper, the VDE is used to investigate the path-dependency of the draping problem. The VDE consists of three stages: In the first stage, a kinematic mapping method is used to obtain target points for the grippers on the mold surface. In the second stage, a motion planner is used to generate the draping sequence, i.e. gripper trajectories, based on the initial gripper positions and the gripper target points on the mold. In the third and final stage, the draping sequence is simulated using a transient FE model of the robot tool, the ply and the mold. The focus of the paper is on the first and third stage, whereas only a simple motion planning scheme is employed (the motion planning is the topic of Paper C).

Albeit the kinematic mapping model is simple, it is still applicable in this context due to the low curvatures of the molds in the project. Thus, the model can predict where the grippers ideally should be at the end of the draping sequence. Naturally, the model can not take any information about how the grippers reach these positions into account. This is the reason for applying the transient FE model.

The literature review in the previous chapter shed light upon the state-of-the-art mechanical models developed by different research groups. The built-in Abaqus *fabric* phenomenological material model is able to take most of the relevant physical effects into account and was therefore chosen as the platform for the mechanical modeling. The scope of the paper is thus not to develop a new mechanical model because the current state-of-the-art modeling, including implementations in commercial software, was found adequate. The fabric material model is based on a reinforcement fabric with two structural directions, and the material data is input as nominal stress-strain curves for each fiber direction and for in-plane shear. To take the rate-dependency of the prepreg material into account, stress-strain curves at different strain rates can be input which are then interpolated in the material model. Permanent deformation can also be specified in the model, although that was not considered in the present study. The material model was implemented in shell elements such that the out-of-plane bending stiffness can be modeled. The ply-mold interface is described by a Coulomb friction model, and the ply-gripper interface is tied, i.e. assuming perfect adhesion with the gripper.

Material characterization in the form of uniaxial tension tests in the fiber directions, bias-extension tests and cantilever tests was conducted. Regarding the bias-extension test, the data acquisition did not involve an optical measure of the shear angles which was justified from reports in the literature concerning bias-extension testing of prepregs. It was further assessed from the tested samples that slipping of tows was insignificant for the shear angles in consideration (the shear properties of the prepreg ply is revisited in Paper B). The cantilever test was used to determine the out-of-plane bending

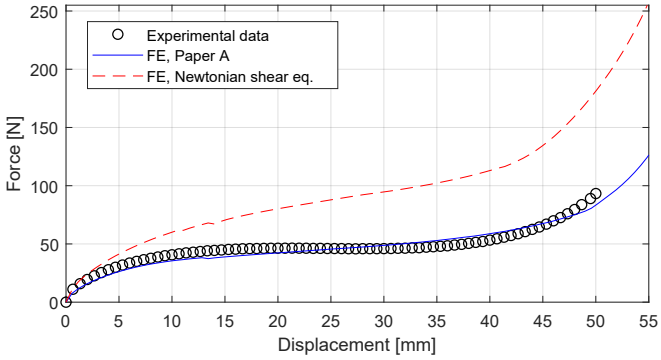

(a) Force-displacement curves for bias-extension test at 100 mm/min. "FE, Newtonian shear eq." refers to the use of Eq. (2.4) for data processing.

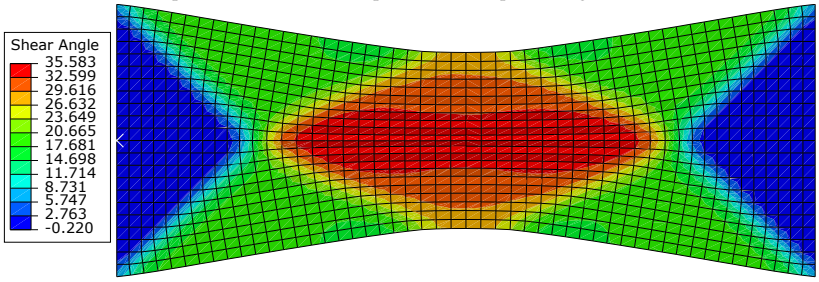

(b) Shear angles in FE simulation of bias-extension test. The displacement is 37 mm which corresponds to a kinematic shear angle of 34° in the center region.

Fig. 3.1: Bias-extension test for verification of FE model from Paper A.

properties of the ply by recording the deflection over time using image processing. Based on models reported in the literature, the right bending stiffness in the shell element model was achieved by adjusting the fiber direction compressive stiffness. This adjustment was achieved using an inverse model and the bending test results. More specifically, the inverse modeling framework was able to create a number of compressive stress-strain curves with corresponding strain rates for the fiber directions. Inputting these results to the fabric material model yielded rate-dependent bending. The material model was, among others, verified using a simulation of the bias-extension test. This verification was not presented in the paper but is shown in Fig. 3.1.

In the results section of the paper, the FE model was first validated using a simple 4-gripper test setup. Next, two different draping sequences were simulated which are both based on a simple linear interpolation in space, between the initial gripper positions and their corresponding target points. In the first sequence, all grippers move simultaneously towards the mold, whereas in the second sequence, the grippers move in groups forming a wave shape motion. The latter sequence was created based on experience from manual layup. It

was concluded that the second sequence is superior although it still left wrinkles on the mold in the draped configuration. This is the motivation for the investigation in Paper C.

The contributions of the paper include the Virtual Draping Environment in which models of different complexity are combined for planning and simulating draping sequences, and the experimental and numerical framework for introducing rate-dependent bending in Abaqus fabric by means of compressive stress-strain curves and corresponding strain rates. The comparison of the two draping sequences and the path-dependency is also a highlight, although it is only a first step on the way.

Drape Trials at FlexDraper Workshop

The FE model presented in Paper A was tested at a FlexDraper workshop with drape trials on mold for a generic aerospace part. The FE model prediction of the draped configuration is shown in Fig. 3.2(a) and the predicted ply-mold difference is visualized as a contour plot in Fig. 3.2(b). The implemented preliminary wave shape draping sequence generated by SDU performed well overall, but resulted in the formation of air pockets, particularly at the corner of maximum x and y values. The air pockets in this region are evident from the photo of the draped ply in Fig. 3.2(c) and were also predicted well by the FE model. After debulking, wrinkles formed in this region of the ply as shown in Fig. 3.2(d).

3.1.2 Paper B

Picture-Frame Testing of Woven Prepreg Fabric: An Investigation of Sample Geometry and Shear Angle Acquisition

In Krogh et al. (2019c) the picture-frame test is applied to further investigate the shear properties of the woven prepreg fabric. The investigation serves two purposes: The first purpose is to explore possible improvements to the common test practice. The second purpose is to check the validity of the bias-extension test used for shear characterization in Paper A. The common test practice of the picture-frame test typically reported in the literature involves a cruciform sample mounted in the picture-frame rig. The frame is deformed by means of a constant crosshead rate, and the shear angles of the fabric are either assumed to follow the frame angle or checked using DIC.

In the study of the paper, the influence of the arms of the cruciform was checked by modifying the samples. One family of modified samples had cut slits in the arms, and the other family had the resin dissolved and the transverse tows removed in the arms. The hypothesis was that the sample arms would contribute to the measured shear load and affect the uniformity of the shear angles in the gage area. A constant crosshead rate will cause an

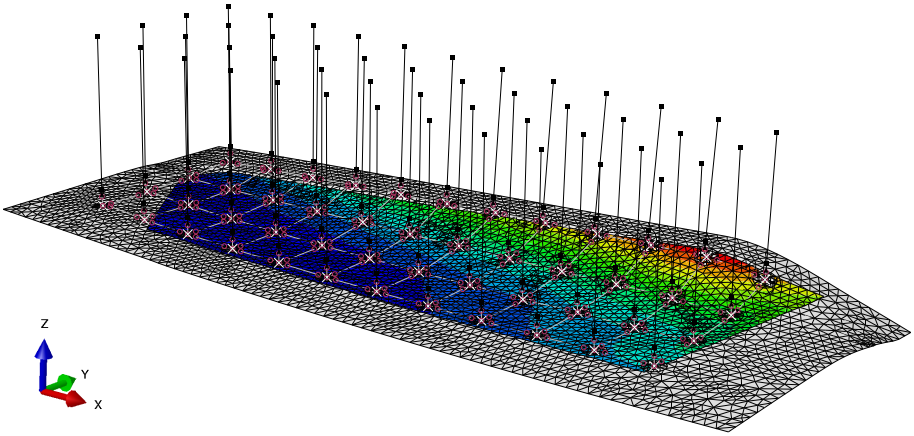

(a) FE model including tool in draped configuration. The contour colors scale with the z coordinate.

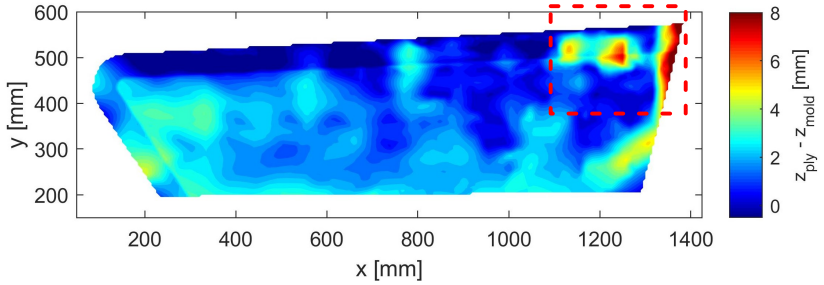

(b) FE model prediction of difference between ply and mold in draped configuration. The red dashed box encloses an area with critical air pockets.

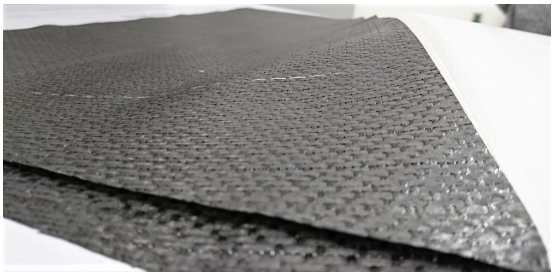

(c) Air pockets in draped ply. The location corresponds to the red dashed box in Fig. 3.2(b).

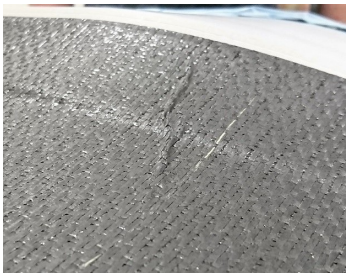

(d) Wrinkles developed from air pockets during debulking.

Fig. 3.2: Numerical and experimental drape trials from FlexDraper workshop.

increasing shear rate of the frame during the course of the test, cf. Eq. (2.5). It is desirable, e.g. for the purpose of inputting the data to Abaqus fabric, to obtain the shear characteristic at a constant shear rate. Therefore, a non-linear expression yielding a constant shear rate was implemented in the test machine control software by means of approximating linear segments. Fi-

nally, it was investigated if the shear angles of the sample could be automatically identified directly from the weave texture using image processing. More specifically, the Hough transform algorithm for identifying straight lines in images was applied. The benefits of the approach are that no patterning is necessary, and that shear angles can also be identified in the initial state, i.e. before frame displacement.

The results of the sample modification showed that a sample with cut slits had a slightly more uniform distribution of shear angles in the gage area compared to the standard sample, but a sample with the transverse tows removed had an inferior shear angle uniformity. The latter result was among others attributed to the fact that those samples were more difficult to install properly in the frame. Still, DIC showed that the average shear angles followed the frame angles well for all sample configurations. The important conclusions were that wrinkling was diminished, and that the shear load was reduced with the sample arm modifications.

The image processing approach for obtaining the shear angles showed promise. Noise was present in the measurements, and therefore a good deal of filtering was applied. Nevertheless, the results predicted the same trends as the DIC results, and the average shear angles were very reasonable. Finally, the picture-frame data were compared to bias-extension data. Good agreement was found for the picture-frame data with the transverse tows removed. Here, the data was normalized by assuming that only the gage area contributes to the shear load, cf. Eq. (2.7). An interesting result was that if the standard sample data was normalized, assuming that the entire sample area contributes to the shear load, then also good agreement was found.

The contributions of the paper include the sample modification study applied to woven prepreg fabric. Testing at a constant shear rate is not a new concept, but the implementation as linear segments is an aid if a high-end testing machine is not available. Lastly, the application of the Hough transform to identify shear angles from the weave texture during a shear test is also a scientific contribution.

3.1.3 Paper C

Generation of Feasible Gripper Trajectories in Automated Composite Draping by means of Optimization

In Krogh et al. (2019b) the motion planning part of the Virtual Draping Environment from Paper A is revisited. The study takes as its point of departure the *MiniDraper* (Fig. 1.6(b), p. 7) because it allows for direct control of the translational degrees of freedom. The idea is to generate feasible draping sequences for which the ply response during draping is taken into account. The computational cost of the nonlinear FE model inhibits its use in an optimiza-

tion framework intended for a reconfigurable robot system. The first step was therefore to develop a computationally efficient fabric model.

Based on the reports in the scientific literature and the experience from the previous studies on characterization and modeling, it was decided to base the model on cables with bending stiffness. The cables are suspended between the grippers, including diagonally across the grid. Evaluation of the model requires determination of some parameters such that the right cable arc lengths are obtained. This determination is achieved in a minimization scheme using semi-analytical gradients. The contact formulation of the cable model was implemented such that portions of cable segments inside a contact tolerance are fixed to the mold. The result is an infinite friction, no-separation formulation.

Two different parameterizations for the optimization framework were discussed. In the first approach, the design variables control the complete trajectories for the grippers to their respective target points on the mold. In the second approach, which was adopted, the design variables control incremental movements of the grippers and meticulous choice of the optimization criteria will ensure a wave shape drape motion. This wave shape motion strategy was first discussed and tested in Paper A.

The basic idea of the chosen optimization criteria is first to create contact between the ply and the mold at a seed point. From here, the wave motion will propagate by minimizing the difference in angle between the ply and the mold at the contact front (indicated by α in the top part of Fig. 3.3). Constraints ensure alignment and prevent the occurrence of multiple, separate contact regions, which can lead to wrinkling or bridging of the ply.

The numerical results of the paper first showed the applicability of the method for a simple 2D problem. Next, the 3D cable model was compared to the nonlinear rate-dependent FE model from Paper A with good agreement. The results section was concluded with two 3D optimization examples. The first 3D example used a 2×2 grid of grippers and a mostly convex mold. The second 3D example used a 3×2 grid and a mold which has both a convex and concave region. While the generated draping sequence was successful for the first 3D example, the concave mold region in the second 3D example caused some minor ply bridging. The remaining part of the ply was draped correctly. Remedies to mitigate this bridging was discussed at the end of the paper.

An intermediate step of the 2nd 3D example (3×2 grippers) is shown in Fig. 3.3 along with the prediction of the FE model described in Paper A. To match the assumptions of the approximate model, the FE contact formulation between the mold and the ply has been augmented with a "no separation" condition which inhibits ply movement normal to the mold surface after contact. The validity of this assumption has to be further investigated, but it is enforced here for the purpose of comparison. Also, the kinematics of the grip-

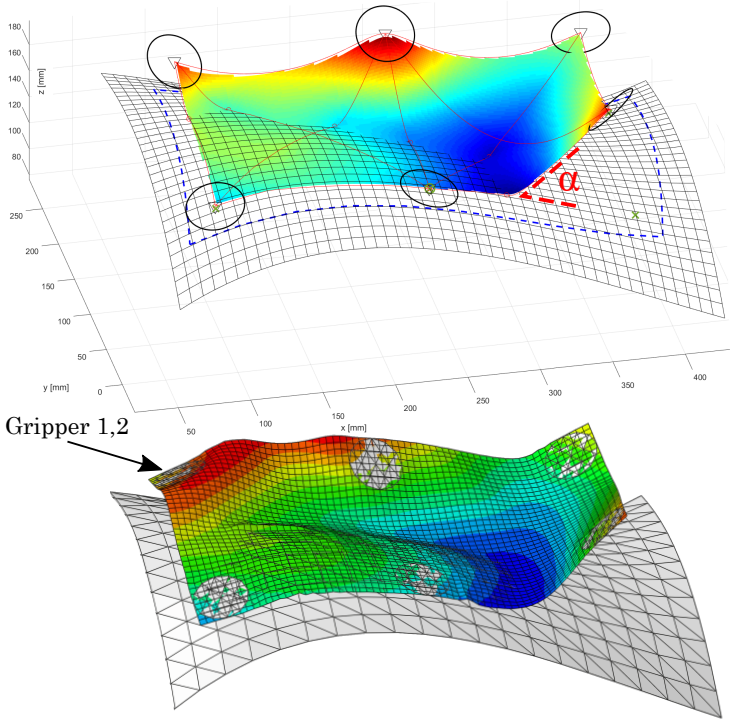

Fig. 3.3: Intermediate step in 3D draping example: Approximate cable model used for optimization (top) and FE model described in Paper A with added "no separation contact" (bottom).

pers in the FE model has been changed to reflect the MiniDraper hardware. A reasonable agreement is seen, except for the region near gripper 1,2 where the two models predict different gripper rotations. Subsequently, small wrinkles develop in the FE model in this ply region and remain in the draped configuration. The remaining part of the draped configuration matches well between the two models, including the bridging at the concave mold region. An experimental validation can provide further insight into the issues and is discussed in the next chapter in Section 4.3.

The contributions of the paper include the computationally efficient 3D fabric model based on cables with bending stiffness. The proposed optimization framework for trajectory generation for a robot system with controllable grippers is likewise a contribution to the research within automated composite draping.

3.2 Conclusion

The fruitful results of the papers, which were summarized in this chapter, support the validity of the project research hypothesis: Numerical analysis, with input from material characterization, is indeed a valuable tool for predicting potential defects in automated composite draping as well as generating feasible draping sequences. The research questions are now addressed:

3.2.1 Which experimental test methods are suitable to characterize the deformation mechanisms of prepreg ply?

As previously stated, the choice of test method is strongly linked to the simulation model to which it provides input. This study has focused on fiber tension, in-plane shear and out-of-plane bending for a continuous formulation. The automated draping process with the gripper grid is not expected to induce large tensions in the fiber directions of the ply. In fact, ply sliding on a gripper is more likely to occur and is discussed in the next chapter in Section 4.1. For this reason, it can be assumed that fiber tensions in the weft and warp directions can be decoupled. Likewise, the shear-tension coupling can be neglected. Under these assumptions, the uniaxial tension test is considered adequate.

For shear characterization with the bias-extension test, tow slipping can be an issue, and in addition, the data processing is subject to some uncertainty. For draping onto mold surfaces of low curvature, the shear locking angle is not reached, and therefore the requirements to the test are lowered. To that end, it was found that tow slipping appeared to be insignificant for the tested shear angles, which is probably due to the resin. In fact, it is the same phenomenon that necessitated the dissolving of the resin to facilitate the removing of the transverse tows in Paper B. Likewise, the data processing was found to yield realistic results, e.g. when simulating the bias-extension test. Furthermore, in the comparison between the picture-frame test and the bias-extension test in Paper B, good agreement between the results was seen. Thus, for the present purpose, the bias-extension test yields adequate results. In Paper B, it was further shown that a test machine can be programmed using linear segments to yield a constant shear rate which is applicable for input to Abaqus fabric.

Out-of-plane bending was characterized using a free-hanging horizontal cantilever test. The test setup is simple but also yielded some scatter in the data. The results, i.e. rate-dependent bending input in the FE model, were, however, satisfying. Yet, a vertical cantilever test with an actuator and a load cell is easy to construct and would probably be a good improvement.

3.2.2 How can the ply material behavior and the kinematics of the FlexDraper tool be captured in a high fidelity predictive simulation model?

There is a great amount of publications regarding different modeling approaches in the scientific literature. A majority of the mechanical models apply the FE method implemented in various commercial softwares. The benefits are that the FE method is well-proven, and that the commercial softwares have interfaces that facilitate pre- and post-processing of data. Scripting is also a convenient option with e.g. Abaqus. The pre-processing allows to easily import mold and ply geometries. Likewise, modeling of the gripper grid as well as the ply-mold and ply-gripper interfaces can be accomplished using built-in components.

Researchers often implement self-developed routines for the material behavior. Yet, for this project, the built-in material model *fabric* was found adequate. Implemented in shell elements, the model is able to account for in-plane fiber tension, rate-dependent shear and rate-dependent out-of-plane bending. Input to the material model was obtained using the material characterization discussed in Section 3.2.1. Further, the model has the option of accounting for permanent deformation. Such a model is state-of-the-art.

Post-processing allows to evaluate the ply-mold difference, i.e. wrinkling and bridging. Likewise, the ply boundary can be evaluated and compared to its prescribed value. Finally, local fiber angles can be checked, although that was not investigated in this study.

3.2.3 What are the important ply deformation mechanisms to account for in an approximate model?

The main requirement to an approximate model is that it is able to represent the displacement field of the ply between the grippers of the grid. Operating the robot system in displacement control, an accurate force prediction is not critical. Therefore, the high fiber-direction stiffness of the plies entails that the fiber direction can be considered inextensible in an approximate model. The model must be able to shear, but as previously noted, shear locking is not expected to be a cause of wrinkling. It was for instance shown in the results of Paper A that wrinkling can occur without shear locking. Thus, the most important deformation mode to account for is out-of-plane bending, which, in the literature, is considered important for the shape of wrinkles. Rate-dependency can be circumvented in the model, for instance by inputting values of a constant-rate bending stiffness and targeting this rate when generating the robot trajectories. Another important aspect is that the model must be able to account for varying boundary conditions, i.e. from the grippers and the mold.

The above discussion was the motivation for basing the approximate model on cables with bending stiffness. A small-sag assumption together with a linear curvature definition was used. A possible improvement to these restraints is discussed in the next chapter in Section 4.2.

3.2.4 How can gradient-based optimization be utilized for determining robot draping sequences?

Two different parameterizations were discussed in Paper C. The idea of the first parameterization is to let controllable splines define the trajectories and simulate an entire draping sequence. The idea of the second parameterization is to control the grippers incrementally based on the ply response. The second parameterization was adopted and implemented. It proved successful as seen with the numerical results. The main drawback is the specification of optimization settings and parameters required for the criteria. All of these parameters have a physical meaning, and therefore the parameters could for instance be changed adaptively as suggested in Paper C. However, a revisit to the spline parameterization could also be interesting. It is believed that fewer parameters are necessary compared to the incremental movement scheme. In fact, the optimization problem could maybe be formulated as *unconstrained*. The drawback of the spline parameterization is that more design variables are needed for the spline control points, and that an objective function evaluation would require a simulation of the entire draping sequence after which the draped result on the mold can be evaluated.

The above discussion basically concerns the computational time, but it is equally important to limit the need for human interaction in the process. The former can somewhat be improved with hardware upgrades and parallel computations. If a hierarchy of ply models with increasing fidelity is established, the generation of feasible gripper trajectories along with the validation could become more efficient and operate more or less automatically.

4

Future Work

> “ Automation offers the greatest possibilities for improvement to the manufacturing process, as this gives higher quality and consistency in the products. In order to achieve this level of skill, an automated system will need to be able to handle, manipulate and shape prepreg sheets in a controlled manner. ”
>
> – Newell and Khodabandehloo (1995)

The results presented in the previous chapter show promise but are only a step on the way towards automated prepreg draping. To be able to improve handling, manipulation and shaping in a controlled manner, some extensions of the PhD work are discussed in this chapter. First, some general thoughts and ideas are presented. Next, three specific topics are addressed in greater detail: modeling the ply-gripper interface in the finite element (FE) model, accounting for large deflections in the approximate model, and validation of the generated draping sequences on the robot system.

As discussed in Section 3.2.4, a hierarchy of models is beneficial for an effectively automatic process for draping sequence generation. An early development of the high fidelity FE model was presented in Krogh et al. (2017) as a linear elastic, rate-independent FE model. This model is less computationally expensive than the nonlinear, rate-dependent FE model and could be included in the hierarchy. Other approaches, such as mass-spring particle models, could also be investigated.

For monotonous draping problems, dissipation or permanent deformation can be neglected, but it is not certain that draping sequences for the robot system will be monotonous. One example could be pre-shearing of the ply before draping, as discussed in Paper C. To this end, the current high fi-

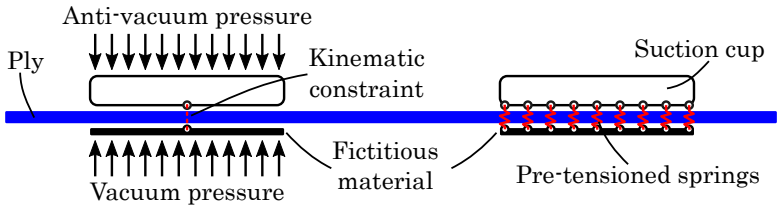

Fig. 4.1: Different modeling approaches for ply-gripper interface. Left: application of pressure. Right: pre-tensioned springs.

delity model can readily be extended with permanent shear deformation. The behavior must be characterized, e.g. using the bias-extension test including unloading.

For characterizing unloading of the bias-extension test, an optical measure of the shear angles is necessary, because the shear angles might not follow the kinematics. To that end, the Hough transform approach developed in Paper B is useful. Further developments, to reduce the noise and determine the optimal algorithm settings is appropriate.

Although a feasible draping sequence should not involve relative movement between the ply and the grippers, and, respectively, the ply and the mold, these effects should probably be represented better in the high fidelity model. Experimental testing can clarify if for instance the mold-ply friction model should include rate-dependency. When draping more than one ply, the mold surface will be covered with the previous plies which further complicates the interface modeling. A starting point for the friction characterization could be the benchmark paper by Sachs et al. (2014). The topic of the ply-gripper interface is considered in the next section.

4.1 Modeling the Ply-Gripper Interface

As discussed in Section 3.2.1, sliding of the ply on the gripper grid is an interesting effect to account for in the high fidelity model. Equally important is the possibility of separation, i.e. a movement normal to the gripper surface. Yet, even in the absence of visual relative movement, the ply is likely to deform locally at the gripper interface which is inhibited with the current tie contact. This section presents the results of a preliminary study that was conducted with the purpose of introducing relative movement in the ply-gripper interface in the FE model.

A difficulty is that the vacuum pressure must move with the suction cup, but act on the ply. Two different modeling approaches that can readily be implemented in commercial FE software were developed and are illustrated in Fig. 4.1. Both of the approaches rely on a rigid representation of the lower

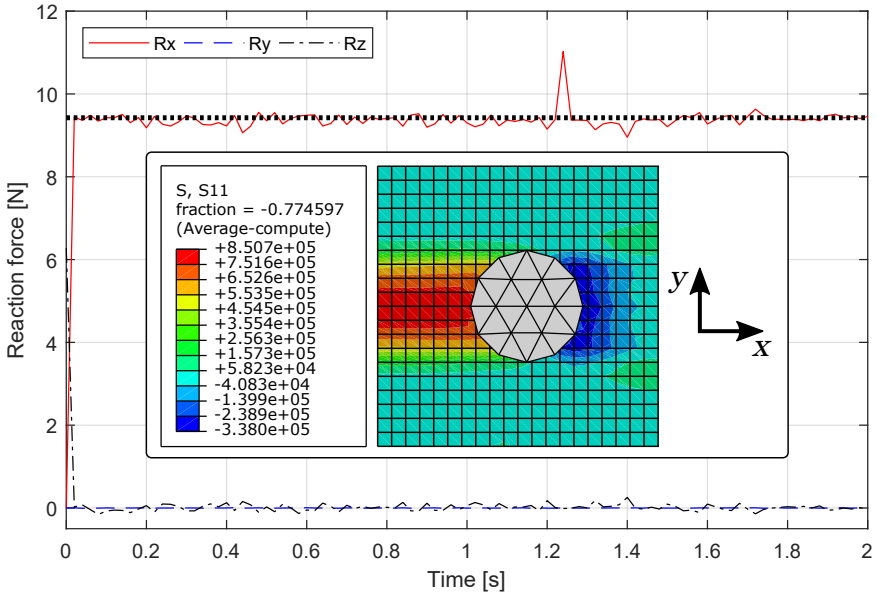

Fig. 4.2: Sliding of suction cup on ply. The graph shows the components of the gripper reaction force over the course of the analysis. The figure embedded in the graph shows a contour plot of x-direction stresses in the deformed model.

suction cup surface, and a fictitious membrane material with weak properties between which the ply is clamped. The clamping is achieved either with an added pressure or with pre-tensioned springs.

In terms of the pressure approach, it is seen in Fig. 4.1, left, that a kinematic constraint keeps the fictitious material in place under the suction cup. A pressure must be added at both the bottom of the fictitious material and at the top of the suction cup in order to ensure static equilibrium. The drawback of this approach is that the pressure remains on the ply after separation, and thus the results are only valid until the point of separation. This issue is alleviated in the spring approach shown in Fig. 4.1, right. The characteristic of the spring is chosen such that the resulting force of all the springs corresponds to the vacuum pressure, until a certain value of elongation, i.e. normal separation, is reached. After this point of elongation, the stiffness can be dropped to an insignificant value to represent separation. The drawback of the spring approach is that the introduction of springs can affect the stable time increment and the robustness of the solution.

Different interface models can be applied for the interaction between the suction cup and the ply, for instance a Coulomb model for sliding friction and a cohesive zone model for sticky normal separation. The fictitious material must have frictionless interface properties.

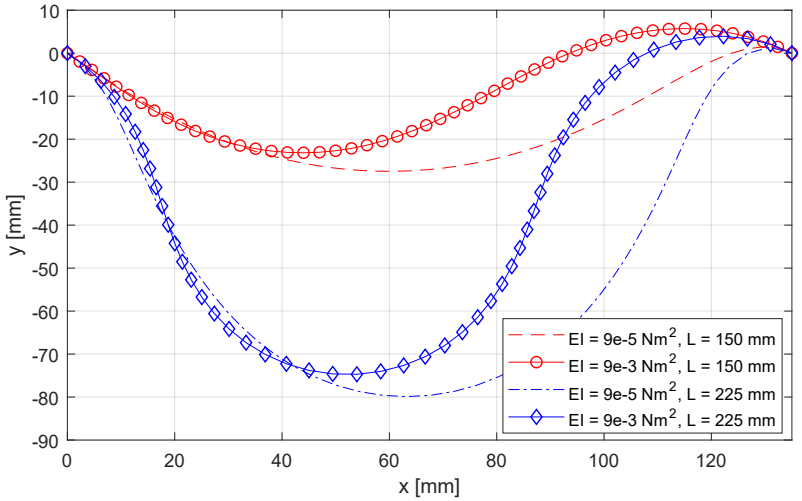

Fig. 4.3: The influence of bending stiffness and length on the deformation of elastica. The span between the supports is 135 mm. The left and right edges are fixed at a rotation angle of -40° and 30°, respectively. The weight per unit length, mg, is 12.26 N/m as in Paper C.

A numerical result with the pressure approach is presented in Fig. 4.2. The setup is a rectangular ply clamped at the edges and with a gripper (40 mm diameter) attached to the surface. A pressure of 0.05 bar is applied which corresponds to a resulting force of 6.28 N. A Coulomb model with a coefficient of friction equal to 1.5 is implemented whereby the theoretical sliding reaction force is 9.4 N. During the analysis, the gripper is displaced across the ply at 4 mm/s for 2 s. The resulting reaction forces of the gripper are reported in Fig. 4.2 and the top view of the deformed model is embedded in the graph. The spikes of the "Rx" force are due to numerical instabilities of the ply. As is evident from the contour plot, compressive stresses build up in front of the sliding gripper. This instability issue must be addressed. Still, the approach is simple to implement, and the preceding discussion works as a proof of concept. The spring approach yields similar results, hence a further investigation will clarify which approach is more suitable.

4.2 Large-Deflection Approximate Model

A solution to the small-sag and linear curvature limitations of the cable model presented in Paper C is introduced in this section. The starting point could be the nonlinear cable differential equation, but a different formulation is investigated here. The idea is to divide the curve into a number of segments and use a minimization of the total potential energy to find the deformed

configuration satisfying the boundary conditions. This kind of model is also known as a Hencky bar-chain model. The approach using the total potential energy avoids another drawback of the linear cable model, i.e. the fact that the unknown variable for the cable arc length determination is the reaction force. When the cable is in compression, there is a risk of finding a feasible but not necessarily physical solution as discussed in Paper C. The solution is likely to depend on the initial guess for the energy minimization routine, but the relation between displacement field and reaction force is not evident. As a consequence, it is unlikely to obtain the desired configuration by choice of the initial guess. This issue is alleviated with the energy approach because the unknowns and thereby the initial guess involves the displacement field.

The total potential energy is given as $\Pi = U + \Omega$. Here U is the strain energy in the material, and Ω is the potential of externally applied loads (Cook et al., 2002). In the present formulation it is assumed that the cables are inextensible. The strain energy arises from bending, and the external loads arise from gravity in the negative z-direction. Hence:

$$U = \int_0^L \frac{M^2}{2\,EI}\,\mathrm{d}s \quad ,\Omega = -\int_0^L mg\,z\,\mathrm{d}s \tag{4.1}$$

In the formulas, M is the bending moment and EI and mg are the flexural rigidity and weight per unit length, respectively. In the numerical implementation, the integrals are replaced by sums of the contributions from each segment. Some results with the energy approach are presented in Fig. 4.3 and show the influence of bending stiffness and length on the predicted deformation field. The red dashed curve has the same properties that were used for determining the cable model material data in Paper C and agrees very well with the cable solution. The formulation shows robustness even for high values of the bending stiffness.

In addition to the introduction of large-deflection cables, another enhancement in the approximate model could be to account for the physical dimensions of the grippers, which was neglected in Paper C. The refinement of the model must always be assessed with regard to the increase in solution time. This evaluation will ensure acceptable reconfiguration times for the flexible robot system. Another critical point is the accuracy of the approximate model and thereby the validity of the generated gripper trajectories. This validation is addressed in the next section.

4.3 Validation of the Generated Draping Sequences

An experimental evaluation of the generated draping sequences will serve to validate or indicate improvements to both the approximate model and the high fidelity model. Recently, a working prototype of the MiniDraper tool

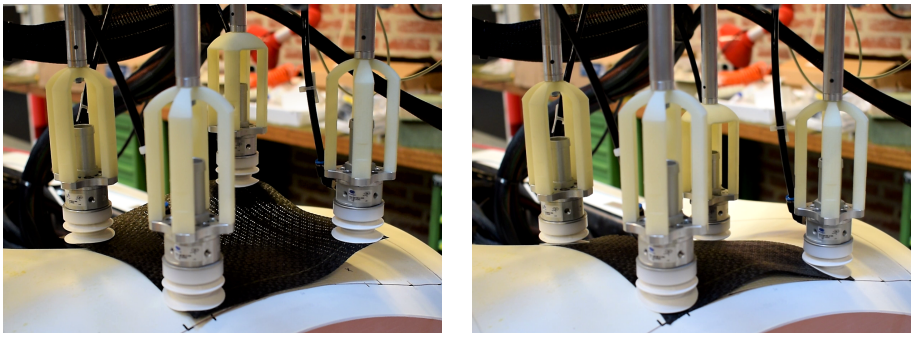

(a) Experimental draping results.

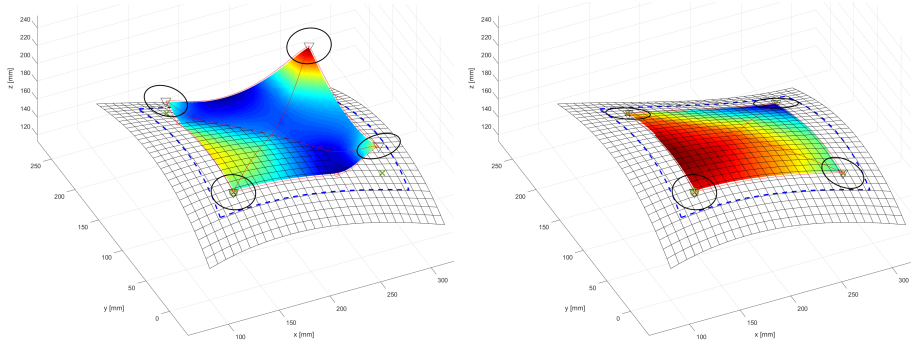

(b) Approximate model predictions. The contour colors of the ply scale with the absolute z-coordinate (height).

Fig. 4.4: Preliminary validation using MiniDraper prototype: intermediate step (left) and draped configuration (right).

(Fig. 1.6(b), p. 7) with a grid of 2×2 grippers was completed and it allows for a preliminary validation. The trajectory optimization program presented in Paper C was adapted to account for the hardware and a draping sequence was generated for the setup used in the first 3D example of Paper C. An intermediate result and the draped configuration is shown in Fig. 4.4(a) along with the corresponding predictions of the approximate model in Fig. 4.4(b). Overall, a good agreement is seen. In the draped configuration of the experiment, a small gap exist between the ply and the mold at two of the edges. This issue arose due to some minor sliding of the ply on the grippers, but also due to the provisional manual calibration and manual installation of the ply on the grippers. The sliding effect does highlight the usefulness of an improved ply-gripper interface representation in the FE model as discussed in Section 4.1. Nevertheless, in the experiment, a subsequent manual consolidation step caused the the ply to make complete contact with the mold without introducing wrinkles. This promising result will be the starting point for a more quantitative validation.

References

Aimene Y, Vidal-Salle E, Hagege B, Sidoroff F, Boisse P (2010) A Hyperelastic Approach for Composite Reinforcement Large Deformation Analysis. Journal of Composite Materials 44(1):5–26, DOI 10.1177/0021998309345348

Akkerman R, Haanappel SP, Sachs U (2018) History and future of composites forming analysis. In: IOP Conference Series: Materials Science and Engineering, IOP Publishing, vol 406, p 012003, DOI 10.1088/1757-899X/406/1/012003

Allaoui S, Boisse P, Chatel S, Hamila N, Hivet G, Soulat D, Vidal-Salle E (2011) Experimental and numerical analyses of textile reinforcement forming of a tetrahedral shape. Composites Part A: Applied Science and Manufacturing 42(6):612–622, DOI 10.1016/j.compositesa.2011.02.001

Alsayednoor J, Harrison P, Yu WR (2017) Influence of specimen pre-shear and wrinkling on the accuracy of uniaxial bias extension test results. Composites Part A: Applied Science and Manufacturing 101:81–97, DOI 10.1016/j.compositesa.2017.06.006

Alshahrani H, Hojjati M (2017) A new test method for the characterization of the bending behavior of textile prepregs. Composites Part A: Applied Science and Manufacturing 97:128–140, DOI 10.1016/j.compositesa.2017.02.027

Arora JS (2012) Introduction to Optimum Design, 3rd edn. Academic Press, Waltham, MA, DOI 10.1016/C2009-0-61700-1

Badel P, Vidal-Sallé E, Boisse P (2008) Large deformation analysis of fibrous materials using rate constitutive equations. Computers and Structures 86(11-12):1164–1175, DOI 10.1016/j.compstruc.2008.01.009

Bassett RJ, Postle R, Pan N (1999) Experimental Methods for Measuring Fabric Mechanical Properties: A Review and Analysis. Textile Research Journal 69(11):866–875, DOI 10.1177/004051759906901111

Belytschko T, Liu WK, Moran B (2000) Nonlinear Finite Elements for Continua and Structures. John Wiley & Sons

Ben Boubaker B, Haussy B, Ganghoffer JF (2007) Discrete models of woven structures. Macroscopic approach. Composites Part B: Engineering 38(4):498–505, DOI 10.1016/j.compositesb.2006.01.007

Bergsma OK (1995) Three Dimensional Simulation of Fabric Draping. Phd thesis, Delft University of Technology

de Bilbao E, Soulat D, Hivet G, Gasser A (2010) Experimental Study of Bending Behaviour of Reinforcements. Experimental Mechanics 50(3):333–351, DOI 10.1007/s11340-009-9234-9

Boisse P, Gasser A, Hivet G (2001) Analyses of fabric tensile behaviour: Determination of the biaxial tension-strain surfaces and their use in forming simulations. Composites - Part A: Applied Science and Manufacturing 32(10):1395–1414, DOI 10.1016/S1359-835X(01)00039-2

Boisse P, Hamila N, Helenon F, Hagege B, Cao J (2008) Different approaches for woven composite reinforcement forming simulation. International Journal of Material Forming 1(1):21–29, DOI 10.1007/s12289-008-0002-7

Boisse P, Hamila N, Vidal-Salle E, Dumont F (2011) Simulation of wrinkling during textile composite reinforcement forming. Influence of tensile, in-plane shear and bending stiffnesses. Composites Science and Technology 71(5):683–692, DOI 10.1016/j.compscitech.2011.01.011

Boisse P, Hamila N, Guzman-Maldonado E, Madeo A, Hivet G, Dell'Isola F (2017) The bias-extension test for the analysis of in-plane shear properties of textile composite reinforcements and prepregs: a review. International Journal of Material Forming 10(4):473–492, DOI 10.1007/s12289-016-1294-7

Boisse P, Colmars J, Hamila N, Naouar N, Steer Q (2018) Bending and wrinkling of composite fiber preforms and prepregs. A review and new developments in the draping simulations. Composites Part B: Engineering 141:234–249, DOI 10.1016/j.compositesb.2017.12.061

Breen DE, House DH, Wozny MJ (1994) A Particle-Based Model for Simulating the Draping Behavior of Woven Cloth. Textile Research Journal 64(11):663–685, DOI 10.1177/004051759406401106

Buckingham RO, Newell GC (1996) Automating the manufacture of composite broadgoods. Composites Part A: Applied Science and Manufacturing 27(3 PART A):191–200, DOI 10.1016/1359-835X(96)80001-9

Cao J, Akkerman R, Boisse P, Chen J, Cheng HS, de Graaf EF, Gorczyca JL, Harrison P, Hivet G, Launay J, Lee W, Liu L, Lomov SV, Long A, de Luycker E, Morestin F, Padvoiskis J, Peng X, Sherwood JA, Stoilova T, Tao

X, Verpoest I, Willems A, Wiggers J, Yu T, Zhu B (2008) Characterization of mechanical behavior of woven fabrics: Experimental methods and benchmark results. Composites Part A: Applied Science and Manufacturing 39(6):1037–1053, DOI 10.1016/j.compositesa.2008.02.016

Cherouat A, Billoët JL (2001) Mechanical and numerical modelling of composite manufacturing processes deep-drawing and laying-up of thin pre-impregnated woven fabrics. Journal of Materials Processing Technology 118(1-3):460–471, DOI 10.1016/S0924-0136(01)00987-6

Chu CC, Cummings CL, Teixeira NA (1950) Mechanics of Elastic Performance of Textile Materials: Part V: A Study of the Factors Affecting the Drape of Fabrics—The Development of a Drape Meter. Textile Research Journal 20(8):539–548, DOI 10.1177/004051755002000802

Cook RD, Malkus DS, Plesha ME, Witt RJ (2002) Concepts and applications of finite element analysis, 4th edn. John Wiley & Sons, New York

D'Agostino MV, Giorgio I, Greco L, Madeo A, Boisse P (2015) Continuum and discrete models for structures including (quasi-) inextensible elasticae with a view to the design and modeling of composite reinforcements. International Journal of Solids and Structures 59:1–17, DOI 10.1016/j.ijsolstr.2014.12.014

Dangora LM, Mitchell CJ, Sherwood JA (2015) Predictive model for the detection of out-of-plane defects formed during textile-composite manufacture. Composites Part A: Applied Science and Manufacturing 78:102–112, DOI 10.1016/j.compositesa.2015.07.011

Dangora LM, Mitchell C, White KD, Sherwood JA, Parker JC (2018) Characterization of temperature-dependent tensile and flexural rigidities of a cross-ply thermoplastic lamina with implementation into a forming model. International Journal of Material Forming 11(1):43–52, DOI 10.1007/s12289-016-1327-2

Denis Y, Guzman-Maldonado E, Hamila N, Colmars J, Morestin F (2018) A dissipative constitutive model for woven composite fabric under large strain. Composites Part A: Applied Science and Manufacturing 105:165–179, DOI 10.1016/j.compositesa.2017.11.018

Do D, John S, Herszberg I (2006) 3D deformation models for the automated manufacture of composite components. Composites Part A: Applied Science and Manufacturing 37(9):1377–1389, DOI 10.1016/j.compositesa.2005.07.011

Dong L, Lekakou C, Bader MG (2001) Processing of Composites: Simulations of the Draping of Fabrics with Updated Material Behaviour Law. Journal of Composite Materials 35(2):138–163, DOI 10.1177/002199801772661975

Eberhardt B, Weber A, Strasser W (1996) A fast, flexible, particle-system model for cloth draping. IEEE Computer Graphics and Applications 16(5):52–59, DOI 10.1109/38.536275

Elkington M, Ward C, Chatzimichali A, Potter KD (2015) Studying effects of preshearing on hand layup. Advanced Manufacturing: Polymer & Composites Science 1(2):80–93, DOI 10.1179/2055035914y.0000000007

Ferretti M, Madeo A, Dell'Isola F, Boisse P (2014) Modeling the onset of shear boundary layers in fibrous composite reinforcements by second-gradient theory. Zeitschrift fur Angewandte Mathematik und Physik 65(3):587–612, DOI 10.1007/s00033-013-0347-8

Flixeder S, Glück T, Kugi A (2017) Force-based cooperative handling and layup of deformable materials: Mechatronic design, modeling, and control of a demonstrator. Mechatronics 47:246–261, DOI 10.1016/j.mechatronics.2016.10.003

Gatouillat S, Bareggi A, Vidal-Sallé E, Boisse P (2013) Meso modelling for composite preform shaping - Simulation of the loss of cohesion of the woven fibre network. Composites Part A: Applied Science and Manufacturing 54:135–144, DOI 10.1016/j.compositesa.2013.07.010

Gereke T, Döbrich O, Hübner M, Cherif C (2013) Experimental and computational composite textile reinforcement forming: A review. Composites Part A: Applied Science and Manufacturing 46:1–10, DOI 10.1016/j.compositesa.2012.10.004

Gong Y, Peng X, Yao Y, Guo Z (2016) An anisotropic hyperelastic constitutive model for thermoplastic woven composite prepregs. Composites Science and Technology 128:17–24, DOI 10.1016/j.compscitech.2016.03.005

Grosberg P, Park BJ (1966) The Mechanical Properties of Woven Fabrics: Part V: The Initial Modulus and the Frictional Restraint in shearing of Plain Weave Fabrics. Textile Research Journal 36(5):420–431, DOI 10.1177/004051756603600505

Guzman-Maldonado E, Hamila N, Boisse P, Bikard J (2015) Thermomechanical analysis, modelling and simulation of the forming of pre-impregnated thermoplastics composites. Composites Part A: Applied Science and Manufacturing 78:211–222, DOI 10.1016/j.compositesa.2015.08.017

Hamila N, Boisse P (2007) A meso-macro three node finite element for draping of textile composite preforms. Applied Composite Materials 14(4):235–250, DOI 10.1007/s10443-007-9043-1

Hamila N, Boisse P, Sabourin S, Brunet M (2009) A semi-discrete shell finite element for textile composite reinforcement forming simulation. International Journal for Numerical Methods in Engineering 79:1443–1466, DOI 10.1002/nme.2625

Harrison P (2016) Modelling the forming mechanics of engineering fabrics using a mutually constrained pantographic beam and membrane mesh. Composites Part A: Applied Science and Manufacturing 81:145–157, DOI 10.1016/j.compositesa.2015.11.005

Harrison P, Clifford M, Long A (2004) Shear characterisation of viscous woven textile composites: A comparison between picture frame and bias extension experiments. Composites Science and Technology 64(10-11):1453–1465, DOI 10.1016/j.compscitech.2003.10.015

Harrison P, Abdiwi F, Guo Z, Potluri P, Yu WR (2012) Characterising the shear-tension coupling and wrinkling behaviour of woven engineering fabrics. Composites Part A: Applied Science and Manufacturing 43(6):903–914, DOI 10.1016/j.compositesa.2012.01.024

Harrison P, Taylor E, Alsayednoor J (2018) Improving the accuracy of the uniaxial bias extension test on engineering fabrics using a simple wrinkle mitigation technique. Composites Part A: Applied Science and Manufacturing 108:53–61, DOI 10.1016/j.compositesa.2018.02.025

Hu JL, Zhang yT (1997) The KES Shear Test for Fabrics. Textile Research Journal 67(9):654–664, DOI 10.1177/004051759706700904

Iwata A, Inoue T, Naouar N, Boisse P, Lomov SV (2019) Coupled meso-macro simulation of woven fabric local deformation during draping. Composites Part A: Applied Science and Manufacturing 118:267–280, DOI 10.1016/j.compositesa.2019.01.004

Jauffrès D, Sherwood JA, Morris CD, Chen J (2010) Discrete mesoscopic modeling for the simulation of woven-fabric reinforcement forming. International Journal of Material Forming 3(SUPPL. 2):1205–1216, DOI 10.1007/s12289-009-0646-y

Jones RM (1999) Mechanics of composite materials, 2nd edn. Taylor and Francis Group, New York

Kaiser B, Pyttel T, Duddeck F (2019) A generalised method for the coupling of a parallelogram-like unit cell with a macroscopic finite element to simulate the behaviour of textiles. International Journal of Material Forming, in press, DOI 10.1007/s12289-019-01472-9

Kang T, Yu W (1995) Drape Simulation of Woven Fabric by Using the Finite-element Method. Journal of the Textile Institute 86(4):635–648, DOI 10.1080/00405009508659040

Kawabata S (1980) The standardization and analysis of hand evaluation. Textile Machinery Society of Japan, Osaka

Khan MA, Mabrouki T, Vidal-Salle E, Boisse P (2010) Numerical and experimental analyses of woven composite reinforcement forming using a hypoelastic behaviour. Application to the double dome benchmark. Journal of Materials Processing Technology 210(2):378–388, DOI 10.1016/j.jmatprotec.2009.09.027

Khan MA, Reynolds N, Williams G, Kendall KN (2015) Processing of thermoset prepregs for high-volume applications and their numerical analysis using superimposed finite elements. Composite Structures 131:917–926, DOI 10.1016/j.compstruct.2015.06.056

Komeili M, Milani AS (2016) On effect of shear-tension coupling in forming simulation of woven fabric reinforcements. Composites Part B: Engineering 99:17–29, DOI 10.1016/j.compositesb.2016.05.004

Krieger H, Kaufmann D, Gries T (2015) Kinematic drape algorithm and experimental approach for the design of tailored non-crimp fabrics. Key Engineering Materials 651-653:393–398, DOI 10.4028/www.scientific.net/KEM.651-653.393

Krogh C, Glud JA, Jakobsen J (2017) Modeling of prepregs during automated draping sequences. In: AIP Conference Proceedings, AIP Publishing, vol 1896, p 030036, DOI 10.1063/1.5008023

Krogh C, Glud JA, Jakobsen J (2019a) Modeling the robotic manipulation of woven carbon fiber prepreg plies onto double curved molds: A path-dependent problem. Journal of Composite Materials 53(15):2149–2164, DOI 10.1177/0021998318822722

Krogh C, Sherwood JA, Jakobsen J (2019b) Generation of Feasible Gripper Trajectories in Automated Composite Draping by means of Optimization. submitted

Krogh C, White KD, Sabato A, Sherwood JA (2019c) Picture-frame testing of woven prepreg fabric: An investigation of sample geometry and shear

angle acquisition. International Journal of Material Forming, in press, DOI 10.1007/s12289-019-01499-y

Laroche D, Vu-Khanh T (1994) Forming of Woven Fabric Composites. Journal of Composite Materials 28(18):1825–1839, DOI 10.1177/002199839402801805

Larsen L, Kaspar M, Schuster A, Vistein M, Kim J, Kupke M (2017) Full automatic path planning of cooperating robots in industrial applications. In: 2017 13th IEEE Conference on Automation Science and Engineering (CASE), IEEE, pp 523–530, DOI 10.1109/COASE.2017.8256157

Launay J, Hivet G, Duong AV, Boisse P (2008) Experimental analysis of the influence of tensions on in plane shear behaviour of woven composite reinforcements. Composites Science and Technology 68(2):506–515, DOI 10.1016/j.compscitech.2007.06.021

Lebrun G, Bureau MN, Denault J (2003) Evaluation of bias-extension and picture-frame test methods for the measurement of intraply shear properties of PP/glass commingled fabrics. Composite Structures 61(4):341–352, DOI 10.1016/S0263-8223(03)00057-6

Lee W, Cao J, Badel P, Boisse P (2008) Non-orthogonal constitutive model for woven composites incorporating tensile effect on shear behavior. International Journal of Material Forming 1(SUPPL. 1):891–894, DOI 10.1007/s12289-008-0239-1

Liang B, Hamila N, Peillon M, Boisse P (2014) Analysis of thermoplastic prepreg bending stiffness during manufacturing and of its influence on wrinkling simulations. Composites Part A: Applied Science and Manufacturing 67:111–122, DOI 10.1016/j.compositesa.2014.08.020

Lin H, Clifford M, Taylor P, Long A (2009) 3D mathematical modelling for robotic pick up of textile composites. Composites Part B: Engineering 40(8):705–713, DOI 10.1016/j.compositesb.2009.07.006

Lindberg J, Behre B, Dahlberg B (1961) Shearing and Buckling of Various Commercial Fabrics. Textile Research Journal 31(2):99–122, DOI 10.1177/004051756103100203

Liu L, Chen J, Li X, Sherwood JA (2005) Two-dimensional macro-mechanics shear models of woven fabrics. Composites Part A: Applied Science and Manufacturing 36(1):105–114, DOI 10.1016/j.compositesa.2004.07.004

Lomov SV, Verpoest I, Barburski M, Laperre J (2003) Carbon composites based on multiaxial multiply stitched preforms. Part 2. KES-F characterisation of the deformability of the preforms at low loads. Compos-

ites Part A: Applied Science and Manufacturing 34(4):359–370, DOI 10.1016/S1359-835X(03)00025-3

Lomov SV, Boisse P, Deluycker E, Morestin F, Vanclooster K, Vandepitte D, Verpoest I, Willems A (2008) Full-field strain measurements in textile deformability studies. Composites Part A: Applied Science and Manufacturing 39(8):1232–1244, DOI 10.1016/j.compositesa.2007.09.014

Lukaszewicz D, Ward C, Potter KD (2012) The engineering aspects of automated prepreg layup: History, present and future. Composites Part B: Engineering 43(3):997–1009, DOI 10.1016/j.compositesb.2011.12.003

Machado M, Fischlschweiger M, Major Z (2016a) A rate-dependent non-orthogonal constitutive model for describing shear behaviour of woven reinforced thermoplastic composites. Composites Part A: Applied Science and Manufacturing 80:194–203, DOI 10.1016/j.compositesa.2015.10.028

Machado M, Murenu L, Fischlschweiger M, Major Z (2016b) Analysis of the thermomechanical shear behaviour of woven-reinforced thermoplastic-matrix composites during forming. Composites Part A: Applied Science and Manufacturing 86:39–48, DOI 10.1016/j.compositesa.2016.03.032

Mack C, Taylor HM (1956) The Fitting of Woven Cloth to Surfaces. Journal of the Textile Institute Transactions 47(9):T477–T488, DOI 10.1080/19447027.1956.10750433

Marques O (2011) Practical Image and Video Processing Using MATLAB. John Wiley & Sons, DOI 10.1002/9781118093467

Milani AS, Nemes JA, Lebrun G, Bureau MN (2010) A comparative analysis of a modified picture frame test for characterization of woven fabrics. Polymer Composites 31(4):561–568, DOI 10.1002/pc.20849

Minus ML, Kumar S (2005) The processing, properties, and structure of carbon fibers. JOM 57(2):52–58, DOI 10.1007/s11837-005-0217-8

Newell GC, Khodabandehloo K (1995) Modelling Flexible Sheets for Automatic Handling and Lay-up of Composite Components. Proceedings of the Institution of Mechanical Engineers, Part B: Journal of Engineering Manufacture 209(6):423–432, DOI 10.1243/pime_proc_1995_209_106_02

Nguyen M, Herszberg I, Paton R (1999) The shear properties of woven carbon fabric. Composite Structures 47(1-4):767–779, DOI 10.1016/S0263-8223(00)00051-9

Nosrat-Nezami F, Gereke T, Eberdt C, Cherif C (2014) Characterisation of the shear-tension coupling of carbon-fibre fabric under controlled membrane tensions for precise simulative predictions of industrial preforming

processes. Composites Part A: Applied Science and Manufacturing 67:131–139, DOI 10.1016/j.compositesa.2014.08.030

Pansart S (2013) Prepreg processing of advanced fibre-reinforced polymer (FRP) composites. In: Advanced Fibre-Reinforced Polymer (FRP) Composites for Structural Applications, Woodhead Publishing, chap 6, pp 125–154, DOI 10.1533/9780857098641.2.125

Pasco C, Khan M, Kendall K (2019) A novel discrete method of shear angle measurement for in-plane shear properties of thermoset prepreg using a point-tracking algorithm. Journal of Composite Materials 53(14):2001–2013, DOI 10.1177/0021998318813193

Peirce FT (1930) 26—The "handle" of cloth as a measurable quantity. Journal of the Textile Institute Transactions 21(9):T377–T416, DOI 10.1080/19447023008661529

Peng X, Cao J (2005) A continuum mechanics-based non-orthogonal constitutive model for woven composite fabrics. Composites Part A: Applied Science and Manufacturing 36(6):859–874, DOI 10.1016/j.compositesa.2004.08.008

Peng X, Cao J, Chen J, Xue P, Lussier DS, Liu L (2004) Experimental and numerical analysis on normalization of picture frame tests for composite materials. Composites Science and Technology 64(1):11–21, DOI 10.1016/S0266-3538(03)00202-1

Peng X, Guo Z, Du T, Yu W (2013) A simple anisotropic hyperelastic constitutive model for textile fabrics with application to forming simulation. Composites Part B: Engineering 52:275–281, DOI 10.1016/j.compositesb.2013.04.014

Poppe C, Rosenkranz T, Dörr D, Kärger L (2019) Comparative experimental and numerical analysis of bending behaviour of dry and low viscous infiltrated woven fabrics. Composites Part A: Applied Science and Manufacturing 124:105466, DOI 10.1016/j.compositesa.2019.05.034

Potluri P, Ciurezu DA, Ramgulam RB (2006) Measurement of meso-scale shear deformations for modelling textile composites. Composites Part A: Applied Science and Manufacturing 37(2):303–314, DOI 10.1016/j.compositesa.2005.03.032

Sachs U, Akkerman R (2017) Viscoelastic bending model for continuous fiber-reinforced thermoplastic composites in melt. Composites Part A: Applied Science and Manufacturing 100:333–341, DOI 10.1016/j.compositesa.2017.05.032

Sachs U, Akkerman R, Fetfatsidis K, Vidal-Sallé E, Schumacher J, Ziegmann G, Allaoui S, Hivet G, Maron B, Vanclooster K, Lomov SV (2014) Characterization of the dynamic friction of woven fabrics: Experimental methods and benchmark results. Composites Part A: Applied Science and Manufacturing 67:289–298, DOI 10.1016/j.compositesa.2014.08.026

Sharma SB, Sutcliffe MP (2004) A simplified finite element model for draping of woven material. Composites Part A: Applied Science and Manufacturing 35(6):637–643, DOI 10.1016/j.compositesa.2004.02.013

Sharma SB, Sutcliffe MPF (2003) Draping of woven fabrics: Progressive drape model. Plastics, Rubber and Composites 32(2):57–64, DOI 10.1179/146580103225009149

Sharma SB, Sutcliffe MP, Chang SH (2003) Characterisation of material properties for draping of dry woven composite material. Composites Part A: Applied Science and Manufacturing 34(12):1167–1175, DOI 10.1016/j.compositesa.2003.09.001

Sidhu RM, Averill RC, Riaz M, Pourboghrat F (2001) Finite element analysis of textile composite preforms stamping. Composite Structures 52(3-4):483–497, DOI 10.1016/S0263-8223(01)00038-1

Skordos AA, Monroy Aceves C, Sutcliffe MPF (2007) A simplified rate dependent model of forming and wrinkling of pre-impregnated woven composites. Composites Part A: Applied Science and Manufacturing 38(5):1318–1330, DOI 10.1016/j.compositesa.2006.11.005

Soteropoulos D, Fetfatsidis K, Sherwood JA, Langworthy J (2011) Digital method of analyzing the bending stiffness of non-crimp fabrics. In: AIP Conference Proceedings, AIP Publishing, vol 1353, pp 913–917, DOI 10.1063/1.3589632

Van Der Weeën F (1991) Algorithms for draping fabrics on doubly-curved surfaces. International Journal for Numerical Methods in Engineering 31(7):1415–1426, DOI 10.1002/nme.1620310712

Wang J, Page JR, Paton R (1998) Experimental investigation of the draping properties of reinforcement fabrics. Composites Science and Technology 58(2):229–237, DOI 10.1016/S0266-3538(97)00115-2

Wang J, Paton R, Page JR (1999) Draping of woven fabric preforms and prepregs for production of polymer composite components. Composites Part A: Applied Science and Manufacturing 30(6):757–765, DOI 10.1016/S1359-835X(98)00187-0

Wang J, Long AC, Clifford MJ (2010) Experimental measurement and predictive modelling of bending behaviour for viscous unidirectional composite materials. International Journal of Material Forming 3(SUPPL. 2):1253–1266, DOI 10.1007/s12289-009-0670-y

Yu W, Zampaloni M, Pourboghrat F, Chung K, Kang T (2005) Analysis of flexible bending behavior of woven preform using non-orthogonal constitutive equation. Composites Part A: Applied Science and Manufacturing 36(6):839–850, DOI 10.1016/j.compositesa.2004.10.026

Yu WR, Pourboghrat F, Chung K, Zampaloni M, Kang TJ (2002) Non-orthogonal constitutive equation for woven fabric reinforced thermoplastic composites. Composites Part A: Applied Science and Manufacturing 33(8):1095–1105, DOI 10.1016/S1359-835X(02)00053-2

Zouari B, Dumont F, Daniel J, Boisse P (2003) Analyses of woven fabric shearing by optical method and implementation in a finite element. In: 6th International ESAFORM conference on Material Forming, Salerno, Italy, pp 875–878

Zouari B, Daniel JL, Boisse P (2006) A woven reinforcement forming simulation method. Influence of the shear stiffness. Computers and Structures 84(5-6):351–363, DOI 10.1016/j.compstruc.2005.09.031

Paper A

Modeling the robotic manipulation of woven carbon fiber prepreg plies onto double curved molds: A path-dependent problem

Christian Krogh, Jens A. Glud & Johnny Jakobsen

The paper has been published in the
Journal of Composite Materials Vol. 53(15), pp. 2419–2164, 2019.

The layout has been revised.

Abstract

This paper investigates the behavior of woven prepreg plies being placed on a weakly double curved mold by a robot. It is essential that the draped configuration is free from wrinkles. The baseline is a Virtual Draping Environment (VDE) that can plan and simulate robot draping sequences. It consists of a kinematic mapping algorithm for obtaining target points for the grippers on the mold surface. A simple motion planner is used to calculate the trajectories of the grippers. Here, two conceptually different draping strategies are employed. Finally, the two generated draping sequences are simulated using a transient, nonlinear Finite Element (FE) model and compared w.r.t. their predicted wrinkle formations. Material data is obtained by means of tension, bias-extension and cantilever tests. The numerical examples show that the VDE can aid in developing the automatic draping system but that the generation of feasible draping sequences is highly path dependent and non-trivial.

Keywords Prepregs, draping, finite element modeling, kinematic modeling, automation

A.1 Introduction

Laminated prepreg composites are widely used in the aerospace industry because of their superior mechanical properties. A significant amount of the total cost relates to the manufacturing where e.g. the draping process is accomplished by means of manual labor. Draping concerns the placement of the uncured fabric in a mold. Here, it is essential that the fabric is positioned correctly and is free from wrinkles. Currently, prepreg reinforcement is draped automatically in the industry by means of Automated Tape Laying (ATL) and Automated Fiber Placement (AFP). These methods are, however, restricted to unidirectional prepreg (Lukaszewicz et al., 2012). For components designed with woven fabric as is frequently seen in the aerospace industry, it is of interest to develop an automatic layup solution that can directly substitute the current manual operation. To this end, an understanding of the fabric behavior and computer models of the draping process is needed.

Shearing (or trellising), i.e. rigid tow rotations at the cross-over points, has long been recognized as the most important deformation mechanism when initially flat fabric is deformed on a double curved mold (Cao et al., 2008). Here, the stiffness is several orders of magnitudes lower than the fiber direction stiffness of the fabric. Recently, the out-of-plane bending stiffness has been identified as important for the formation of wrinkles and their shape (Boisse et al., 2011).

The fabric response in shear and tension is the baseline for the early fabric

forming models such as the work by Womersley (1937) and the *pin-jointed net model* by Mack and Taylor (1956). Here, the fibers are considered inextensible while the shear stiffness is zero. The model is quick to evaluate but it is only an idealization of the draped configuration. This type of model is denoted a *kinematic model* as opposed to *mechanical models* which are often accomplished using the Finite Element (FE) method whereby the physics of the material can be taken into account.

One approach within the framework of mechanical models is to consider the fabric as a continuum and use homogenization theory to obtain anisotropic material properties dependent on the fabric deformation. The material model is usually implemented in standard finite elements such as shells. The material properties should preferably be related to experimental data in some way. This was e.g. neatly accomplished by Aimene et al. (2010) who used a hyperelastic potential composed of contributions from fiber tensions and shear. The energy contributions were formulated as polynomials in invariants which were fit to experimental data. The use of invariants facilitated easy calculation of the constitutive law. Other continuous models are also described in the literature (Peng et al., 2013; Yu et al., 2002).

A second mechanical model approach is known as *discrete modeling*. By means of structural finite elements such as trusses, beams and membranes possibly in combination with springs the focus is to model the unit cell of the fabric. E.g. the prepreg fabric model by Skordos et al. (2007) uses a grid of truss element with a bilinear material law to model the tows and nonlinear elastic-viscoplastic diagonal truss elements to model the shear behavior governed by the resin. Other discrete models can also be found in the literature (Jauffrès et al., 2010; Harrison, 2016; Cherouat and Billoët, 2001). The main disadvantage is that a high number of Degrees of Freedom (DOF) usually is needed. Also, the generation of the mesh requires some attention.

Finally, a semi-discrete model, which can be considered as a hybrid between continuous and discrete, was introduced by Hamila et al. (2009) in a self made special purpose finite element. The element was found efficient and easy to relate to experimental data.

The fabric forming models presented above are in many cases used to simulate the deep drawing or press forming of fabrics. The present work takes basis in a newly developed robot system for handling and draping entire prepreg plies onto weakly double curved molds. As it will be shown, the problem is highly path dependent. That is, the draped configuration including possible defects is dependent on the path taken by the robot. Determining a feasible draping sequence from the vast solution space of possible sequences is crucial and relies on modeling. The next section gives an overview of the robot system and the requirements to the modeling. Then, the *Virtual Draping Environment* is presented where kinematic and mechanical based modeling are combined to plan and simulate the draping process.

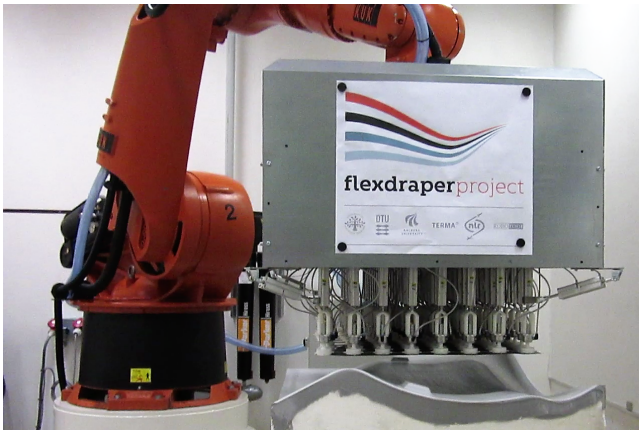

Fig. A.1: The FlexDraper robot cell. The grid of grippers is in the initial configuration over the mold after the ply has been picked up.

Hereafter, material characterization is employed to provide material data input, and a model validation and a further numerical exploration of the path dependency is presented. Finally, the paper is concluded with a discussion.

A.2 Problem Specification

The work presented in this paper is part of the FlexDraper research project, which is briefly introduced in the following. As described in the previous section, the scope of the project is to drape entire prepreg plies onto double curved molds by means of an industrial robot. The project focuses on *weakly double curved* molds, i.e. molds without tight corners, where the plies can be readily draped without the need for post treatment and where the shear angles remain below the locking angle. The robot cell under development is depicted in Figure A.1.

The robot end effector (Figure A.2) consists of a grid of vertically actuated suction cups which will be denoted as *grippers*. The actuators are mounted in universal joints meaning that the horizontal degrees of freedom (DOF) are free. To add constraints, so-called *interlinks* are mounted between the grippers. These bars, mounted in ball joints, maintain the distance between the grippers (also mounted in ball joints) while allowing the grid to shear. Notice, that this setup entails, that only the vertical DOF are controllable.

Measures to evaluate the quality of drapes include a prescribed ply boundary and checks on the fiber angles at certain locations. Naturally, the draped plies must follow the mold surface within tight tolerances (dependent on the industry and product) and be free from wrinkles and air pockets. In the robot

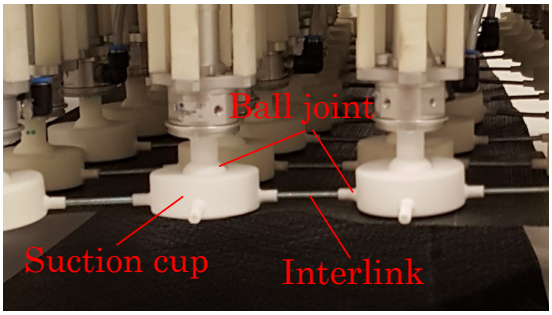

Fig. A.2: The design of the robot tool grid with actuated suction cups connected by interlinks.

cell these checks will be carried out by a vision sensor system but ideally the modeling should detect possible flaws at an earlier stage.

The material system used in this study is a balanced carbon fiber 4-harness satin weave with a Bismaleimide (BMI) resin. The thickness is 0.3 mm and the areal density is 314 g/m^2. The robot system is operated at room temperature, for which reason the temperature dependency of the prepreg is neglected. All experimental work is therefore carried out at room temperature. The resin state could also influence the results. In the present study, the material was used within the processing window specified by the manufacturer.

In this study a self designed 450 mm $\times$ 450 mm double curved mold is used. It has concave and convex parts which will challenge the draping. The mold surface is defined by a 3rd degree polynomial surface:

$$\begin{aligned} z(x,y) = 1.004x + 1.089y - 3.667x^2 - 4.4x\,y - \\ 3.75y^2 + 3.086x^3 + 8.889x^2\,y + 4.321y^3 \end{aligned} \tag{A.1}$$

Here $x \in [0, 0.45]$, $y \in [0, 0.45]$. Using manual layup it was checked that a ply can be draped onto the mold, see Figure A.3.

If a ply can be draped manually onto a mold, one could think it is a trivial task to determine the corresponding robot draping sequence. However, the first attempts with the system under development contradicts this statement. This is exactly the motivation for studying the problem numerically.

A.3 The Virtual Draping Environment

The Virtual Draping Environment (VDE) consists of three components depicted in Figure A.4: A kinematic mapping algorithm for generating gripper target points on the mold surface, a motion planner to calculate the trajectories from the initial configuration of the grippers to the target points and

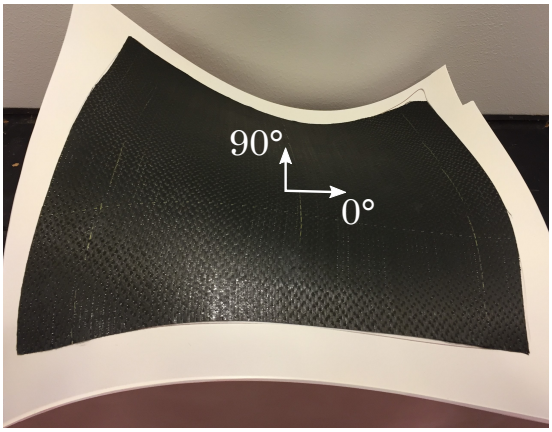

Fig. A.3: The mold used in this study with a manually draped ply on top. The Gaussian curvature range between -25 m^{-2} and 23 m^{-2}.

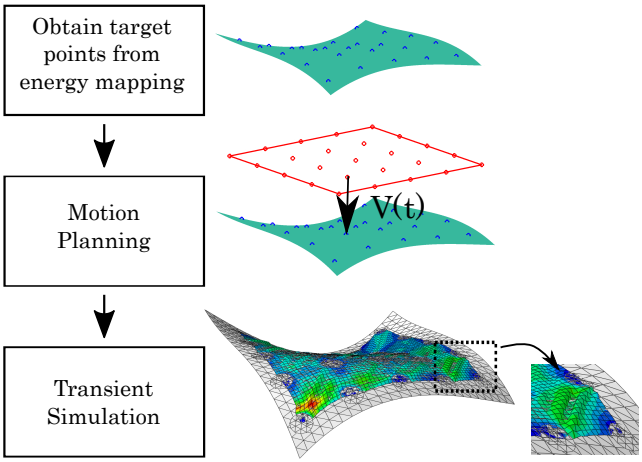

Fig. A.4: The components of the Virtual Draping Environment.

a transient nonlinear Finite Element (FE) model to simulate the draping sequence. The three components are elaborated in the following.

A.3.1 Energy Mapping Algorithm

When the draping process is carried out manually, the boundary of the final geometry is used to guide the ply, e.g. as a laser projection on the mold. This is usually given with the part specification. With the new robot tool, the ply is gripped inside the boundary which is why additional information must be calculated.

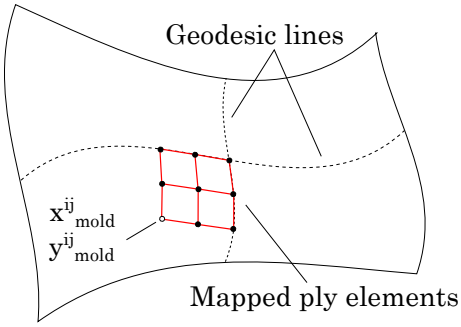

Fig. A.5: Energy mapping algorithm.

The energy mapping algorithm is a purely kinematic model that can determine the map Ψ from the flat ply in $\mathbb{R}^2$ to the draped configuration on the mold in $\mathbb{R}^3$:

$$\{x_{mold}, y_{mold}, z_{mold}\} = \Psi(x_{ply}, y_{ply}) \tag{A.2}$$

The basic assumptions are that the fiber extensional stiffness is infinite and the fabric shear stiffness is zero as proposed by Mack and Taylor (1956). From large deflection shell theory it is known that tensile membrane strains develop when an initially flat sheet undergoes deformations to a finite Gaussian curvature (Lin et al., 2009). This phenomenon is not accounted for. However, as the fabric contains voids and the model is an approximation, the approach is considered valid.

The algorithm used in this study was introduced by Bergsma and Huisman (1988) and later benchmarked (Van Der Weeën, 1991). The ply is discretized into four node quadrilateral elements with a bilinear interpolation. The ply nodes are treated in the mold coordinate system. The algorithm is initiated at a chosen starting point along with two geodesic lines on the mold surface in the direction of weft and warp fiber angles. This will form a starting point from which the ply elements can be mapped The setup is depicted in Figure A.5. The elements are mapped one at the time. For each element mapping, three nodes will be constrained and the free node $x^{ij}_{mold}, y^{ij}_{mold}$, is located by minimizing the fiber strain energy U which is the equivalent of minimizing the fiber strain integrated over the element volume:

$$U(x^{ij}_{mold}, y^{ij}_{mold}) = \int_V \frac{1}{2}\left(\varepsilon^2_{xx} + \varepsilon^2_{yy}\right) \mathrm{d}V \tag{A.3}$$

While this type of model has been superseded by more advanced nonlinear FE models for simulation of industrial draping processes, its application in this context is still valid. The slippage of crossing tows is small for car-

bon/epoxy prepregs as reported by Laroche and Vu-Khanh (1994). The same authors reported fine agreement between the experimental data and the calculations using the pin-jointed net model. Also, the shear angles remain below the locking angle (here $\approx 35^\circ$ shear strain). However, as will become evident in the paper, shear angles below the locking angle does not necessarily alleviate wrinkles.

Once the map has been determined, the gripper target points on the mold surface can be calculated. That is, the coordinates of the grippers in the initial flat configuration can be mapped onto the mold in the final draped configuration.

A.3.2 Motion Planning

With information about the grippers in the initial configuration and in the final configuration, gripper trajectories can be generated. While there are infinitely many ways to construct a trajectory from one point in space to another, a starting point, which is used in this study, is a linear interpolation. That is, each gripper will move with a constant velocity in a straight line from the initial point $\mathbf{P_1}$ to the final point $\mathbf{P_2}$.

The next concern is the pattern in which the grippers are to move. Certain features in the mold may influence in what order different areas of the ply preferably should be draped (Hancock and Potter, 2006). From the hand layup process it is observed that the operators tend to choose some initial contact point, e.g. a corner, from which the ply is draped in a droplet or wave pattern. The immediate benefit of this approach is the avoidance of entrapped air between the mold and the ply. In this study the applicability of the VDE will be investigated by two different gripper move patterns or *draping strategies*:

1. Uniform draping, where all grippers move to the mold simultaneously.
2. Wave shape draping, where groups of grippers with equal distance to some starting point sequentially move to the mold.

To further improve the draping, a so-called *preshape* is employed: Before the draping strategy is executed, the grippers are first moved vertically such that they have equal distance to their respective target points on the mold. The principles in the two draping strategies are depicted in Figure A.6 for a 2D case with three grippers.

Note that the interpolation approach does not include any information about the ply in the states between the initial configuration and the draped configuration. The approach is used as a starting point, but as will become evident in the results section (A.5), it does not necessarily lead to feasible draping sequences.

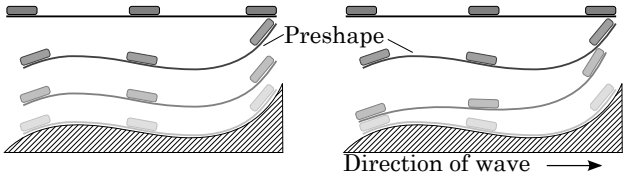

Fig. A.6: Draping strategies. Left: uniform draping, right: wave shape draping.

A.3.3 Transient Nonlinear Finite Element Model

The simulation of the generated draping sequences is carried out using Abaqus Explicit. The model comprises the ply, the mold surface and the contact surfaces of the grippers. The mold and the grippers are treated as rigid whereas the ply is modeled using the Abaqus intrinsic *fabric* material model with nonlinear, rate-depedent behavior. The input to the material model is determined in the next section. The interlinks between the grippers and the offset rotation point of the grippers are modeled by means of Multi Point Constraint (MPC) rigid beam elements as seen in Figure A.7. Connector elements are introduced in the gripper rotation points in order to model a maximum and minimum rotation as well as the actuators and their mounting in the universal joints (two connector elements per gripper).

The phenomenological fabric material model is suitable for woven fabric materials where the weft and warp direction will change during deformation such that they are no longer perpendicular. It allows for capturing the in-plane deformation behaviors, i.e. fiber extension, fiber compression and shear. It is assumed that all deformation modes are decoupled. The model uses nominal stress and strain data at different strain rates as the constitutive law which is convenient to obtain. In the material characterization section (A.4) it becomes evident that an increasing strain rate in general makes the ply response stiffer, i.e. a direct effect of the resin viscosity. Naturally, the model must be used in a geometric nonlinear, finite strain analysis. The outputs include the angle between the weft and warp direction, i.e. the fabric

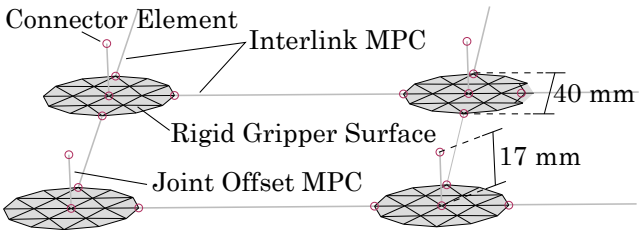

Fig. A.7: Modeling of interlinks and joint offset using Multi Point Constraint (MPC) elements in Abaqus. The attachment of connector elements is also shown.

shear strain (Dassault Systèmes Simulia Corporation, 2014).

The ply is meshed with 4-node shell elements with reduced integration and hourglass control. The plate theory on which the element formulation is based, assumes a first order shear deformation through the thickness. Later in the paper it will be shown, that the shear deformation is an important part of the out-of-plane response. Another point to note regarding the out-of-plane behavior is the fact that it is obtained from the in-plane properties. This is indeed a valid assumption for homogeneous materials, but incorrect for heterogeneous materials like woven fabric. A number of remedies are proposed in the literature of which two are considered in the following due to their ease of implementation.

Döbrich et al. (2014) suggested to introduce three fictitious layers in the shell. The middle layer accounts for the extensional stiffness while the outer layers account for the bending stiffness. In this way the extension and bending are conveniently decoupled and the approach is readily implemented in commercial FE softwares. This approach is valid as long as the axial stiffness of the outer bending layers is much lower than the axial stiffness of the middle extension layer. During characterization of the fabric material in this study, it was found that it exhibits a highly rate dependent behavior in bending. At high strain rates, the bending stiffness becomes significant, for which reason the decoupling is not practical.

The second approach involves adjusting the compressive stiffness in order to get the right bending behavior which causes the effective modulus to be asymmetric (Yu et al., 2005; Dangora et al., 2015). This approach is justified by the fact that relative fiber movement is possible within the tows (both in-plane and out-of-plane). Thus, the compressive stiffness is different and in general lower than the tensile stiffness of the fibers. The downside is that the bending stiffness changes if the ply is subjected to tension. In the present study, however, the bending response is mostly of concern when the ply is sagging. The asymmetric modulus approach is adopted in the present study and details are presented in section A.4.3.

The interface between the grippers and the ply involves the effects of the suction and the frictional resistance which is highly governed by the tackiness of the resin. During the initial testing on the robot system, it was found that the frictional resistance is substantial since grippers push into the ply when picking it up. With the suction on, the ply is kept fixated. Therefore, the grippers in this study are tied to the ply, i.e. modeled as having infinite friction. This approach will constrain the ply material and in reality some deformation underneath the grippers is expected.

In the interface between the ply and the mold, sliding is much more likely to occur. Here, the frictional resistance is approximated by an experimentally determined coefficient of friction of 1.50. The experimental setup was analogous to ASTM Standard D 1894.

By default, the transient FE model is undamped for which reason damping needs to be introduced. In this study, viscous Rayleigh damping is applied due to its numerical advantages. This means, that the damping matrix equals the mass matrix scaled by some constant α. To this end, a value of α that will critically damp the system is desired, i.e. with $\zeta = 1$ in the following formula (Cook et al., 2002):

$$\alpha = 2\zeta\omega_1 \tag{A.4}$$

Here ω_1 is the fundamental eigenfrequency of the system. In the following, the damping behavior is studied by means of a cantilever specimen. The setup is analogous to what will be presented in section A.4.3 where the out-of-plane properties of the prepreg is characterized. Here, the idea is to get an approximate value of α to be used in the FE models.

The frequency ω_1 of the cantilever specimen can e.g. be found by conducting an FE analysis with an undamped ply or approximated from the analytical solution to the dynamic differential equation of the beam. Here, the latter is considered. For linear elastic, isotropic materials, the fundamental eigenfrequency of a beam is given as (Cook et al., 2002):

$$\omega_1 = 1.875^2\sqrt{\frac{E_{static}I}{mL^3}} \tag{A.5}$$

In the formula E_{static} is Young's modulus, I is the moment of inertia, m is the mass of the beam and L is the length. Naturally, this formula can only approximate the fundamental eigenfrequency of a prepreg specimen, as the material cannot be considered linear elastic and isotropic. The unknown quantity in Eq. (A.5), E_{static} is determined as follows. From the experimental results in section A.4.3, the static deflection of a prepreg cantilever specimen is found. Next, an isotropic, large deflection beam is fitted to the experimental static deflection by adjusting Young's Modulus. The resulting value of Young's Modulus is equal to E_{static}. Inserting the values in equation (A.5) the result is $\omega_1 = 11\ \mathrm{s}^{-1}$ and by using equation (A.4) the damping factor becomes $\alpha = 22$. This value is obviously highly model dependent but it will used as a starting point for other analyses.

In the analyses, dynamic effects are small and thus mass scaling is applied to reduce the computation time. The mass is scaled with a factor up to 20. To this end it is checked that the kinetic energy is low compared to the strain energy in the model and that mass scaling does not alter the end result significantly for this kind of problem.

A.4 Material Characterization

This section presents the experimental tests carried out to obtain material data for the Finite Element (FE) model. These encompass tension tests for the fiber direction response, bias-extension tests for the shear response and cantilever tests for the bending response.

All tests were conducted at room temperature on a single ply with the material defrosted accordingly. Tension and bias-extension tests were conducted on an Instron 5568 electromechanical tensile test machine. A source of error which applies to all the tests is the fact that the specimens were cut to fixed dimensions which potentially involves cutting into the tows.

A.4.1 Tension Test

Strips of prepreg material with a width of 25 mm were cut in the fiber direction. The desired gage length is 150 mm. The strips were mounted in the grippers of the tensile test machine which was operated in displacement control until a maximum load of 500 N. Two different crosshead rates were tested: 2 mm/min and 0.5 mm/min.

The specimen deformation should ideally be obtained from a direct measurement, e.g. an extensometer or strain gage, but due to the inhomogeneity of the material this is not practical. Multiple authors have reported successful use of an optical measuring technique, such as Digital Image Correlation (DIC) (Willems et al., 2009; Zhu et al., 2008). The use of DIC was found challenging due to gaps between tows opening and closing during deformation which inhibits the correlation process. To overcome the issues it was decided to use a *compliance compensation* procedure for the tension tests. The system compliance of the tensile test machine was measured by conducting three tests on a steel specimen (grade S355) with a rectangular cross section of 25 mm $\times$ 5 mm and a gage length of 50 mm. This specimen has a stiffness several orders of magnitude higher than the prepreg strips. The specimen was mounted in the same grippers as were used for the prepreg material. At an applied load of 500 N, the theoretical elongation of the steel specimen is:

$$\delta = \frac{FL}{EA} = 0.0012 \text{ mm} \tag{A.6}$$

Here the value of Young's Modulus is assumed to be $E = 200$ GPa. In turn, the maximum displacement of the cross head was 0.1 mm. Thus, the elongation of the steel specimen can be neglected and the response is a measure of the test machine compliance. For reference, the maximum elongations measured during testing of the prepreg were in the order of 1 mm.

The force-displacement data of the steel specimen are subtracted from the

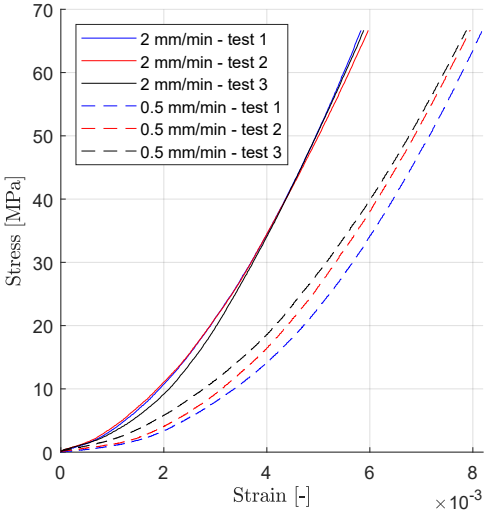

Fig. A.8: Nominal stress-strain response of prepreg material in the 0° direction.

force-displacement data of the prepreg. Next, the compliance compensated prepreg data are converted to nominal stress and strain as follows:

$$\sigma = \frac{F}{A_0} \quad , \varepsilon = \frac{\Delta L}{L_0} \tag{A.7}$$

Here the subscript 0 indicates a quantity in the initial undeformed state. The results are presented in Figure A.8.

From the figure it is seen that the prepreg material shows a non-linear stress-strain behavior. This is expected since the tows are crimped in the unloaded state and will gradually de-crimp during loading. It is also evident that the response is rate dependent which can be accredited to the presence of the resin and its straining during decrimping of the tows. As a simplification in the FE model, it is assumed that the fiber response is rate-independent. This is justified by the fact that shearing is the predominant deformation mechanism during forming. For the FE model input, the stress-strain response obtained at 2 mm/min is used.

A.4.2 Bias-extension Test

The bias-extension test is a common method for measuring the shear response of fabric. Various authors have benchmarked this test against another method, the picture frame test (Lebrun et al., 2003; Harrison et al., 2004). The bias-extension test was chosen based on the aforementioned benchmarks due

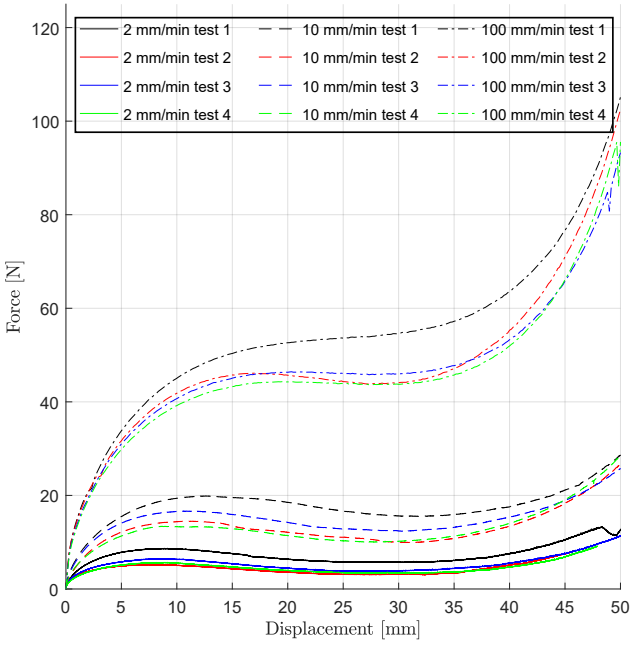

Fig. A.9: Force vs. crosshead displacement for bias-extension tests.

to its simplicity and ease of application.

In the test, a wide sample of the prepreg material with fibers in $\pm 45^\circ$ is clamped in grippers at the top and bottom. When the height is at least twice the width, a pure shear zone will theoretically exist in the middle. For this study the width is 120 mm and the desired gage length is 270 mm. The tensile test machine is operated in displacement control at three different cross head rates: 2 mm/min, 10 mm/min and 100 mm/min. The results are presented in Figure A.9.

The figure shows families of curves with three distinct parts: First, a steep part ($\approx$ 0-10 mm in 100 mm/min test), then a plateau ($\approx$ 10-35 mm in 100 mm/min test) and finally another steep part ($\approx$ 35-50 mm in 100 mm/min test). The first steep part corresponds to in-plane fiber bending where the tows remain fixed at the cross-over points (Grosberg and Park, 1966). When the frictional resistance at the cross-over points is exceeded, the tows begin to rotate and thus, the response is governed by friction effects. This corresponds to the plateau part. When neighboring tows come in contact and change cross-sectional shape, the force increases and the *locking angle* is eventually reached (Nguyen et al., 1999). This is evident as the final steep part. Throughout the entire deformation intra-ply slippage is possible. As previously noted, the resin helps to keep the tows in place. Also, reports in the

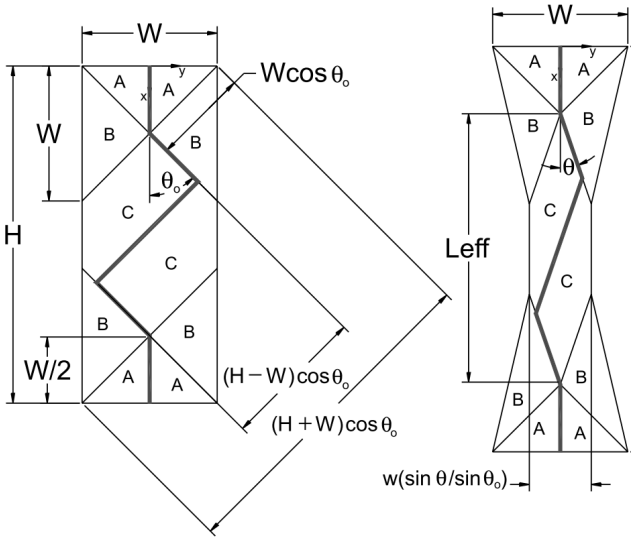

Fig. A.10: Kinematics of the bias-extension test (Lebrun et al., 2003).

literature show that slippage is small below 40° shear (Boisse et al., 2017; Harrison et al., 2005). Assuming three distinct shear zones in the sample (see Figure A.10), a relation between the cross head movement δ and the shear angle γ in the pure shear zone, C can be derived (Lebrun et al., 2003):

$$\gamma = 90^\circ - 2\cos^{-1}\left(\frac{L_0 + \delta}{\sqrt{2}L_0}\right) \tag{A.8}$$

Here the original length of zone C is given as $L_0 = H - W$. Equation (A.8) assumes that no intra-ply slippage occurs and thus, ideally the shear strain should be measured using e.g. DIC. The shear strain rate is found by differentiating equation (A.8) w.r.t. time:

$$\dot{\gamma} = \frac{\sqrt{2}}{L_0 \sin\theta}\dot{\delta} \tag{A.9}$$

So while $\dot{\delta}$ is constant within a test, $\dot{\gamma}$ will increase with increasing shear strain due to $\sin\theta$ entering the equation. In order to obtain constant rate curves, a C^1 continuous interpolated surface of the form $F = F(\gamma, \dot{\gamma})$ is created, where F is the cross head force. One representative set of data from each of the three testing rates (2, 10 and 100 mm/min) are used as input in the interpolation. Now, slices of the surface are taken at the initial strain rates of the tests yielding three constant rate cross head force vs shear angle curves.

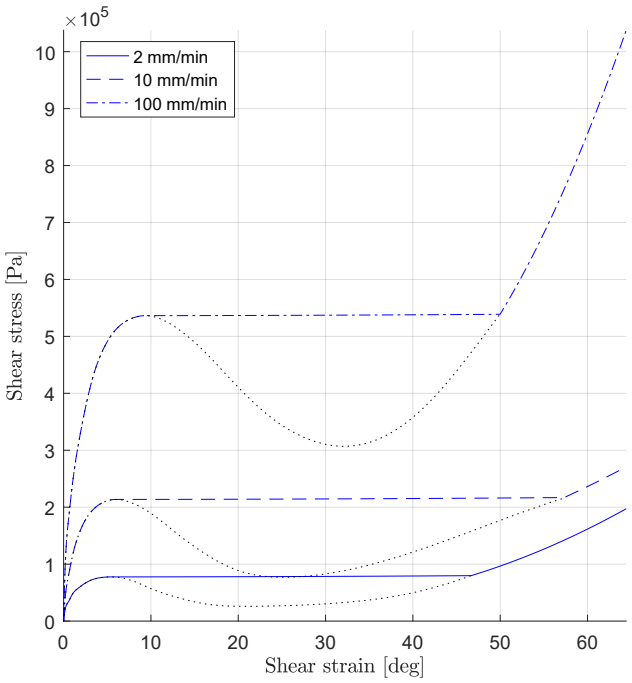

Fig. A.11: Shear stress vs shear strain for bias-extension tests.

Using energy equilibrium the normalized shear force per unit length is derived to (Cao et al., 2008):

$$F_{sh}(\gamma) = \frac{1}{(2H - 3W)\cos\gamma}\left[\left(\frac{H}{W} - 1\right) F\left(\cos\frac{\gamma}{2} - \sin\frac{\gamma}{2}\right) - W F_{sh}\left(\frac{\gamma}{2}\right)\cos\frac{\gamma}{2}\right] \tag{A.10}$$

Notice how the force evaluated at a shear angle γ depends on the force evaluated at the half shear angle $\frac{\gamma}{2}$. Thus, the expression must be evaluated iteratively. The nominal shear stress τ is found by division with the initial thickness.

A shear stress vs shear angle curve for each cross head rate is presented in Figure A.11. In the figure, black dotted lines are drawn in the plateau-region. These lines correspond to the actual calculated shear stresses which are seen to exhibit negative stiffnesses. To avoid instability during the FE solution, the corrected curves with a flat plateau region are used.

In Figure A.9 the force drop in the plateau region is also visible. One pos-

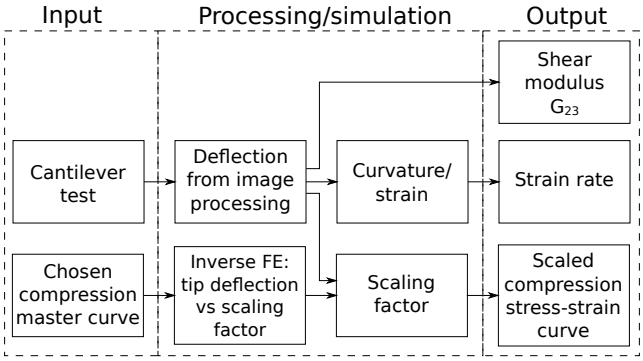

Fig. A.12: Method to obtain stress-strain curve and strain rate from cantilever test.

sible explanation for the drop is relaxation of the material, but this is not investigated further. It must also be pointed out that equation (A.10) was derived for rate-independent materials. Harrison et al. (2004) proposed another formula for rate-dependent materials assuming Newtonian fluid behavior. This approach avoids the negative stiffness, but the Newtonian assumption also introduces errors. Because the material exhibits a rate-dependency, it follows that it has non-Newtonian behavior. In this study, the rate-independent results with negative stiffness correction in Fig. A.11 will be used. This decision is made based on Finite Element simulations of the bias-extension test using the two approaches.

A.4.3 Cantilever Test

As introduced previously, the bending behavior of the material model is controlled by the compressive stiffness. Thus, this section presents the methodology to measure the out-of-plane deformation of the prepreg material and calculate a number of compression stress-strain curves with corresponding strain rates. The end result is introduction of rate-dependent bending in the FE-model. The cantilever test is chosen due to its simple setup and the fact that the loading from gravity is well known. See e.g. Alshahrani and Hojjati (2017) for an overview of the various bending test methods.

The basic idea is to capture the deflection of the specimen over time. Based on the deflection, the strain rate as function of time is obtained. Then by using an inverse model approach and the tip deflection of the specimen at different time stamps, compression stress-strain curves are obtained. These steps are outlined in the flowchart in Figure A.12 and elaborated in the following.

In the test, the specimen are cut to a width of 25 mm and clamped at one end such that the free length is 150 mm. The free part is held horizontal by a support, which is removed upon start of the test. The experiment is run for 6

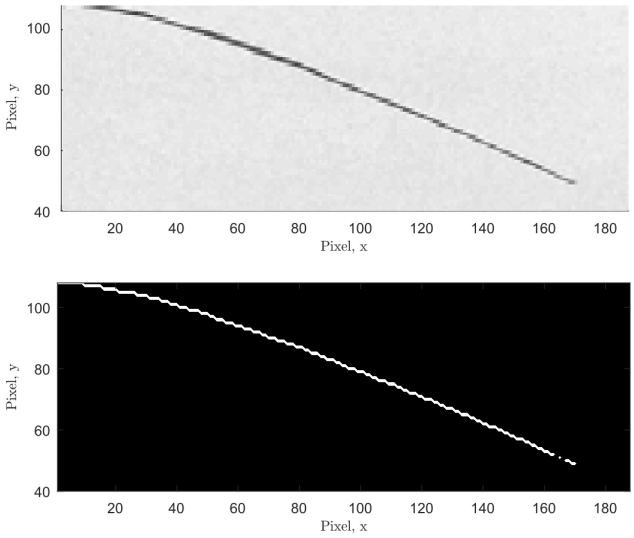

Fig. A.13: Image processing of cantilever test. Top: grayscale image, bottom: binarized and eroded image.

minutes until no further deformation is visible. Four samples of 0° and five samples of 90° specimens are tested.

For the data processing, the method used by Liang et al. (2017) (see also Dangora et al. (2015)) makes up the baseline. It consists of taking a still image of the deflecting specimen, using image processing to extract the midline and fitting a continuous smooth function from which it is possible to obtain the moment-curvature relation. Here, slight modifications are introduced. Instead of still images, a video of the deflecting specimen is recorded whereby the time aspect is taken into account.

The recorded video is handled using MATLAB's Image Processing Toolbox. For each chosen frame, the image is binarized using a global gray level threshold value. Small areas less than some pixel tolerance are removed. Next, the image is eroded, i.e. shrunk to a single pixel in thickness. Practically it is achieved by averaging the nonzero indices for each horizontal coordinate. These steps are depicted in Figure A.13. Given the eroded image and the spatial resolution, x and y coordinates of the deflected specimen can be calculated. Next, a polynomial $P(x)$ of order 4 is fitted to the x and y coordinates of the deflected specimen with the constraint that it must pass through the origin.

Using the polynomial, the tip deflection as function of time is found and presented for all the tested specimen in Figure A.14. Quite a lot of scatter in the data are observed but it is worth to note that six of the nine recorded deflections are within 5 mm after 13 s. No trends can be seen regarding the

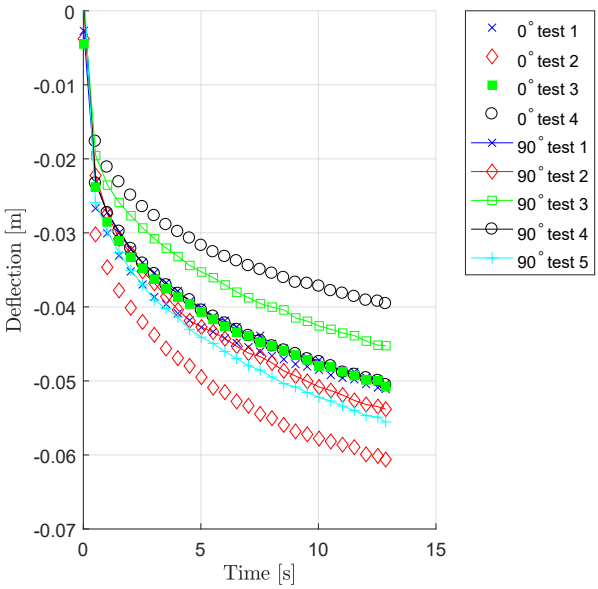

Fig. A.14: Cantilever tests of 150 mm specimen presented as tip deflection vs time.

orientation of the specimens. Especially the initial conditions, i.e. releasing of the specimen from horizontal is believed to cause the scatter. Other test methods could give better control of the test parameters (Alshahrani and Hojjati, 2017).

In the following, 0° test 3 will be considered since it represents the average behavior of the tests. The curvature of the specimen is found as follows:

$$\kappa = \frac{P''(x)}{(1 + P'(x)^2)^{\frac{3}{2}}} \tag{A.11}$$

From which it is possible to calculate the strain using the thickness T of the specimen:

$$\varepsilon_{xx} = -0.5\, T\, \kappa \tag{A.12}$$

In this formula it is assumed that the neutral axis is located in the geometric center of the beam. This is not the case when the effective moduli are different in tension and compression. Also the weave style influences the location of the neutral axis. However, since the desired quantity is the *strain rate*, it is believed that the calculation is valid. This is also justified from Figure A.15 which depicts the strain vs. time at different percentages of the beam length.

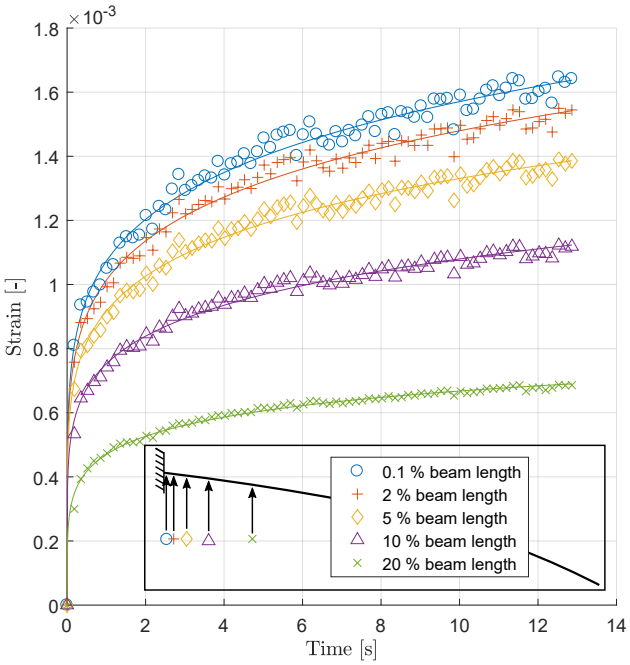

Fig. A.15: Strain vs. time at different percentages of the beam lengths for cantilever specimen.

The slopes of the curves, i.e. the strain rates, are seen to be very similar over the course of the test, especially near the root end. The solid lines arise from a least squares fit of a double power law on the following form (used for analytical differentiation):

$$\varepsilon_{xx}(t) = at^b + ct^d \tag{A.13}$$

During the tests it was observed that the specimen mostly deforms near the root end (see also Figure A.13). Therefore, the 0.1% beam length curve is used for strain rate calculation for the FE model.

The final information that is derived from the cantilever test is the out-of-plane shear modulus. From Timoshenko beam theory for a linear elastic, small deformation cantilever beam with a uniform load q (gravity) the slope at $x = 0$ is:

$$v'(x = 0) = \frac{qL}{K_s GA} \tag{A.14}$$

Here K_s is the shear correction factor which, in lack of better, assumes the familiar value of 5/6 for solid homogeneous materials. Based on the root end slope of the experiment, the value of G can be estimated. As expected,

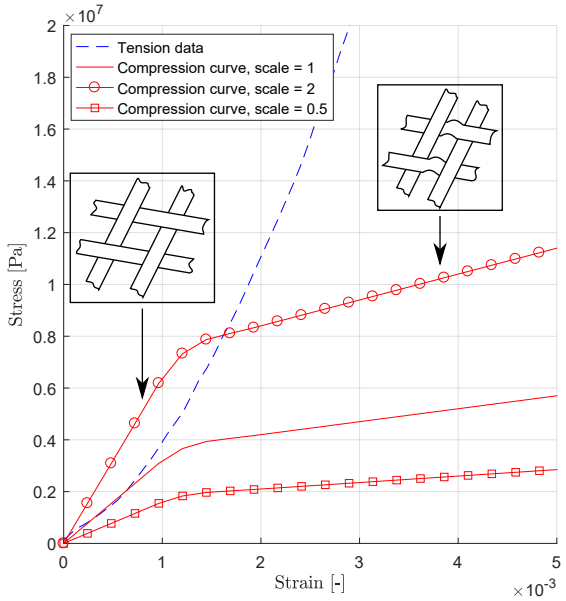

Fig. A.16: Scalable compression stress-strain curve with break caused by meso-level buckling.

it decays with time. In the current FE material model, however, it must be a constant. A value of $G_{13} = G_{23} = 2 \cdot 10^5$ Pa is chosen by manual fitting such that also a physically sensible response is obtained when the ply is subjected to compression.

With the link between the deflection and the strain rate established, the task is now to determine a compression stress-strain curve, that will give the desired deflection. One could in principle calculate the moment and then the stress in the beam from beam theory. However, the uncertainty of the neutral axis location in addition to the nonlinear tension response (Figure A.8) complicates the operation. Thus, a more robust choice is the inverse model approach.

First, a compression master curve is chosen. The idea is to define the shape of the curve and use a single parameter to scale the curve such that different bending responses are obtained. The chosen master curve resembles a buckling curve where the break of the curve is assumed to arise from meso-level buckling, i.e. buckling of the tows in the unit cell. The curve follows the initial slope of the tension response until 0.1 % strain after which the slope decreases to $5 \cdot 10^8$ Pa. Notice, however, that these slopes were chosen rather arbitrarily. The curve is depicted in Figure A.16. A total of 12 FE simulations of a deflecting cantilever beam are then conducted with the compression curve scaled in the range from 0.02 to 10. For each FE simulation the

static tip deflection is extracted. Now, interpolating using smooth splines, an expression for the tip deflection of the FE model as function of the scaling factor is obtained.

The only task remaining is to output the desired compression stress-strain curves and corresponding strain rates for the material model. The first curve is generated from data at time equal to 0.4 s in the experiment. The last curve is generated from data where the prepreg specimen has reached a static deflection of 95 mm. Here the strain rate should be effectively zero and is input as $\dot{\varepsilon} = 10^{-15}$. Four curves with equidistant scaling factor are generated in between. Note, that no extrapolation was used in the determination of the stress-strain curves.

A.5 Results

This section presents results with the Virtual Draping Environment (VDE).

A.5.1 Simulation of Cantilever Test

As a verification of the cantilever test data processing described in the previous section, two cantilever tests are simulated in Abaqus. This includes a model with the same dimensions as used for the data processing (25 mm $\times$ 150 mm) and a shorter model (25 mm $\times$ 70 mm). For the latter, two cantilever experiments are conducted for comparison. The results are presented in Fig A.17. From the figure it is evident that there is fine agreement between the test and simulation of the 150 mm strip. A small offset of maximum 2 mm or 4 % is seen. For the 70 mm strip there is also good agreement between test and simulation. With the rather large uncertainties of the experiment the bending part of the material model is considered adequate. Regarding the damping, which was described in section A.3.3, the calculated value is seen to almost critically damp the system. Some initial deflection oscillation is seen in the experimental data and is also captured by the FE simulation as seen in the zoomed-in rectangle. Notice that this is a physical dynamic effect of the test.

A.5.2 Model Validation

In the following, a simple test case with 4 grippers (120 mm spacing) and a 160 mm $\times$ 160 mm ply is considered. The ply is draped onto the lower left corner of the test mold (see Figure A.3). A test rig where the grippers are controllable in x, y and z directions is used to obtain experimental data. The grippers are mounted in ball joints but no interlinks are used. With these controllable DOF, the system is more deterministic which facilitates the validation. A manually created draping sequence that purposely produces wrin-

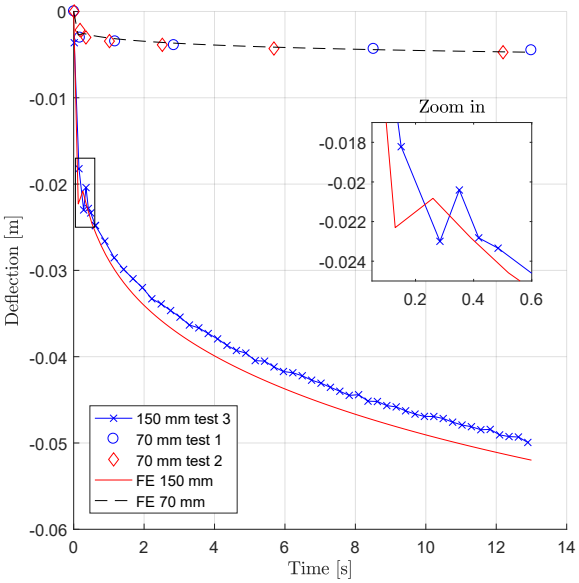

Fig. A.17: Comparison of experiments and FE simulations of cantilever test. The FE model uses data from *150 mm test 3* as input.

kles is executed and afterwards the draped ply on the mold is recorded using a PrimeSense Carmine 1.09 3D scanner. The same draping sequence is simulated using the transient model in Abaqus. The starting position of the grippers is such that they all have the same vertical distance to their target points on the mold surface. The draping sequence consists of two parts: a sequential in-plane movement of three grippers to the x and y coordinates of the target points, followed by a collective vertical movement to the mold surface. To enforce the infinite friction assumption in the model, the grippers (solid nylon discs) are glued onto the ply.

The ply after in-plane deformation and in the final configuration on the mold is depicted in Figure A.18. During the in-plane movement of the grippers a large wrinkle is formed in the direction of shearing. This is maintained in the draped configuration. Notice, that this is not due to the fabric reaching the locking angle ($\approx 35°$) since the maximum shearing angle on the mold is about $20°$ (according to the kinematic mapping algorithm). In addition, because of the mold-ply friction, the grippers are not completely tangent to the mold surface in the final configuration.

The simulation results of the transient FE model are shown in Figure A.19 in the same two states (See the appendix for the velocities used). In general, the FE model is seen to predict the tendencies in both states well. The largest

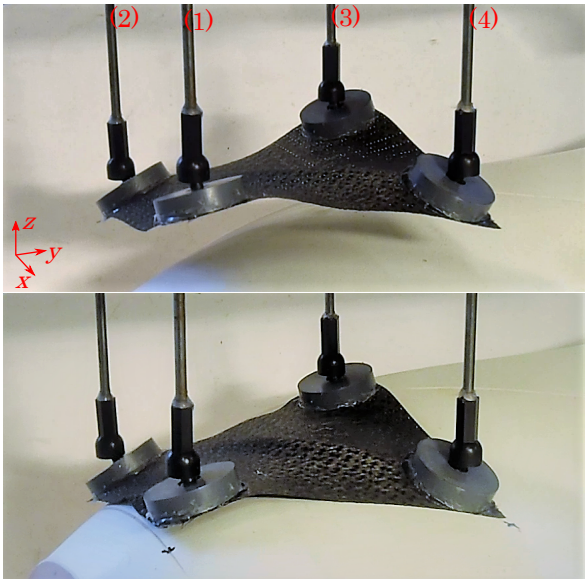

Fig. A.18: The model validation drape experiment in two different states: Top: After in-plane movement (free hanging). Bottom: Final configuration on the mold.

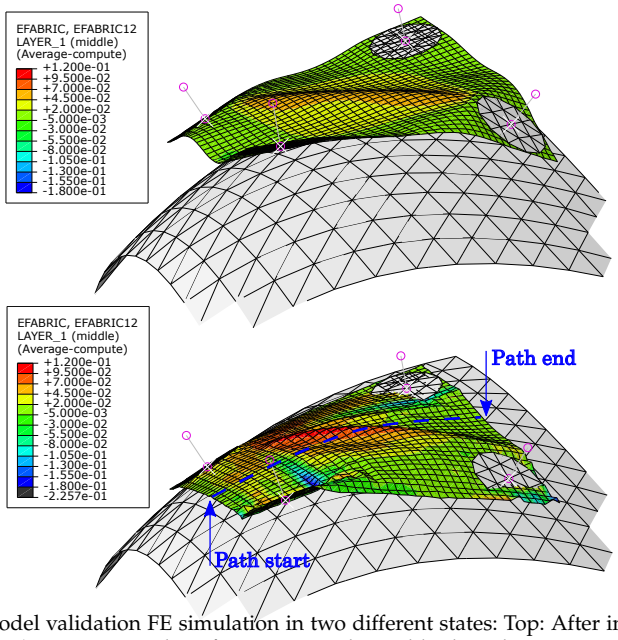

Fig. A.19: The model validation FE simulation in two different states: Top: After in-plane movement (free hanging). Bottom: Final configuration on the mold. The colors represent fabric shear strain.

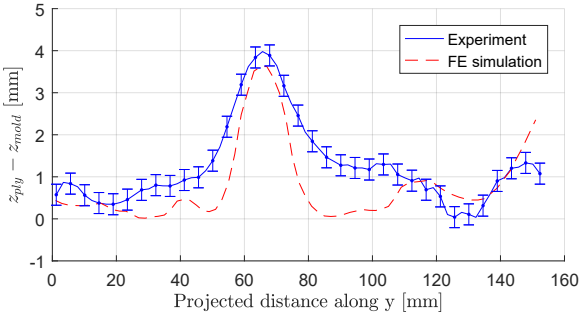

Fig. A.20: Difference between ply and mold for both experimental (error bars indicate resolution) and FE simulation.

discrepancies are seen in the draped configuration near the grippers where also some small penetrations through the mold surface occur. This indicates that the constant Coulomb friction model is a simplification of the actual interface behavior. This may be due to the viscous properties of the prepreg.

Figure A.20 presents a plot of the difference between the ply and the mold for both the experiment and the FE model. The data are sampled at a line of constant x-values halfway across the ply. The spatial resolution of the 3D scanner used to record the experimental result is about 0.5 mm which is indicated with error bars in the plot.

The main peak in the plot corresponds to the large diagonal wrinkle, which is predicted well by the FE model. This is mostly related to the material model as the wrinkle is formed before mold contact as seen in Figure A.19. There is a discrepancy of about 1 mm on the right side of the peak at y-distances 80 mm to 110 mm which again is believed to be due to the friction model. At y-distances 110 mm to 160 mm a fair agreement is seen. This wrinkling is partly created before mold contact. Obviously there are a some uncertainties associated with both the FE model and the experiment, so a result of this kind is considered acceptable.

Overall, the comparisons between the FE models and experiments in this and in the previous section indicate that the material model is appropriate while the ply-mold interface model with the simple constant Coulomb friction could be improved. However, the discrepancies in the present example are mostly caused by the grippers when they make contact with the mold at an angle, i.e. they are not tangent to the mold surface. As seen, the friction causes the grippers to halt in these configurations which of course should be avoided already in the planning of the draping sequence. However, as will become evident in the following, the use of interlinks greatly reduces the issue with gripper rotations.

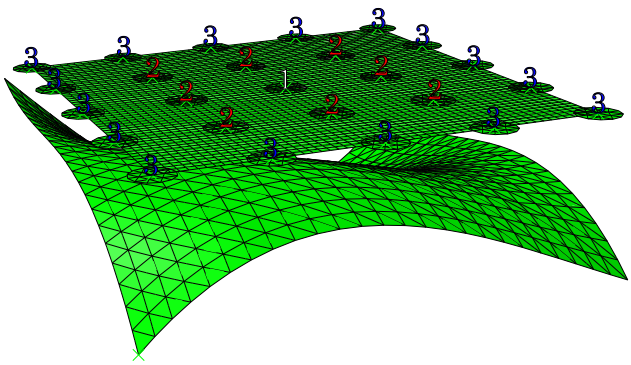

Fig. A.21: The FE model in the initial configuration. The numbers indicate the groups of grippers in the wave shape draping sequence.

A.5.3 Simulation of Robot System Draping

Consider next a 405 mm $\times$ 405 mm ply being draped onto the test mold by the robot system. The interlinks are used in the model and therefore only the z DOF are controllable. The 5 $\times$ 5 grid has a spacing of 100 mm. A vertical spring is introduced in the connector elements (see Figure A.7) to model the maximum actuator force. This helps prevent mold penetrations since the grippers are displacement controlled. If some grippers are not completely on the mold surface after draping, they will be moved accordingly.

The energy mapping algorithm is used to find the draped configuration. A starting point in the center of the mold is selected and geodesic lines from mid-side to mid-side of the mold edges are created on the mold surface. Since the starting point is in the center of the mold, gripper 3,3, i.e. the one in the center, is fixed in-plane. The initial configuration in the FE model is shown in Figure A.21. During draping, the grippers are first moved into the preshape (5 s duration) which is seen in Figure A.22. Next, the two different strategies previously outlined in section A.3.2 are executed: The uniform draping sequence and the wave shape draping sequence. Results from both are presented in the following. It is expected that the wave shape draping sequence performs better than the uniform draping sequence because it resembles the current manual operation closer.

A.5.4 Result with Uniform Draping Sequence

As described previously, the uniform draping sequence implicates that all the grippers move towards the mold simultaneously (5 s duration). The result is shown in Fig A.23 as a contour plot of the ply-mold difference. The figure shows, that the draped configuration has wrinkles. Especially, the upper left corner has a maximum ply-mold separation of 12.2 mm. The figure

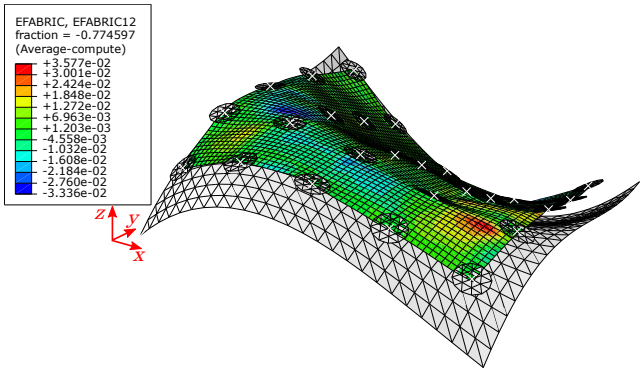

Fig. A.22: The robot system FE model after preshaping. The colors represent shear strain.

also shows the prescribed boundary (red line with circles), i.e. the boundary obtained from the mapping algorithm. Here, it is evident that the upper and lower edges of the ply are far off the boundary - as much as 28 mm in the upper right corner. So while the grippers in principle should make contact with the mold simultaneously using this draping sequence, the steep gradients of the mold in areas with high curvature causes some grippers to make contact with the mold before others. Thereby, some grippers do not reach their target points. From Figure A.22 it is seen that the sag of the ply before mold contact is small but even the free-hanging ply can make contact with the mold at the wrong x and y coordinates. Since the in-plane displacements are controlled by the interlinks the error propagates throughout the ply.

A.5.5 Result with Wave Shape Draping Sequence

Next, a wave shape is simulated originating from the center of the mold. The numbers in Figure A.21 indicate the order in which the grippers move. Grippers with the same number move to the mold simultaneously in 3.5 seconds. After a delay of 0.8 seconds the next group follows. The last grippers to make contact with the mold are consequently the group 3 grippers. The result is shown in Figure A.24. From the figure it is evident that there are still wrinkles in the draped configuration, however, the result is improved compared to the uniform draping sequence. The wrinkles are located in the same areas of the mold but now the maximum ply-mold difference is reduced to 10.1 mm (12.2 mm previously) and the boundary offset of the upper right corner is reduced to about 20 mm (28 mm previously). The middle part of the ply from where the wave originates as well as the lower left corner is now completely free from wrinkles. Thus, the wave shape draping sequence is an improvement but the issues in the areas of high mold curvature as described in the previous section persist. A 3D view of the draped configuration is

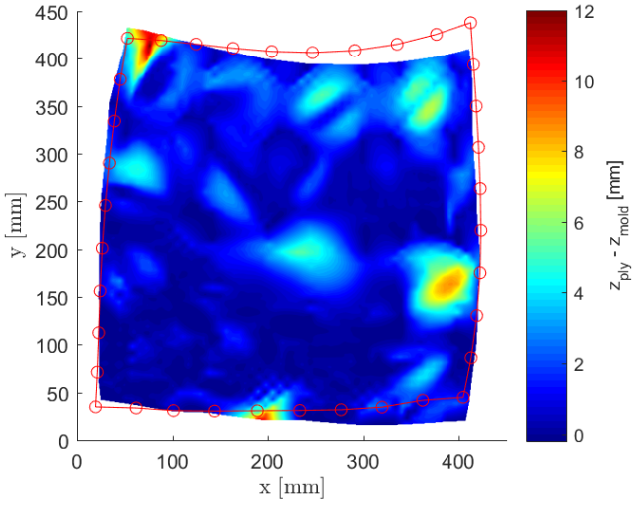

Fig. A.23: Contour plot of ply-mold difference for uniform draping sequence. The red line with circles indicates the prescribed boundary.

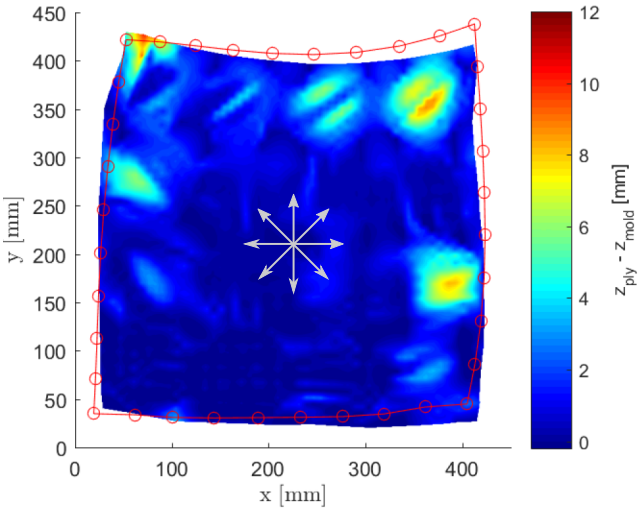

Fig. A.24: Contour plot of ply-mold difference for wave shape draping sequence. The red line with circles indicates the prescribed boundary. The arrows show the wave direction.

presented in Figure A.25.

Please note, that both of the results presented in Figures A.23 and A.24 are inconsistent with the requirements of no wrinkles and placement within the boundary and thus cannot be accepted in an industrial context.

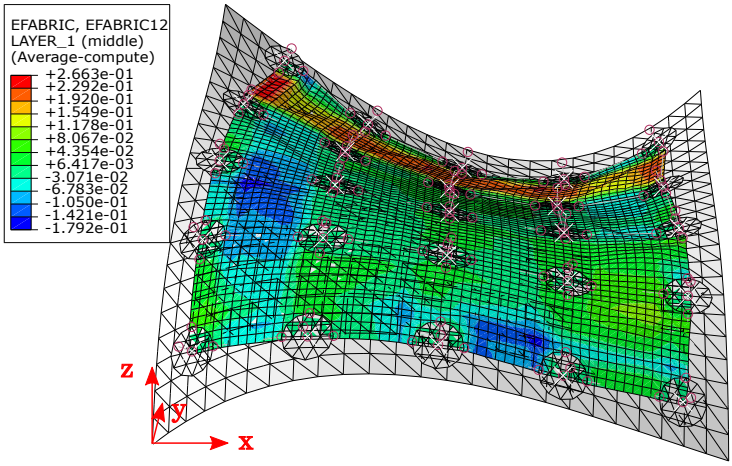

Fig. A.25: The draped configuration of the wave shape draping sequence. The colors indicate fabric shear strain.

A.6 Conclusions

This paper has introduced a Virtual Draping Environment (VDE) for planing and simulating draping sequences for the robot system under development. The z-velocity of each gripper in the array must be determined such that the draped configuration is free from wrinkles. Here, the emphasis has been on setting up the transient non-linear Finite Element (FE) model and using it for simulation of the draping process. To this end, material characterization was employed which consists of tension tests, bias-extension tests, and cantilever tests. Especially the shear and bending response showed a high degree of rate-dependency. This was expected since the ply is a prepreg.

The bending response of the FE model is achieved by adjusting the compressive stiffness in the fiber direction. By means of video recording of the cantilever test and image processing, the experimental deflection was determined. Additionally, the strain rate was calculated in order to include the rate-dependency in the FE model. Using an inverse modeling approach, the bending response of the FE model was adjusted to match that of a cantilever test. This approach showed good agreement - also when comparing to a cantilever test of a shorter specimen.

To test the FE model in its entirety, a simple 4-gripper experimental arrangement was used. When comparing the subsequent FE simulation with the experiment, the material model seemed to be appropriate while the simple Coulomb friction interface could be improved. It was, however, noted that the lack of interlinks (see Figure A.2) in the validation setup caused some particular difficult interface conditions which are avoided when simulating the

robot drape tool.

Finally, the FE model was used to evaluate two different gripper move patterns or *draping strategies*. The first was a uniform strategy where all grippers move towards the mold simultaneously. The second is a wave shape strategy where grippers move in a droplet or wave originating from the center of the mold. Both of the simulated draping sequences resulted in wrinkles but the wave shape strategy performed slightly better.

To this end it is interesting to note that both simulations used the same z-displacements of the grippers but executed in different ways. The grippers do not terminate at the same locations in the two simulations so it cannot directly be concluded that it is a path dependent problem. However, the fact that the differences result from mold-ply friction which itself is a path dependent phenomenon and that wrinkles can be formed already in the free hanging configuration (see Figure A.18) is strong evidence.

The work presented in this paper is only a small step towards modeling of automated manipulation of prepregs. The griper-ply interface which was neglected in this study, should be investigated carefully. Although the frictional resistance appears high, it should be checked that it is sufficient when the ply is sheared. The current tie contact probably also overconstrains the ply which could lead to unphysical wrinkling. Feasible draping sequences where the ply border matches the prescribed boundary should be generated. To this end it could be interesting to investigate whether optimization techniques can be employed. Wrinkles should also be avoided but another approach would be to investigate what wrinkle sizes and shapes that can be removed during debulking of the layup.

By continuing the study of robotic draping it is hoped that the cost of carbon fiber parts for the aerospace industry eventually can be lowered.

Conflicts of Interest

The Authors declare that there is no conflict of interest.

Funding

The research presented in this paper is carried out as part of the project Flex-Draper - An Intelligent Robot-Vision System for Draping Fiber Plies sponsored by the Innovation Fund Denmark, Grant no. 5163-00003B. This support is gratefully acknowledged.

References

Aimene Y, Vidal-Salle E, Hagege B, Sidoroff F, Boisse P (2010) A Hyperelastic Approach for Composite Reinforcement Large Deformation Analysis. Journal of Composite Materials 44(1):5–26, DOI 10.1177/0021998309345348

Alshahrani H, Hojjati M (2017) A new test method for the characterization of the bending behavior of textile prepregs. Composites Part A: Applied Science and Manufacturing 97:128–140, DOI 10.1016/j.compositesa.2017.02.027

Bergsma OK, Huisman J (1988) Deep drawing of fabric reinforced thermoplastics. In: Brebbia CA, de Wilde WP, Blain WR (eds) Computer aided design in composite material technology, Springer-Verlag, Berlin, pp 323–334

Boisse P, Hamila N, Vidal-Salle E, Dumont F (2011) Simulation of wrinkling during textile composite reinforcement forming. Influence of tensile, in-plane shear and bending stiffnesses. Composites Science and Technology 71(5):683–692, DOI 10.1016/j.compscitech.2011.01.011

Boisse P, Hamila N, Guzman-Maldonado E, Madeo A, Hivet G, Dell'Isola F (2017) The bias-extension test for the analysis of in-plane shear properties of textile composite reinforcements and prepregs: a review. International Journal of Material Forming 10(4):473–492, DOI 10.1007/s12289-016-1294-7

Cao J, Akkerman R, Boisse P, Chen J, Cheng HS, de Graaf EF, Gorczyca JL, Harrison P, Hivet G, Launay J, Lee W, Liu L, Lomov SV, Long A, de Luycker E, Morestin F, Padvoiskis J, Peng X, Sherwood JA, Stoilova T, Tao X, Verpoest I, Willems A, Wiggers J, Yu T, Zhu B (2008) Characterization of mechanical behavior of woven fabrics: Experimental methods and benchmark results. Composites Part A: Applied Science and Manufacturing 39(6):1037–1053, DOI 10.1016/j.compositesa.2008.02.016

Cherouat A, Billoët JL (2001) Mechanical and numerical modelling of composite manufacturing processes deep-drawing and laying-up of thin pre-impregnated woven fabrics. Journal of Materials Processing Technology 118(1-3):460–471, DOI 10.1016/S0924-0136(01)00987-6

Cook R, Malkus DS, Plesha ME (2002) Concepts and applications of finite element analysis. John Wiley & Sons, Inc., New York

Dangora LM, Mitchell CJ, Sherwood JA (2015) Predictive model for the detection of out-of-plane defects formed during textile-composite manufacture. Composites Part A: Applied Science and Manufacturing 78:102–112, DOI 10.1016/j.compositesa.2015.07.011

Dassault Systèmes Simulia Corporation (2014) Abaqus 6.14 Documentation: 23.4.1 Fabric material behavior

Döbrich O, Gereke T, Diestel O, Krzywinski S, Cherif C (2014) Decoupling the bending behavior and the membrane properties of finite shell elements for a correct description of the mechanical behavior of textiles with

a laminate formulation. Journal of Industrial Textiles 44(1):70–84, DOI 10.1177/1528083713477442

Grosberg P, Park BJ (1966) The Mechanical Properties of Woven Fabrics: Part V: The Initial Modulus and the Frictional Restraint in shearing of Plain Weave Fabrics. Textile Research Journal 36(5):420–431, DOI 10.1177/004051756603600505

Hamila N, Boisse P, Chatel S (2009) Semi-discrete shell finite elements for textile composite forming simulation. International Journal of Material Forming 2(SUPPL. 1):169–172, DOI 10.1007/s12289-009-0518-5

Hancock SG, Potter KD (2006) The use of kinematic drape modelling to inform the hand lay-up of complex composite components using woven reinforcements. Composites Part A: Applied Science and Manufacturing 37(3):413–422, DOI 10.1016/j.compositesa.2005.05.044

Harrison P (2016) Modelling the forming mechanics of engineering fabrics using a mutually constrained pantographic beam and membrane mesh. Composites Part A: Applied Science and Manufacturing 81:145–157, DOI 10.1016/j.compositesa.2015.11.005

Harrison P, Clifford M, Long A (2004) Shear characterisation of viscous woven textile composites: A comparison between picture frame and bias extension experiments. Composites Science and Technology 64(10-11):1453–1465, DOI 10.1016/j.compscitech.2003.10.015

Harrison P, Tan MK, Long AC (2005) Kinematics of Intra-Ply Slip in Textile Composites during Bias Extension Tests. In: 8th Int. ESAFORM Conf. on Materials Forming, pp 987–990

Jauffrès D, Sherwood JA, Morris CD, Chen J (2010) Discrete mesoscopic modeling for the simulation of woven-fabric reinforcement forming. International Journal of Material Forming 3(SUPPL. 2):1205–1216, DOI 10.1007/s12289-009-0646-y

Laroche D, Vu-Khanh T (1994) Forming of Woven Fabric Composites. Journal of Composite Materials 28(18):1825–1839

Lebrun G, Bureau MN, Denault J (2003) Evaluation of bias-extension and picture-frame test methods for the measurement of intraply shear properties of PP/glass commingled fabrics. Composite Structures 61(4):341–352, DOI 10.1016/S0263-8223(03)00057-6

Liang B, Chaudet P, Boisse P (2017) Curvature determination in the bending test of continuous fibre reinforcements. Strain 53(1):e12213, DOI 10.1111/str.12213

Lin H, Clifford M, Taylor P, Long A (2009) 3D mathematical modelling for robotic pick up of textile composites. Composites Part B: Engineering 40(8):705–713, DOI 10.1016/j.compositesb.2009.07.006

Lukaszewicz D, Ward C, Potter KD (2012) The engineering aspects of automated prepreg layup: History, present and future. Composites Part B: Engineering 43(3):997–1009, DOI 10.1016/j.compositesb.2011.12.003

Mack C, Taylor HM (1956) The Fitting of Woven Cloth to Surfaces. Journal of the Textile Institute Transactions 47(9):T477–T488, DOI 10.1080/19447027.1956.10750433

Nguyen M, Herszberg I, Paton R (1999) The shear properties of woven carbon fabric. Composite Structures 47(1-4):767–779, DOI 10.1016/S0263-8223(00)00051-9

Peng X, Guo Z, Du T, Yu W (2013) A simple anisotropic hyperelastic constitutive model for textile fabrics with application to forming simulation. Composites Part B: Engineering 52:275–281, DOI 10.1016/j.compositesb.2013.04.014

Skordos AA, Monroy Aceves C, Sutcliffe MPF (2007) A simplified rate dependent model of forming and wrinkling of pre-impregnated woven composites. Composites Part A: Applied Science and Manufacturing 38(5):1318–1330, DOI 10.1016/j.compositesa.2006.11.005

Van Der Weeën F (1991) Algorithms for draping fabrics on doubly-curved surfaces. International Journal for Numerical Methods in Engineering 31(7):1415–1426, DOI 10.1002/nme.1620310712

Willems A, Lomov SV, Verpoest I, Vandepitte D (2009) Drape-ability characterization of textile composite reinforcements using digital image correlation. Optics and Lasers in Engineering 47(3-4):343–351, DOI 10.1016/j.optlaseng.2008.03.012

Womersley JR (1937) 6.—THE APPLICATION OF DIFFERENTIAL GEOMETRY TO THE STUDY OF THE DEFORMATION OF CLOTH UNDER STRESS. Journal of the Textile Institute Transactions 28(3):T97–T113, DOI 10.1080/19447023708658810

Yu W, Pourboghrat F, Chung K, Zampaloni M, Kang T (2002) Non-orthogonal constitutive equation for woven fabric reinforced thermoplastic composites. Composites Part A: Applied Science and Manufacturing 33(8):1095–1105, DOI 10.1016/S1359-835X(02)00053-2

Yu W, Zampaloni M, Pourboghrat F, Chung K, Kang T (2005) Analysis of flexible bending behavior of woven preform using non-orthogonal constitutive equation. Composites Part A: Applied Science and Manufacturing 36(6):839–850, DOI 10.1016/j.compositesa.2004.10.026

Zhu B, Yu T, Teng J, Tao X (2008) Theoretical Modeling of Large Shear Deformation and Wrinkling of Plain Woven Composite. Journal of Composite Materials 43(2):125–138, DOI 10.1177/0021998308098237

Appendix: 4-Gripper FE Prescribed Velocities

Table A.1 presents the 4-gripper FE model velocity boundary conditions, which were obtained from the grippers in the experiment. The initial coordinate of gripper 2 is $\{39.8, 40.1, 137.0\}$ mm with the other grippers placed such that they form a square grid with side lengths 120 mm.

Table A.1: Velocities prescribed in the 4-gripper FE model. Non-active grippers are prescribed a zero velocity.

Step	Grp.	Velocity [mm/s]			Time [s]
1	1	{ 0.0,	0.0,	−0.93 }	3
1	2	{ 0.0,	0.0,	−9.53 }	3
1	4	{ 0.0,	0.0,	−4.27 }	3
2	1	{ -2.9,	4.0,	0.0 }	2
3	3	{ 4.1,	-0.22,	0.0 }	2
4	4	{ 0.67,	0.74,	0.0 }	18
5	1,2,3,4	{ 0.0,	0.0,	−5.1 }	6
6	1	{ -1.0,	-3.0,	0.0 }	1
6	2	{ -0.75,	-0.75,	0.0 }	1
6	3	{ -1.0,	1.0,	0.0 }	1
6	4	{ -2.0,	-3.0,	0.0 }	1

Paper B

Picture-Frame Testing of Woven Prepreg Fabric: An Investigation of Sample Geometry and Shear Angle Acquisition

Christian Krogh, Kari D. White, Alessandro Sabato & James A. Sherwood

The paper has been accepted for publication in the *International Journal of Material Forming*, 2019.

The layout has been revised.

Abstract

This paper examines different concepts in relation to the picture-frame test for shear characterization of a woven prepreg fabric. The influence of the sample arms is investigated by means of cut slits as well as removed transverse tows. Shear angles are obtained using Digital Image Correlation (DIC) and also from images taken during the test which are processed for fiber angles directly from the weave texture. The image processing relies on the Hough transform in MATLAB. The concept of constant shear strain rate is discussed and implemented in the test software by a multi-linear crosshead velocity profile. Finally, bias-extension data are obtained and used for comparison. It is found that the sample arm modifications have a pronounced effect on the measured shear load whereas the uniformness of the shear strain field in the samples is not improved considerably.

Keywords Woven carbon fiber prepreg, Shear characterization, Picture frame testing, Image Analysis

B.1 Introduction

During the forming of woven fabrics, a significant amount of shear or trellising occurs. This deformation mechanism has long been recognized as the most important when an initially flat piece of fabric undergoes deformation to a double-curved shape (Nguyen et al., 1999). Naturally, the shear properties of the fabric must be characterized if the forming behavior is to be accurately predicted in a simulation code. To this end it is common practice to use either the *picture-frame test* or the *bias-extension test* to do this characterization.

The picture-frame test uses a square frame with hinged corners. A test sample is clamped in the frame with the fibers oriented parallel and perpendicular to the frame edges. One frame corner is held stationary while the opposite corner is displaced such that the sample theoretically is subjected to uniform shear. The test has been applied to a number of different materials such as thermoplastic woven glass fibers (Peng and Cao, 2005), dry woven carbon fibers (Nguyen et al., 1999), woven carbon fiber prepreg (Mohan et al., 2016), Uni-Directional (UD) carbon fiber prepreg (Harrison et al., 2002), and thermoplastic cross-ply polyethylene fiber sheets (Dangora et al., 2015).

There are a number of known issues in regard to the picture-frame test. First, the test is sensitive to the clamping boundary conditions as discussed by Harrison et al. (2004). If fiber tension across the sample is too low, the sample might not shear to the same extent as the frame. On the other hand, if the tension is too high, then the results might be compromised - especially

if the sample is misaligned in the frame. Second, because of the frame design with the clamping area and the hinges, the samples are in general not square but cruciform. Therefore, the "arms" of the sample could also influence the measurements in the gage area in the center of the sample.

To avoid the contributions from the sample arms when testing woven materials, some researchers remove the transverse tows from the arms before testing, see e.g. Lussier (2000), Zhu et al. (2007), and Peng and Cao (2005). However, based on a benchmark study with contributions from several research groups (Cao et al., 2008) there exist no general practice regarding the sample arms. The results from the paper do in fact not suggest differences between samples with and without transverse tows in the sample arms. However, due to the many variations in test setups and practices among the participating research groups, this conclusion is not decisive. In the paper, it was discussed how one should be careful not to alter the sample tightness or local fiber orientations when removing the transverse tows.

For some materials, the transverse fibers are not so easily removed. Dangora et al. (2015) studied the effect of sample arms in the picture-frame test with thermoplastic preconsolidated UD cross-ply. Slits were cut in varying widths and also the polyurethane matrix was dissolved to achieve a condition of "infinite slits". A significant influence of the sample arms was found and only the infinite-slit condition test data provided good agreement in a finite element (FE) simulation.

In the picture-frame test, it is often assumed that the shear strains are uniform in the gage area such that a global shear force and shear strain can be obtained from a kinematic and static analysis of the frame. It is, however, common practice to use either Digital Image Correlation (DIC) measurements or to manually check the fiber angles from pictures of the test as a validation (Cao et al., 2008).

The manual identification of fiber angles from pictures can be alleviated by using image processing techniques. Harrison et al. (2008) presented a program that uses lines drawn on the samples before testing to identify the shear angles. However, the authors noted that the finite thickness and the varying contrast of the lines would introduce noise into the measurements. Arumugam et al. (2016) conducted picture-frame tests of 3D textiles with a grid drawn on the test samples. Pictures taken during the test were analyzed using a Hough transform to recognize straight lines. Other researchers have obtained fiber angles directly from the weave texture. See for instance the study by Olson et al. (2017) on parachute suspension lines. Lastly, it should be noted that advanced commercial laser measurement systems exist, which was e.g. applied by Krieger et al. (2015) for the bias-extension test of NCF.

A final point regarding the picture frame is, that it does not produce a constant shear angle rate when displaced at a constant crosshead rate. Rather, the shear angle rate is a nonlinear function of the crosshead movement. This

statement is evident from the aforementioned kinematic relations between the crosshead displacement and the shear angle. The behavior must be taken into account when testing rate-dependent materials such as prepregs and e.g. comparing the test data to bias-extension data.

A number of remedies to the non-constant shear angle rate have been discussed in the literature. Harrison et al. (2002) used the picture-frame kinematics to generate a nonlinear crosshead vs. time expression that yields a constant shear rate. It was implemented on a standard universal test machine. However, additional control software was needed to achieve the nonlinear crosshead movement. It was reported that the use of a constant shear rate resulted in less variability in the data. In the study by Lebrun et al. (2003), picture-frame and bias-extension data were compared. The shear angle rate was taken into account by using a calculated ratio between the two crosshead speeds which ensured an equal (but varying) shear angle rate. Harrison et al. (2004) developed normalization equations for the picture-frame test and the bias-extension test that allows for comparison. By normalizing the two types of test data by their respective crosshead rates, good agreement was found in the comparison.

The overall goal of this paper is to investigate the shear characterization of a woven prepreg fabric using the picture-frame test. This investigation involves the influence of the cruciform sample arms on the gage area and how fabric shear angles can be acquired. Regarding the sample arms, the transverse tows are not easily removed due to the resin, and an approach similar to that of Dangora et al. (2015) will be taken, which involves cut slits and dissolved resin. The details hereof are presented in Section 2. The influence of the sample arms is inspected by considering the load required to shear the sample as well as the distribution of shear angles in the sample. Regarding the latter, the kinematic analysis does not suffice, for which reason a full-field method is needed. Here, the well-proven DIC is employed and it is also investigated if the fabric angles can be acquired based on the weave texture from images taken during the test. More specifically, the Hough transform is applied in this analysis. The data acquisition methods are presented in Section 3. The rate-dependency of the prepreg fabric is taken into account by testing at a constant shear rate. A nonlinear expression for the crosshead is generated and approximated using linear segments. The segments are readily implemented as ramps in the standard Instron® Bluehill software. The procedure is elaborated in Section 4. The results of the paper are presented in Section 5. It is shown that the sample arm modification mainly influences the measured shear load. To address potential issues with the clamping boundary conditions, the picture-frame data are compared to results from a bias-extension test. While this test has a number of drawbacks, the tows are always untensioned, and thus the test can be used to verify picture-frame data as suggested by Harrison et al. (2004). Good agreement between the two tests is found pro-

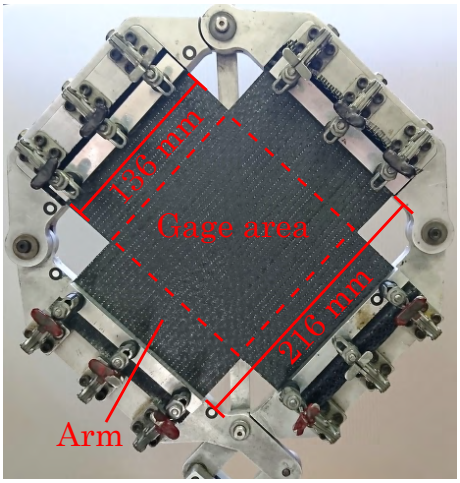

Fig. B.1: The picture frame with a mounted sample. The frame has an amplifying linkage mechanism.

vided that the proper sample area-normalization is carried out. The paper is ended with a discussion in Section 6 and a conclusion.

B.2 Test Samples

The material used in this study is a 4-harness satin-weave carbon-fiber prepreg with a bismaleimide (BMI) resin. The thickness is 0.3 mm and the areal density is 314 g/m^2. The resin causes the material to exhibit viscoelasticity. As a consequence, the shear force required to shear the material depends on the rate of shear. This rate-dependency was verified in a previous study with the prepreg material using the bias-extension test (Krogh et al., 2019). The viscoelasticity makes the shear response different from that of dry fabrics. The testing temperature is also a factor because the viscosity of the resin is dependent on temperature. In this study, all tests were carried out at room temperature.

Figure B.1 shows the picture frame including the amplifying linkage mechanism with a mounted sample. The amplifying linkage mechanism respectively increases the displacement and decreases the force on the frame by a factor of 4.25 in comparison to the crosshead values. The basic sample type is a cruciform with an arm width equal to 62 tows or approximately 136 mm, i.e. the maximum width that fits in the frame. The test sample is cut from the stock material by means of a utility knife and a ruler. The basic sample type serves as the reference and will be referred to as having *full arm geometry*. To investigate the influence of arm geometry, the basic sample is modified in

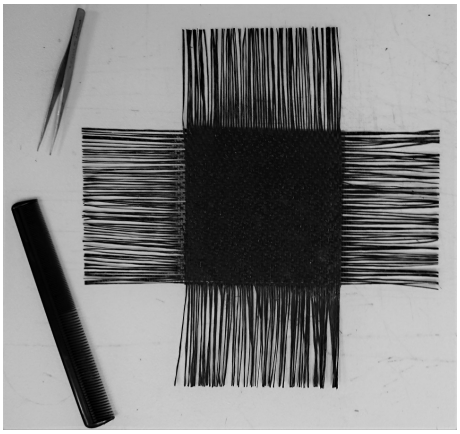

Fig. B.2: Transverse tows removed from sample with comb and tweezers after submersion in ethanol.

two ways: By *cutting slits* and by *removing the transverse tows*.

The cutting of slits is likewise carried out with the utility knife and the ruler. The slits are cut with a distance increment of 3 tows, and thus, the total number of slits in each arm is 20.

To remove the transverse tows, the resin must be dissolved. For this purpose ethanol was selected because it dissolves the uncured BMI resin without damaging the carbon fibers according to chemical resistance charts. Each sample arm was submerged in a tray with ethanol for a few seconds after which excess ethanol was wiped off. Care was exercised not to get any ethanol on the gage area of the sample. Next, the sample was placed on a cutting board, and a ruler was placed on top on the boundary between the gage area and the arm. A comb was used to remove the transverse tows. Only a few tows were removed at a time, starting from the free edge. Near the gage area, tweezers were used to remove the final transverse tows. The end result is depicted in Fig. B.2.

Using the approach outlined above, it was found, that the remaining tows would still be coated with resin. For the sake of easier mounting in the frame, it was decided not to remove that resin and thereby keep the fibers bundled. Also, in relation to the mounting of the sample in the frame, it was found preferable to comb the samples while on the cutting board and wrap the arm ends in masking tape before transferring the sample to the frame.

Both the cutting of slits and removing of transverse tows are cumbersome tasks that take about 10 - 15 minutes per sample. This time must be added to the cutting of the basic cruciform sample. If DIC is used, (see Section B.3.2) then even more time must be added for sample preparation.

A wooden fixture was made to keep the frame stable while mounting the

sample. The fixture has a surface to support the sample which is flush with the frame. In this way, the effect of varying fiber tensions was diminished.

B.3 Data Acquisition and Processing

In this section, the different methods of data acquisition that were employed in the study are presented and discussed, i.e. data from the crosshead, DIC and image processing using Hough transform.

B.3.1 Crosshead Force and Displacement

Crosshead force and displacement were recorded in the picture-frame tests with the Instron Bluehill Universal Testing software. The load cell used had a capacity of 5 kN and an accuracy of 0.1 %. The formulas used to calculate the shear strain and shear force are typical for picture-frame analyses (Harrison et al., 2004; Cao et al., 2008; Launay et al., 2008; Jauffrès et al., 2010). The global shear angle, γ, of the sample is geometrically related to the length of the frame, L_F, and the crosshead displacement, δ through the equation:

$$\gamma = \frac{\pi}{2} - 2\arccos\left(\frac{1}{\sqrt{2}} + \frac{\delta}{2L_F}\right) \tag{B.1}$$

The shear force, F_{sh}, on the fabric is also a function of the global shear angle and the crosshead force, F:

$$F_{sh} = \frac{F}{2\cos\left(\frac{\pi}{4} - \frac{\gamma}{2}\right)} \tag{B.2}$$

Peng et al. (2004) used a method of normalization for cruciform sample testing based on energy conservation through work done per volume. Using an assumption of zero contribution of load from the arms and uniform shear deformation in the gage area, the shear force can be normalized over the gage area with side length L_f, while also taking the frame length into account. Combining these into a single expression yields (Jauffrès et al., 2010):

$$F_{sh,norm\_gage} = \frac{L_F}{L_f^2}\frac{F}{2\cos\left(\frac{\pi}{4} - \frac{\gamma}{2}\right)} \tag{B.3}$$

B.3.2 Digital Image Correlation

For digital image correlation, a sequence of digital images is compared to an initial reference image. A displacement field can be calculated from the local deformation of the isotropic pattern within a subset window or facet. Differentiation of the displacement field will yield the local strain of the sample. A

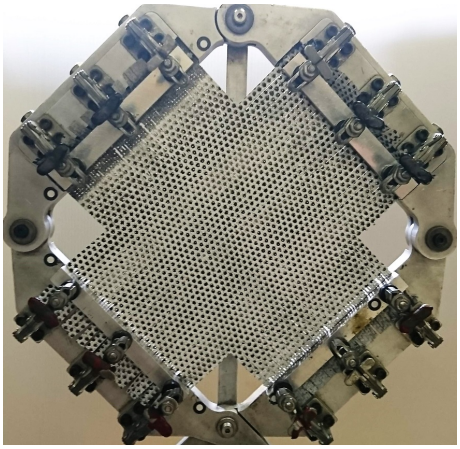

Fig. B.3: Slitted arm sample with DIC pattern mounted in the frame.

strain window is used by the differentiation algorithm, defining the number of neighboring facets. A large strain field will yield less noise, but also less spacial resolution. Two cameras, installed at different angles with respect to the sample, are required for 3D DIC. Strains are calculated in the tangential plane of the object (Lomov et al., 2008).

Digital image correlation was performed with an Aramis 3D digital imaging setup. The specifications of the setup are found in Table B.1. The analysis was performed with a facet size of 10×10, an 8-pixel step and linear shape function. The strain window was set to 3 points with the strain resolution being $0.05°$. The samples were patterned by first applying a thin coat of white spray paint to reduce glare. A uniform dot pattern was then applied using lightly sprayed black paint with a stencil. The holes of the stencil were approximately 3 mm in diameter, spaced 5 mm center-to-center on the diagonal. The use of the stencil helped to achieve an even ratio of white and black paint as well as the right speckle size. Notice, that the size and spacing of the holes in the stencil are not a direct measure of the spatial resolution because the pattern is still considered random. The patterning of the sample mounted in the frame is shown in Fig. B.3.

The previous discussion of DIC has illustrated, that the method relies on an applied pattern which enables the correlation between the deformed and the undeformed samples. The first question is whether the paint affects the measurements. This point is up for debate as some authors have reported that the paint applied for DIC does affect the results (Harrison et al., 2018) while others have reported that there is no influence (Jauffrès et al., 2010). In a comparison between different samples, it can be assumed that the paint affects all the samples equally (Dangora et al., 2015). Next, because the ref-

Table B.1: DIC setup in Aramis. The shear strain resolution is computed as the standard deviation of two still image strain maps.

Technique used	3D DIC
Sensor and Digitization	1624×1236, 8 bit
Lens and Imaging Distance	8.5 mm, 0.6 m
Recording frequency	10 Hz
Facet, step	10×10, 8
Shape functions	Linear
Interpolation of 3D points	Max. 3 points
Filtering	Median 5×5, 3 runs
Strain window	3 points
Shear strain resolution	0.05°

erence configuration is recorded after the sample has been mounted in the frame, it does not contain information about any possible unintended predeformation. That is, the fiber directions could be different from $\pm 45^\circ$ before the test is started. Lastly, the selection and application of a proper pattern can be a time consuming task. These issues are the motivation for looking into alternatives.

B.3.3 Image Processing using Hough Transform

The idea of the image processing setup is to identify the fiber angles directly from the weave texture which alleviates the issues discussed above. The tows will appear as straight lines in the images which can be detected using the Hough transform algorithm. The method is useful for finding lines in images, even if the input image contains sparse or broken lines (Marques, 2011). Figure B.4 depicts the principle of the algorithm in Cartesian coordinates. The figure shows two coordinate systems, namely the *Cartesian space* and the *Transform domain*. In the Cartesian space, two points, (x_1, y_1) and (x_2, y_2), are located, which represent two points in a recorded image. The Transform domain represent possible lines in the image, i.e. on the form $y = ax + b$. Many lines passing through the point (x_1, y_1) can be generated and vice versa for the the point (x_2, y_2). Each of those lines map to a point in the transform domain. However, only one line passes through both points and that line is exactly given by the intersection point in the transform domain.

In practice, the algorithm operates in polar coordinates with the parameters ρ (perpendicular distance from the line to the origin) and θ (the angle between the line's perpendicular and the horizontal axis) to avoid infinite gradients of vertical lines.

The implementation of the fiber angle detection in MATLAB is now ex-

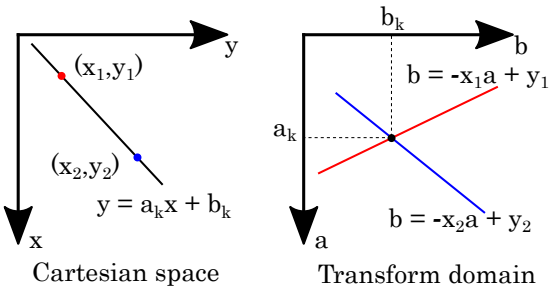

Fig. B.4: The principle of the Hough transform in Cartesian coordinates with two points.

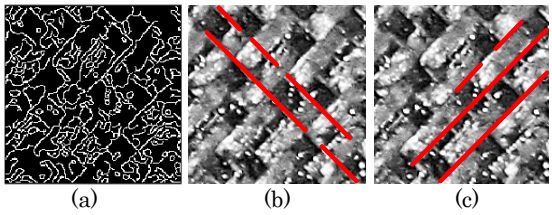

Fig. B.5: Steps in the fiber angle detection using Hough transform. (a) Binary image from edge detection, (b) lines detected for Fiber 1 family (c) lines detected for Fiber 2 family.

plained. The first step is to crop the image to the Region of Interest (ROI), i.e. the gage area. To ensure an even distribution of detected fiber angles throughout the ROI, the image is divided into a grid of cells, which shall be referred to as *Hough cells*. The idea is to detect a small number of lines (i.e. angles) within each Hough cell as shown in Fig. B.5. The steps in the figure are elaborated in the following. First, in each Hough cell, Contrast-limited adaptive histogram equlization (CLAHE) is applied to make sure that the image utilizes the entire range of gray-scale values. Hereafter, the image is sharpened using unsharp masking. Then, the cell is ready for the edge detection using the Canny algorithm followed by the Hough transform. The Hough transform is carried out for each family of fibers where the distinction is achieved by careful choice of the θ-values to search for: Using the frame angle associated with the current image and a specified tolerance, a desired range of θ-values can be calculated. Upon completing the analysis of all Hough cells, tows in the entire sample will have been detected.

To obtain a contour plot of the shear angle distribution, a grid of so-called *Contour cells* is introduced. Notice, that these are different from the Hough cells. The following is repeated for each family of fibers. For each contour cell, the detected fiber tows enclosed by the Contour cell are found, and the median value of the fiber angles together with the coordinates of the Contour cell center are stored in arrays. The array of Contour cell shear angles is then filtered using a 2D median filter. Next, a C^1 continuous surface is inter-

polated based on the coordinates and angles. Finally, the fabric shear angle distribution surface is obtained as the difference between the two interpolated surfaces.

B.4 Constant Shear Strain Rate Data

It is well established that prepreg fabric exhibits a rate-dependent behavior due to the presence of the viscous resin. To this end, constant shear rate data are of interest for two reasons: 1) For comparison with bias-extension test data at the same constant rate and 2) For use in forming simulation codes where test data can be input directly as the constitutive law. For instance, with the Abaqus *fabric* material model (Dassault Systèmes Simulia Corporation, 2014), stress-strain curves of constant strain rates can be input. Then by using interpolation, other strain rates are achieved in the material model. The testing at a constant shear rate is explained in the following.

B.4.1 Testing at a Constant Shear Rate

The approach for testing at a constant shear rate is as follows. First, a constant shear rate expression for the crosshead movement vs time is obtained. Next, this expression is approximated using linear segments such that it can be implemented in standard test machine software. In this study, the TestProfiler module in Bluehill 3 by Instron® is utilized.

For this study, the test shear rate was chosen such that it corresponds to the initial shear rate when testing at a crosshead rate of 100 mm/min. The shear rate is equal to 0.046 rad/s or 2.66 °/s.

The kinematic picture-frame relations were presented in Section B.3.1. Using these equations, the following differential equation can be obtained (see also Harrison et al. (2002)):

$$\dot{\delta}(t) = \frac{L_F \dot{\gamma}}{2} \sqrt{4 - \frac{\left(\delta(t) + L_F\sqrt{2}\right)^2}{L_F^2}} \tag{B.4}$$

Using the initial condition $\delta(0) = 0$, a closed form solution to Eq. (B.4) can be obtained. The expression, $\delta(t)$, is rather long and is not presented here. It is instead visualized in Fig. B.6 which consists of a crosshead movement vs. time graph and a shear-strain rate vs. time graph. The solution to Eq. (B.4), $\delta(t)$, (red dashed line) is compared to a constant crosshead rate (solid black line with circles) and the multi-linear approximation to the constant shear rate expression consisting of 20 segments (solid blue line). From Fig. B.6, right graph, it is seen that the constant crosshead rate results in an increas-

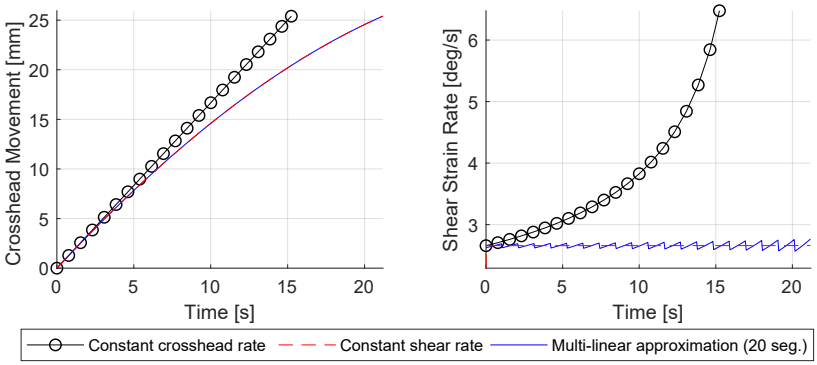

Fig. B.6: Constant crosshead rate vs constant shear rate and a multi-linear approximation.

ing shear-strain rate over time. In fact, the rate increases by a factor of 2.4 over the course of the test. The constant shear-rate crosshead movement and its multi-linear approximation are indistinguishable in the graph to the left whereas differences can be observed on the graph to the right where the rate is considered. Still, the multi-linear approximation is seen to provide a good approximation of the constant shear-strain rate. The slopes of the linear segments are obtained by dividing the nonlinear expression into 20 evenly spaced time intervals and computing secants using the start and end points of each interval. All three curves displace the crosshead 25.4 mm (1 inch) which results in a frame displacement of 108 mm due to amplification linkage.

The 20 linear segments can readily be implemented as ramp segments in the TestProfiler module in Bluehill. In the first step, the crosshead is moved until the empty frame plateau load of 100 N is reached. Notice that this rather high load is an effect of the amplifying linkage mechanism. Hereafter is the actual 20 segment ramp program executed.

B.5 Results

This section presents the results from the sample arm geometry study using DIC and Hough transform and finally the comparison to bias-extension data.

B.5.1 The Influence of Sample Arm Geometry

The influence of the sample arm geometry is evaluated by two different approaches. First, the influence on the measured shear load is examined. Next, it is investigated how the different sample arm geometries affect the state of the shear strain field in the gage area. Figure B.7 presents the crosshead force

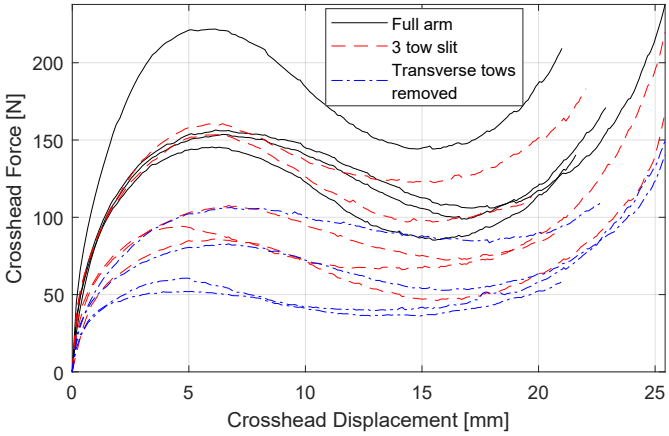

Fig. B.7: Crosshead force vs. displacement curves for samples with full arms, slitted arms and arms with transverse tows removed respectively. Notice that these crosshead values are different from the frame values due to the amplifying linkage mechanism.

vs crosshead displacement for all the tested samples. First of all, a lot of scatter is noticeable in the figure. As previously mentioned, the picture-frame test is sensitive to misalignments and differences in fiber tension. These sensitivities are believed to be the main causes of the scatter. Consider for instance the "Full arm" curve with the highest load in Fig. B.7. During testing, this sample had very little wrinkling in the arms compared to the three other "Full arm" curves. This difference could be an indication of higher tension in the tows, but because the tow tension cannot be quantified with the setup in this study, a definitive conclusion cannot be drawn. It is worth noting that none of the "3 tow slits" or "Transverse tows removed" samples wrinkled during testing. In fact, this lack of wrinkling is a strong indication that the arm geometry does influence the samples during shearing. Fig. B.8 depicts some typical deformed samples. In the figure it can be seen how the arm tows in the sample with the transverse tows removed tend to deform into S-shapes. This deformation is also sketched in Fig. B.9. The boundary conditions are the same for the other sample configurations, but the resulting deformations are different. The phenomenon can be considered as instability, i.e. shear buckling of the arm regions. For the slitted samples, out-of-plane twisting of the tows between the slits can be observed. The wrinkling observed with the full-arm samples is likewise believed to arise from the clamping boundary conditions.

In general, Fig. B.7 demonstrates a trend that the crosshead force decreases the more the sample arms are modified, i.e. from full arm to slitted arms and further to transverse tows removed. In Fig. B.10 the crosshead data have been converted to normalized shear force vs shear angle data using Eq. (B.1) and (B.3). Each family of curves has been averaged and the standard

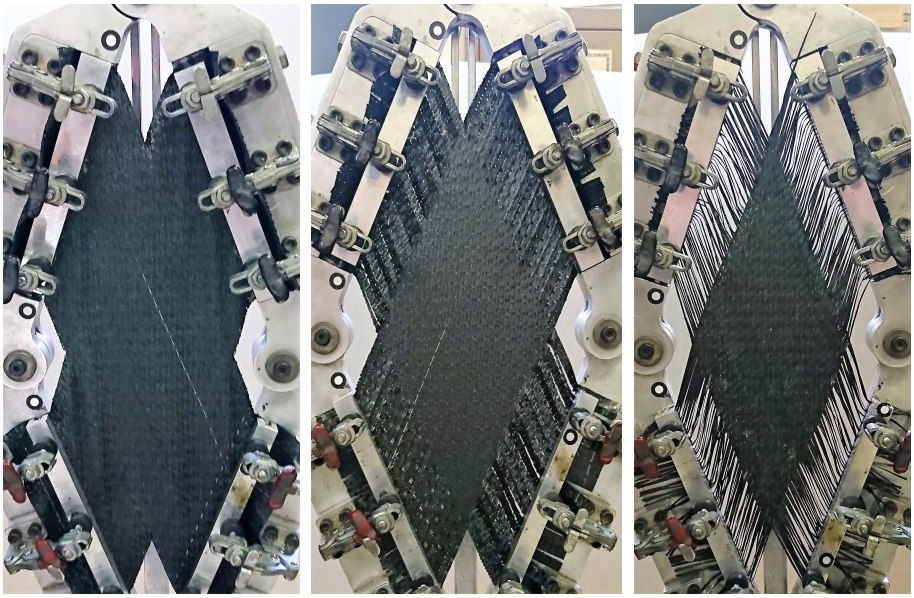

Fig. B.8: Deformed samples. From left to right: Full arm, 3 tow slits and Transverse tows removed.

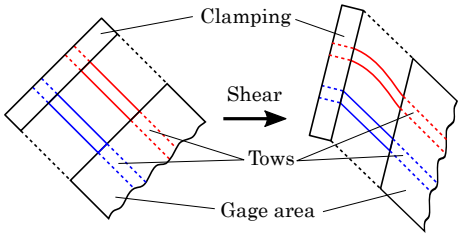

Fig. B.9: Effect of in-plane tow bending stiffness on the deformation in the arm regions. Lower, blue tow has zero bending stiffness, i.e. follows kinematic assumption, whereas the upper, red tow has a finite bending stiffness.

deviation is indicated with error bars. The trend from Fig. B.7 is replicated with the addition that the curves also become flatter with increasing sample arm modification.

In the following, the full-field DIC data are used to further analyze the different sample arm geometries. For the samples with modified arms, no useful DIC data are available in the arms due to the discontinuity of the sample surface. These discontinuities are visible in Fig. B.8.

To verify that the fabric shear angles follow the frame angles, all shear angles from each stage of the DIC data have been averaged. The averaged or *global shear angles* are plotted against the frame angle in Fig. B.11. In the

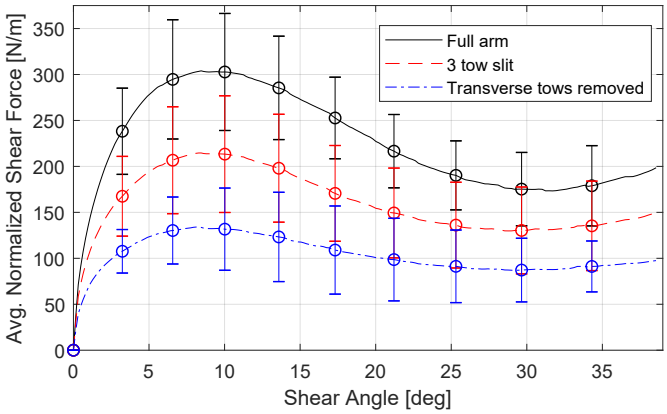

Fig. B.10: Averaged values of normalized shear force vs shear angle for samples with full arms, slitted arms and arms with transverse tows removed respectively. The error bars indicate the standard deviation.

figure, it is seen that all of the shear angles measured in the gage area follow the frame angle well, but the difference increases with increasing frame angle. The full-arm and the 3-tow slit curves are almost indistinguishable whereas the transverse tows removed is slightly lower. It is interesting though, that the closest results are observed for the full-arm geometry with shear angles measured over the entire area of the sample.

The question is next, how the distribution of shear angles changes with the different sample-arm geometries in the study. For reference, consider the full arm geometry sample in Fig. B.12. The contours covering the entire sample area indicate the distribution of the fabric shear angles at a picture-frame angle of 24°. In the gage area, the shear angles appear to be in the vicinity of 24° with some lower values near the boundaries. The arms of the sample, however, are exhibiting higher shear angles than the frame angle. This difference in the shear angles between these two regions on the test samples, explains the observations made regarding Fig. B.11: The shear angles are in general up to 2° behind the frame angle when considering the gage area, but the higher angles observed in the arms counteract this lag when the entire sample area is used for calculating the global shear angle.

Another interesting observation can be made from Fig. B.12 by looking closely at the gage area: Diagonal bands of slightly higher shear angles extend from one toggle clamp to another. These bands indicate that the clamping design does not provide a uniform amount of clamping force across the width of the sample.

Due to the aforementioned availability of the DIC data, the comparison between the shear angle distribution for the different arm geometries in Fig. B.13 only concerns the gage area. In the comparison, the frame angle

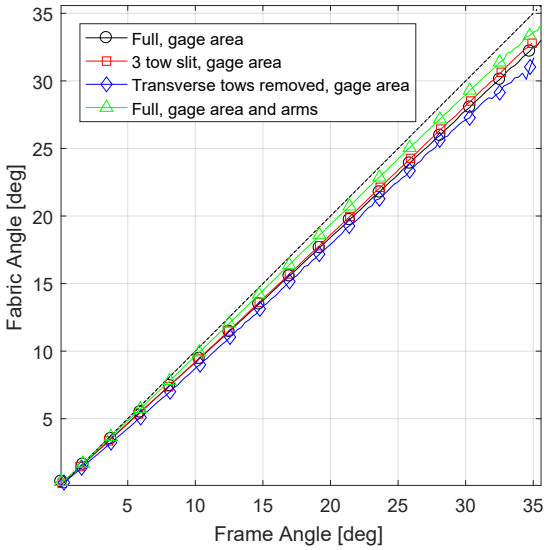

Fig. B.11: DIC fabric angles vs frame angles from the gage area of full arm geometry, 3-tow slits and transverse tows removed. Also from entire sample with full arm geometry. The theoretical 1:1 line is shown as black dots.

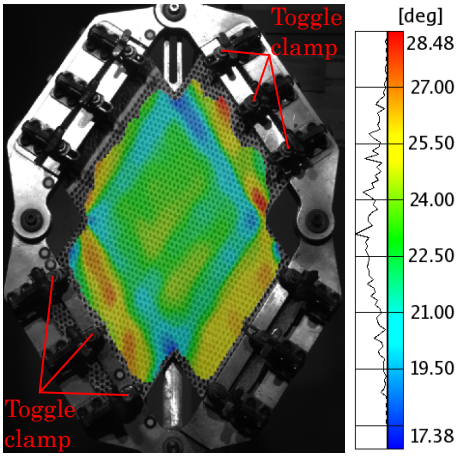

Fig. B.12: Distribution of the shear angles in sample with full-arm geometry at a picture-frame angle of 24°.

is 18°.

In Fig. B.13, each of the contour scales has been set to the same maximum and minimum values. With aid from the histogram next to each colorbar, the following remarks can be made: The full-arm geometry and 3-tow slits samples both have a fairly uniform distribution of shear angles although the

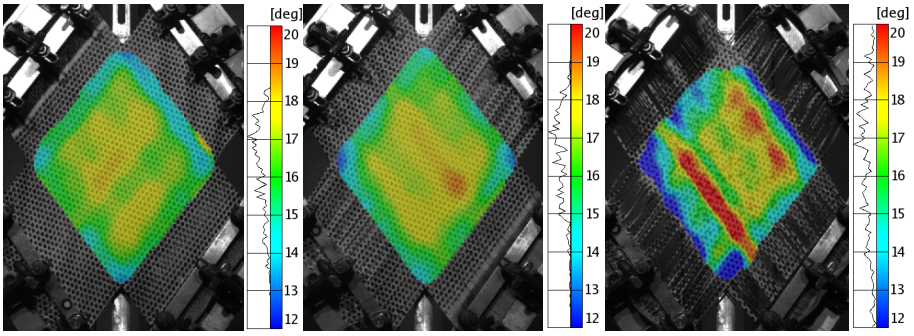

Fig. B.13: Comparison of DIC shear angles in gage area for full arm geometry (left), 3 tow slits (middle) and transverse tows removed (right). The frame angle is 18°.

3-tow slits sample has fewer boundary effects. In the sample with transverse tows removed, the distribution of shear angles is less uniform. The contours show the effect of uneven tension in the tows which results in shear angles that are both significantly higher and lower than the frame angle.

It must be pointed out that the DIC results only represent one sample within each configuration of arm geometry. However, because the average fabric angles follow the frame angle well, it is believed that the results from Fig. B.13 are generally applicable to the the tested material system.

In general, it can be stated that the samples with transverse tows removed require a significantly lower force to be sheared compared to the full-arm samples. The DIC results indicate that the distribution of shear angles is more scattered in samples with transverse tows removed in comparison to the other sample geometries, but the average shear angle in the gage area shows only a minor lag.

B.5.2 Shear Angles from Hough Transform

In this paragraph, the Hough transform approach for obtaining the shear angles is evaluated. Full-field shear-angle data from 3-tow slits and transverse-tows-removed samples are presented for comparison of the Hough transform approach with the DIC results. Notice, however, that the speckle pattern on the DIC samples inhibits the detection of fiber angles from the weave texture. Further, both acquisition methods are sensitive to the right lighting conditions and thus, the same sample cannot conveniently be analyzed using both DIC and Hough transform during testing. For this reason, the Hough transform results were validated by means of manual measurements on the images acquired during the test. The Hough transform settings used are listed in Table B.2.

The full-field results from the Hough transform are presented in Fig. B.14

Table B.2: Parameters used for Hough transform. Some settings are different for the fibers families due to fiber family 2 being more visible in the weave pattern. †The Hough cell vertical size is determined based on the horizontal size and the image aspect ratio. The image size is 3456 × 5184 pixels.

Parameter	Fiber 1	Fiber 2
θ tolerance rel. to frame	$\pm 10^\circ$	$\pm 10^\circ$
Number of Hough peaks	5	7
Min. length in line extraction	21 pix	25 pix
Fill gap value in line extraction	10 pix	12 pix
Hough Cell horizontal size†	165 pix	
Hough Cell overlap	50 %	
Contour Cell size	130 pix	
Contour Cell overlap	50 %	
Median filter size	5×5	

(initial configuration, i.e. undisplaced frame) and Fig. B.15 (18° frame angle). It was found that the initial configuration did not have perfectly 90° tow angles as seen in Fig. B.14. This pre-shear was likely induced during mounting in the frame as the figure suggests the effects of clamping. The pre-shear could also occur during preparation of the sample or even at an earlier stage. Regardless, it should receive more attention in future studies. For the purpose of comparison with the DIC results, the average shear angle from the initial configuration was subtracted from the deformed full-field data. The average initial shear angles were 1.35° (3 tow slits) and 0.46° (transverse tows removed) respectively. Pre-shear is not a new concept and was for instance investigated by Alsayednoor et al. (2017) in relation to the bias-extension test.

The Hough transform results obtained with an 18° frame angle in Fig. B.15 show the same trends as observed with the DIC results in Fig. B.13. The 3-tow-slits sample has a fairly uniform distribution of shear angles with some boundary effects whereas the transverse-tows-removed sample has a lot less uniform distribution. Due to noise in the results, the spatial resolution is low compared to the DIC results and a considerable amount of filtering was applied. For this reason, the present Hough transform results are only suitable for exploring the trend or for obtaining a global shear angle. Hence, by averaging the shear angles for the two contour plots in Fig. B.15 respectively, global shear angles of 16.88° (3-tow slits) and 17.96° (transverse tows removed) are obtained. These values compare well with the global shear angles from DIC in Fig. B.11.

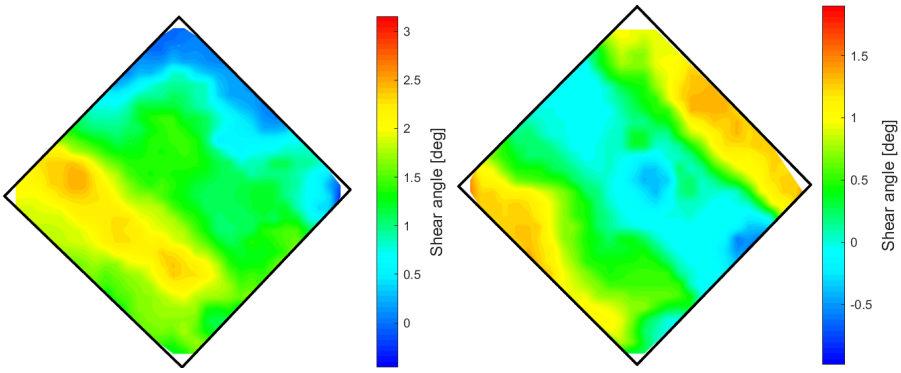

Fig. B.14: Shear angles in the gage area for the undisplaced frame obtained using Hough transform. Sample configurations: 3-tow-slits (left) and transverse-tows-removed (right). The colorbars are centered around the mean and span ± 3 standard deviations.

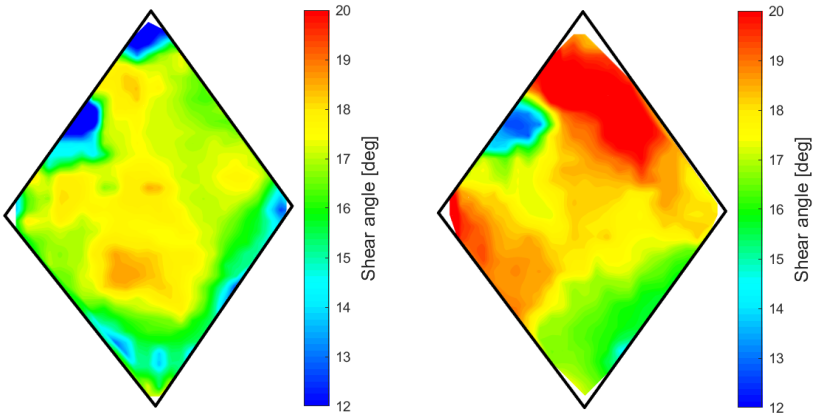

Fig. B.15: Shear angles in the gage area for 18° frame angle obtained using Hough transform. Sample configurations: 3-tow-slits (left) and transverse-tows-removed (right).

B.5.3 Comparison to Bias-Extension Data

In this section the picture-frame test results are compared to results obtained with the bias-extension test. The question is, however, what test configuration of picture-frame results should be used for the comparison. The normalized shear force curves in Fig. B.10 along with the DIC results indicate that results obtained from the samples with the transverse tows removed provide the best representation of the material's shear characteristic. Recall though, that Eq. (B.3) from Peng et al. (2004), which was used for normalization of the picture-frame crosshead force data, assumes that only the gage area contributes to the shear force. In the same paper, the authors present a normalization equation based on the assumption that the entire sample contributes

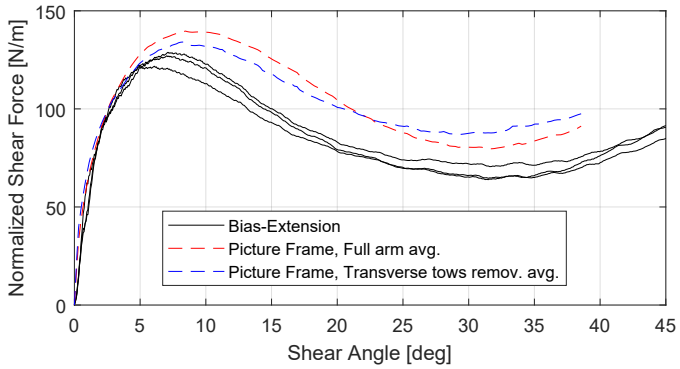

Fig. B.16: Comparison between picture frame and bias-extension results.

to the shear force:

$$F_{sh,norm\_entire} = \frac{L_F}{L_f^2 + 2(L_F - L_f)L_f} F_{sh} \tag{B.5}$$

The assumption of shear force contributions from the entire sample can be justified using Fig. B.12. This figure shows, that the arms of the standard cruciform sample do indeed experience shearing to the same extent as the gage area. Thus, in the following, the picture-frame data used for comparison are the transverse-tows-removed data from Fig. B.10 and the averaged full-arm crosshead data normalized with Eq. (B.5).

Regarding the bias-extension data, a sequence of linear ramps have been implemented in the test machine control software analogous to Sec. B.4.1. Thereby the same constant shear rate of 0.046 rad/s can be achieved. Three samples of 120 mm $\times$ 270 mm were tested. The load cell used had a capacity of 2 kN (0.4 % accuracy). The data processing, i.e. calculation of shear angle and normalized shear force, follows the description in Cao et al. (2008). Videos of the specimens during testing were analyzed using Hough transform to extract the average fabric shear angle in the center zone and to correct the calculated angle. The Hough transform results were again validated using manual measurements.

The comparison between picture-frame and bias-extension results is presented in Fig. B.16. Regarding the bias-extension data in the figure, it is seen that the three test results are very close to each other with a maximum absolute deviation between the curves of only 10 N/m. Thus, the issue with uneven fiber tension between different samples in the picture frame test is avoided with the bias-extension test. Regarding the two sets of picture frame data, it is remarkable how the different normalization methods manage to bring the curves close to each other. Finally, comparing the picture frame

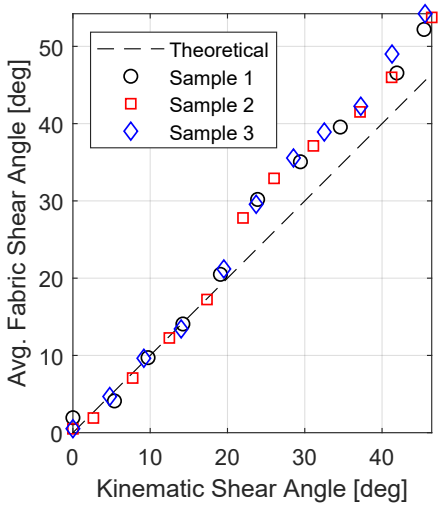

Fig. B.17: Measured vs. kinematic shear angles in center region of bias-extension samples.

data with the bias-extension data, a fairly close resemblance is observed. It must be noted that the shear force from the bias-extension test is calculated using a formula derived for dry fabrics. Thus, it naturally introduces errors.

For reference, a result from the Hough transform image analysis of the bias-extension test is presented in Fig. B.17 as the average fabric shear angle vs. the kinematic shear angle. The former is the average of the measured shear angles in the center region of the specimen and the latter is obtained based on the distance between the grippers. It is seen that the measured angles follow the kinematic angles until around 20° after which they start to deviate to higher values. It is believed that this phenomenon arises from so-called 2nd gradient effects (Ferretti et al., 2014): At the boundaries between the shear zones in the sample, the in-plane bending stiffness of the tows inhibits a sharp shear angle transition. This violates the pin-jointed net assumption behind the bias-extension kinematics. The same phenomenon was e.g. also observed in the data presented in Alsayednoor et al. (2017).

B.6 Discussion

The work presented in this paper enables the drawing of many conclusions, but some points are up for discussion. Consider, for instance, the reason for testing the fabric at a constant shear rate and in a manner which provides a uniform shear-angle distribution in the sample: The idea is to get a more accurate shear characteristic compared to the usual test procedure. However, as was demonstrated, the modification of the sample arms resulted in more scat-

ter in the data because the samples were more difficult to mount properly in the frame than the baseline configuration samples. The current picture-frame design with toggle clamps also caused issues in terms of the uniformity of the shear-angle field - especially with the modified samples. To this end, various design improvements of the picture frame can be found in the literature (Launay et al., 2008; Milani et al., 2010; Nosrat-Nezami et al., 2014).

Steps could of course be taken to alleviate the issues mentioned above, e.g. by keeping the fabric material intact in the part of the sample arm that is clamped. Effectively, that would mean to remove only the transverse tows in some part of the arm. However, the sample preparation used in this study was already cumbersome. Thus, the best recommendation for picture-frame testing of the prepreg fabric used in this study would be to use the original cruciform sample and normalize the shear force assuming that the entire sample area contributes to the shear force. As was seen in Fig. B.16, this approach yielded a good agreement with the modified-sample and bias-extension data.

The image processing results using the Hough transform were able to replicate the trends observed with the DIC results. A lot of noise was present in the located fiber angles which was reduced by means of filtering. One issue was glare effects due to the resin on the prepreg material. Thus, the measurement signal could maybe be improved by testing with polarized light in combination with a polarizing filter on the camera lens. Another option would be to paint a grid on the sample as utilized by Arumugam et al. (2016). Here, the grid lines should preferably be centered on the tows which could be accomplished with a stencil. However, as previously discussed, one important benefit of the present approach is that the samples are completely unaffected by the shear angle measurement.

The Hough transform method also has its limitations. In fact, it concerns a general issue for 2D measurement techniques as investigated by Alsayednoor et al. (2017): If the bias-extension sample wrinkles, the out-of-plane displacements can cause the angle-measurements to be 20% higher than the true value. In this case, a 3D technique needs to be employed. When the sample shears, the two families of tows cross over each other. Thus, the best measurements are obtained in the initial configuration. With this in mind, another possible application of the Hough transform would be only to inspect the sample in the picture frame before the start of the test. If the frame is also identified in the image, the fiber angles relative to the frame could be obtained.

Another interesting point is the influence of the modified sample arms when comparing to the similar study by Dangora et al. (2015) using preconsolidated UD cross-ply. In that study, similar decreases in the magnitude of the crosshead force were observed with increasing arm modification but in contrast to this study, a pronounced and critical effect on the uniformness of

the shear strain field in the gage area was observed. One explanation for this result is that the UD cross-ply has much less interaction between the two fiber directions which could mitigate the effects of uneven clamping forces. This underlines that one should be careful to draw general conclusions based on one material study. To this end it would be interesting to test more material systems, e.g. with different fiber architectures, different fiber materials and different matrix materials.

B.7 Conclusion

This paper has presented the results of an investigation concerning the shear characterization of woven prepreg fabric using the picture-frame test. In particular, the influence of the cruciform-sample arms, methods for acquiring shear angles and the concept of testing at constant shear-strain rates were examined.

Testing at a constant shear-strain rate was achieved by considering the kinematics of the picture frame whereby a nonlinear expression for the crosshead displacement vs. time was obtained. The nonlinear expression was implemented in the control software of the tensile-test machine by means of a series of ramp segments. Using this approach, picture-frame data can be objectively compared to bias-extension data, when the test rate is of importance.

The investigation of the influence of the sample arm geometry involved modifications to the original cruciform sample. The first modification was cutting of slits in the arms while the second was dissolving the resin and removing the transverse tows in the arms. Using DIC, it was first established that a slitted sample had a slight improvement on the uniformity of the shear-strain field compared to an original cruciform sample, whereas a sample with transverse tows removed had a less uniform distribution. The latter observation was ascribed to the fact that the sample was more difficult to mount correctly in the frame such that the tow tension was even. For all three kinds of samples the average shear angles were close to the calculated angles from the kinematics of the picture frame.

Comparing the measured crosshead forces between the three different sample geometries, a large difference was observed. Namely, the forces measured from the original sample geometries were approximately twice of those from the samples with the transverse tows removed. This difference clearly indicates that the arms of the cruciform sample influence the measured results.

Next, it was investigated if shear angles could be obtained directly from images taken during the test by using image processing. In particular, whether a Hough transform could locate the fiber directions using only the weave structure. With the setup used in this study, the approach managed to cap-

ture the trend in the shear-angle distribution when comparing to DIC and to predict the average shear angle well. There is potential for improvement, but the present results work as a proof of concept for further development.

Finally, comparing the data of the normalized shear force vs. shear angle from the picture-frame test with bias-extension test results obtained at the same constant shear-angle rate, good agreement was found. Here, different normalization schemes for the picture-frame test shear force were employed. Namely, the original cruciform sample data were normalized assuming contributions from the gage area and the arms, whereas the transverse-tows-removed data were normalized assuming only contributions from the gage area. The two normalization schemes brought the shear force curves remarkably close to each other. Thus, the recommendation regarding picture frame testing of the prepreg material in this study, is to test the original cruciform sample and normalize assuming contributions from the entire sample.

Acknowledgments

The authors wish to thank the Innovation Fund Denmark (grant no. 5163-00003B) for providing support for the research presented in the paper. The authors also thank Terma Aerostructures A/S for providing the material.

Conflict of Interest

The authors declare that they have no conflict of interest.

References

Alsayednoor J, Harrison P, Yu WR (2017) Influence of specimen pre-shear and wrinkling on the accuracy of uniaxial bias extension test results. Composites Part A: Applied Science and Manufacturing 101:81–97, DOI 10.1016/j.compositesa.2017.06.006

Arumugam V, Mishra R, Militky J, Tunak M (2016) In-plane shear behavior of 3D spacer knitted fabrics. Journal of Industrial Textiles 46(3):868–886, DOI 10.1177/1528083715601509

Cao J, Akkerman R, Boisse P, Chen J, Cheng HS, de Graaf EF, Gorczyca JL, Harrison P, Hivet G, Launay J, Lee W, Liu L, Lomov SV, Long A, de Luycker E, Morestin F, Padvoiskis J, Peng X, Sherwood JA, Stoilova T, Tao X, Verpoest I, Willems A, Wiggers J, Yu T, Zhu B (2008) Characterization of mechanical behavior of woven fabrics: Experimental methods and benchmark results. Composites Part A: Applied Science and Manufacturing 39(6):1037–1053, DOI 10.1016/j.compositesa.2008.02.016

Dangora LM, Hansen CJ, Mitchell CJ, Sherwood JA, Parker JC (2015) Challenges associated with shear characterization of a cross-ply thermoplastic lamina using picture frame tests. Composites Part A: Applied Science and Manufacturing 78:181–190, DOI 10.1016/j.compositesa.2015.08.015

Dassault Systèmes Simulia Corporation (2014) Abaqus 6.14 Documentation: 23.4.1 Fabric material behavior

Ferretti M, Madeo A, Dell'Isola F, Boisse P (2014) Modeling the onset of shear boundary layers in fibrous composite reinforcements by second-gradient theory. Zeitschrift fur Angewandte Mathematik und Physik 65(3):587–612, DOI 10.1007/s00033-013-0347-8

Harrison P, Clifford M, Long A (2002) Constitutive modelling of impregnated continuous fibre reinforced composites micromechanical approach. Plastics, Rubber and Composites 31(2):1–12, DOI 10.1179/146580102225001409

Harrison P, Clifford M, Long A (2004) Shear characterisation of viscous woven textile composites: A comparison between picture frame and bias extension experiments. Composites Science and Technology 64(10-11):1453–1465, DOI 10.1016/j.compscitech.2003.10.015

Harrison P, Wiggers J, Long A (2008) Normalization of shear test data for rate-independent compressible fabrics. Journal of Composite Materials 42(22):2315–2344, DOI 10.1177/0021998308095367

Harrison P, Alvarez MF, Anderson D (2018) Towards comprehensive characterisation and modelling of the forming and wrinkling mechanics of engineering fabrics. International Journal of Solids and Structures 154:2–18, DOI 10.1016/j.ijsolstr.2016.11.008

Jauffrès D, Sherwood JA, Morris CD, Chen J (2010) Discrete mesoscopic modeling for the simulation of woven-fabric reinforcement forming. International Journal of Material Forming 3(SUPPL. 2):1205–1216, DOI 10.1007/s12289-009-0646-y

Krieger H, Kaufmann D, Gries T (2015) Kinematic drape algorithm and experimental approach for the design of tailored non-crimp fabrics. Key Engineering Materials 651-653:393–398, DOI 10.4028/www.scientific.net/KEM.651-653.393

Krogh C, Glud JA, Jakobsen J (2019) Modeling the robotic manipulation of woven carbon fiber prepreg plies onto double curved molds: A path-dependent problem. Journal of Composite Materials 53(15):2149–2164, DOI 10.1177/0021998318822722

Launay J, Hivet G, Duong AV, Boisse P (2008) Experimental analysis of the influence of tensions on in plane shear behaviour of woven composite reinforcements. Composites Science and Technology 68(2):506–515, DOI 10.1016/j.compscitech.2007.06.021

Lebrun G, Bureau MN, Denault J (2003) Evaluation of bias-extension and picture-frame test methods for the measurement of intraply shear properties of PP/glass commingled fabrics. Composite Structures 61(4):341–352, DOI 10.1016/S0263-8223(03)00057-6

Lomov SV, Boisse P, Deluycker E, Morestin F, Vanclooster K, Vandepitte D, Verpoest I, Willems A (2008) Full-field strain measurements in textile deformability studies. Composites Part A: Applied Science and Manufacturing 39(8):1232–1244, DOI 10.1016/j.compositesa.2007.09.014

Lussier D (2000) Shear characterization of textile composite formability. Master's thesis, University of Massachusetts, Lowell

Marques O (2011) Practical Image and Video Processing Using MATLAB. John Wiley & Sons, DOI 10.1002/9781118093467

Milani AS, Nemes JA, Lebrun G, Bureau MN (2010) A comparative analysis of a modified picture frame test for characterization of woven fabrics. Polymer Composites 31(4):561–568, DOI 10.1002/pc.20849

Mohan RP, Alshahrani H, Hojjati M (2016) Investigation of intra-ply shear behavior of out-of-autoclave carbon/epoxy prepreg. Journal of Composite Materials 50(30):4251–4268, DOI 10.1177/0021998316635238

Nguyen M, Herszberg I, Paton R (1999) The shear properties of woven carbon fabric. Composite Structures 47(1-4):767–779, DOI 10.1016/S0263-8223(00)00051-9

Nosrat-Nezami F, Gereke T, Eberdt C, Cherif C (2014) Characterisation of the shear-tension coupling of carbon-fibre fabric under controlled membrane tensions for precise simulative predictions of industrial preforming processes. Composites Part A: Applied Science and Manufacturing 67:131–139, DOI 10.1016/j.compositesa.2014.08.030

Olson BG, Krieger H, Sherwood JA, Willis DJ, Bergeron K (2017) Investigation of Tensile Properties of Braided Parachute Suspension Line. In: 24th AIAA Aerodynamic Decelerator Systems Technology Conference, American Institute of Aeronautics and Astronautics, Denver, Colorado, DOI 10.2514/6.2017-4198

Peng X, Cao J (2005) A continuum mechanics-based non-orthogonal constitutive model for woven composite fabrics. Composites Part A: Applied Science and Manufacturing 36(6):859–874, DOI 10.1016/j.compositesa.2004.08.008

Peng X, Cao J, Chen J, Xue P, Lussier DS, Liu L (2004) Experimental and numerical analysis on normalization of picture frame tests for composite materials. Composites Science and Technology 64(1):11–21, DOI 10.1016/S0266-3538(03)00202-1

Zhu B, Yu TX, Tao XM (2007) An experimental study of in-plane large shear deformation of woven fabric composite. Composites Science and Technology 67(2):252–261, DOI 10.1016/j.compscitech.2006.08.011

Paper C

Generation of Feasible Gripper Trajectories in Automated Composite Draping by means of Optimization

Christian Krogh, James A. Sherwood & Johnny Jakobsen

The paper has been submitted.

The included paper is the submitted preprint.
The layout has been revised.

Abstract

Prepreg composites find great applicability in e.g. the automotive and aerospace industries. A major challenge with this class of material systems is the accurate placement of a fabric that can be very tacky and hence sticks to the mold surface. In this study, automatic draping of entire plies of woven prepregs is considered. A robot end effector with a grid of actuated grippers is under development and it has the ability to position the plies onto double-curved mold surfaces of low curvature. The key issue is how the grippers of the end effector should move to achieve successful drapings of the plies that meet the quality requirements of the industry. In this study, an approximate ply model based on cables with bending stiffness is applied in an optimization framework where the gripper movements constitute the design variables. The optimization framework has taken inspiration from manual layup procedures. The numerical draping results indicate the usefulness of the cable model used in connection with the optimization framework. The next step is to implement the generated gripper trajectories on the physical robot system.

Keywords Woven prepreg, Forming, Trajectory Optimization, Offline Motion Planning, Automation

C.1 Introduction

Although composites exhibit properties that are very desirable from a mechanical point of view, a major drawback is the cost associated with their manufacturing, which is dominated by manual steps, e.g. hand placement of plies. To this end, significant research efforts are being pursued for lowering the manufacturing cost by utilizing robots (Björnsson et al., 2017). In the *FlexDraper* research project, a robot end effector with an array of actuated grippers is employed to manipulate entire woven prepreg plies onto double-curved mold surfaces of low curvatures. Prepreg plies comprise a fabric which is pre-impregnated with resin. This operation constitutes an automatic draping process that can directly replace the manual hand layup.

A key issue related to the automation of the draping process, is the concept of *draping strategies* which for the robot system translates to its gripper trajectories. Handling of the prepreg ply by the FlexDraper robot system was previously studied by means of a nonlinear, rate-dependent finite element (FE) model (Krogh et al., 2019a). It was found that the end result is highly dependent on the gripper paths and that wrinkles can easily form during draping. In an industrial context, it is essential to avoid wrinkling.

The manufacturing of composite preforms with a punch, die and blank

holder is a common operation in e.g. the automotive industry. To this end, the pressure distribution created by the blank holder over the course of the process cycle has been subject to optimization with the purpose of avoiding wrinkling (Lin et al., 2007; Zhu et al., 2008). Recently, the concept of a multi-punch tool with individually controllable segments has also been investigated (Coutandin et al., 2018).

Concerning composite layup on a mold surface, a number of research groups have been studying automation of the process and the concept of draping sequences. Eischen and Kim (1993) considered the automatic placement of a strip of apparel fabric on a flat surface. By means of optimization the authors generated manipulator paths that minimized the reaction force. In the work by Reinhart and Ehinger (2013), a robot end effector in the form of an elastic roller with suction was used to drape carbon-fiber preforms for subsequent resin infusion. The authors discussed different *draping strategies* for a number of molds, i.e. rolling motions of the tool in different directions. Molfino et al. (2014) outlined a *handling strategy* for use with a robot system which relies on a 3D laser scanner. The laser scanner was used to identify placing strategies on the mold for dry fabric. Nagele et al. (2015) presented a *backward-oriented* approach for offline programming of the draping process of dry fabrics for a system with a grid of grippers. The idea is to start from the draped configuration and then determine robot sequences to some starting point. It is, however, not clear how well the approach can take the path-dependency of the prepreg ply into account.

Catenary models have been explored by some researchers for representing the ply behavior. Flixeder et al. (2017) developed a force-based control system for handling of dry 2D fabrics, where the manipulator movements are generated online using a catenary model. A catenary model was also used by Eckardt et al. (2016) for the purpose of finding the inclination of the grippers which will not induce any unnecessary bending in the dry fabric. In their paper, the authors also discussed the use of a *seed point* or *seed curve* from where the draping can start, which originates from manual layup. They investigated three manually created draping strategies on a single-curved demonstrator part. The first two draping strategies were rejected due to induction of defects while the third was successful.

Brinker et al. (2017) discussed *drape paths* and presented a figure with discrete gripper trajectories arising from a kinematic drape simulation. Newell and Khodabandehloo (1995) presented a large deflection beam model for draping automation and experimentally validated it against a strip of prepreg. Also, a large-deflection shell model was introduced by Lin et al. (2009) for real time ply prediction under certain pre-defined boundary conditions.

The references mentioned above all provide inspiration for the work presented in this paper but the methods are not directly applicable to draping of prepreg fabric on arbitrary 3D molds with the particular robot tool consid-

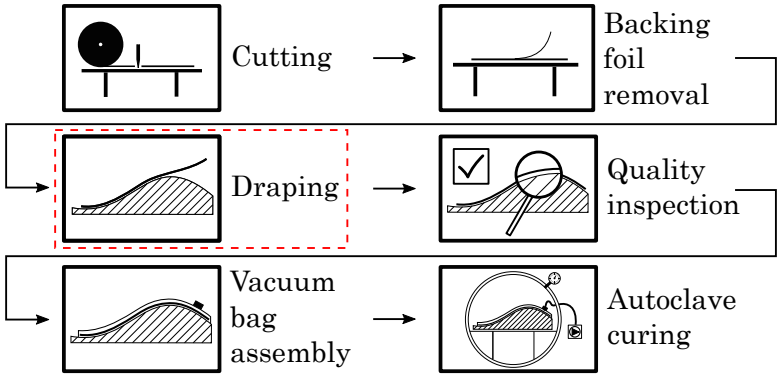

Fig. C.1: The major steps in the production of prepreg composites. This paper concerns the draping step.

ered in this study. The goal of the current study is to generate feasible draping sequences, i.e. off-line gripper trajectories, for the robot of the FlexDraper project. The generation must be done automatically. Here, a computationally efficient fabric model based on cables with bending stiffness is employed to predict the mechanical behavior of the prepreg ply during draping. The trajectories are generated by means of an optimization scheme which incrementally moves the grippers based on the predicted ply response. The rest of the paper is organized as follows: Section C.2 provides a detailed description of the problem to be solved and the robot tool. Section C.3 introduces the cable fabric model and discusses its properties. Section C.4 presents the optimization scheme and Section C.5 presents numerical results. Finally, a discussion and a conclusion complete the paper.

C.2 Problem Description

The draping process is only one step in the production of prepreg composites as outlined in Figure C.1. The draping process consists of picking up a flat ply and conforming it to a mold surface. The governing deformation mode that allows the ply to undergo a deformation from flat to double curved is known as trellising or fabric shearing. This shearing entails, as seen in Figure C.2, that the fiber tows in the weave rotate at their crossover points such that the angles change from the initially 90°. Notice, therefore, that the draping process is not simply a pick-and-place operation.

The amount of shearing necessary for a given draping process mainly depends on the curvature of the mold. The amount of shearing that can be realized with the fabric depends on several factors, of which the fabric architecture, e.g. weave pattern and tow spacing, is highly important. At a certain

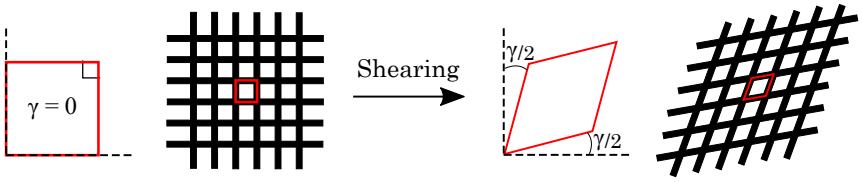

Fig. C.2: Fabric shear involving fiber tows rotating at the cross-over points. γ is the shear angle.

degree of shear, known as the *locking-angle*, the neighboring tows start to make contact which usually entails wrinkling. Notice though, that wrinkling is a complex phenomenon that does not solely depend on the shear angle. This study focuses on low-curvature molds without sharp corners which enables the plies to be readily draped without post-treatment and without the fabric reaching the locking angle. The Gaussian curvature of the mold in this study ranges between -25 m^{-2} and 23 m^{-2}.

There are certain quality requirements to the draping process. The draped ply must conform to the mold surface without wrinkles and air pockets. Also, the boundary of the ply must follow a prescribed boundary on the mold. The tolerances on the ply-mold alignment and boundary depend on the industry and the specific part but are usually in the order of a few millimeters.

The ply material used in this study is a woven fabric which is pre-impregnated with the resin - a *prepreg*. The resin influences the ply behavior in two ways. First, the bending stiffness of the otherwise limp fabric increases. Second, the tackiness causes the interface friction to become significant. Notice though, that the general methodology is not restricted to a particular material system.

C.2.1 The Robot System

The concept of the new robot end effector under development is shown in Figure C.3. The tool consists of an array of suction cups or *grippers* with a diameter of 40 mm. The grid in Figure C.3 is 2 $\times$ 2, and this grid size along with a 3 $\times$ 2 grid is studied in this paper using a numerical approach. The tool may potentially be expanded to a higher number of grippers. The idea is that the three translational degrees of freedom for each gripper can be controlled. The vertical z rotational degree of freedom, i.e. yaw, is locked, whereas the two remaining rotational degrees of freedom are free to the extent allowed by the flexible bellow. It is assumed that rotations up to 40° are achievable. The work envelope of the tool is such that a 150-mm initial spacing between the center of the grippers is appropriate. The fiber directions are parallel to the edges of the ply.

The hardware design of the tool offers great flexibility in terms of different mold geometries and ply shapes. Thus, the intended use is not mass

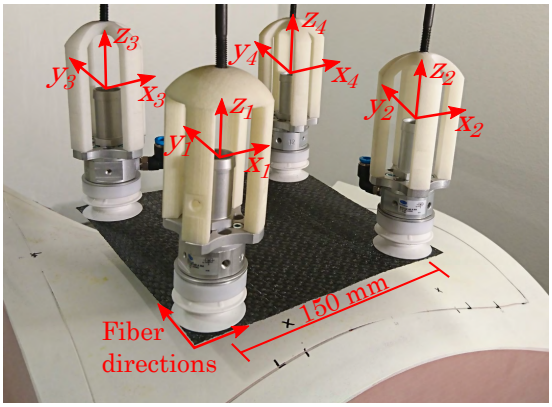

Fig. C.3: The concept of the robot end effector under development with a 2×2 grid of x, y, z controllable suction cups. The prepreg ply is held above the mold.

production but instead small batches. To this end, reconfiguring the automatic draping system for a new mold-ply kit should be reasonably fast.

In a previous study by Krogh et al. (2019a), the prepreg material was characterized experimentally for the in-plane tension and shear and out-of-plane bending responses. This characterization was used as the basis for a nonlinear rate-dependent finite element (FE) model. While this model gives good predictions of the ply deformation field during draping it is also computationally expensive; a typical draping simulation takes in the order of hours to complete. Thus, its use in an optimization framework would entail very long computation times. With the flexibility required for the automatic robot draping system, a faster, approximate model is desired. This need is the motivation for applying the approximate ply model based on cables to predict the mechanical behavior of the ply.

C.2.2 Challenges with regard to Automatic Draping

Automatic draping with the robot system poses some challenges. In general, there are two main issues to address: where the grippers should pick up the ply and afterwards how the grippers should move during draping, i.e. the placing of the ply on the mold surface.

With regard to where the grippers should pick up the ply, these locations could be dependent on both the ply and the mold. It might be beneficial that the grippers pick the ply at its boundary such that it can be controlled. Another concern could be to have as much of the suction area as possible covered by the ply. On the other hand, certain characteristics on the mold, such as high curvatures or concave regions, might make some gripper touchdown locations more favorable than others. In this study, a rectangular ply is

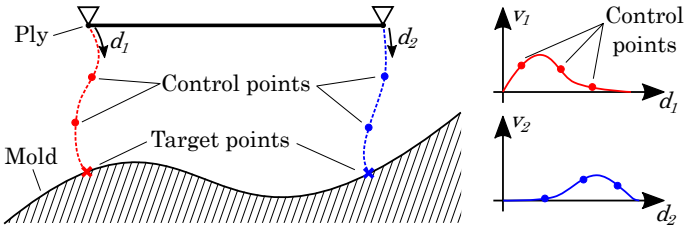

Fig. C.4: Possible parameterization of gripper trajectories (d_1 and d_2) and velocity profiles (V_1 and V_2) using splines.

considered and thereby the grippers on the robot system will be arranged in a rectangular grid during pick-up. The determination of optimal pick locations in terms of the mold and non-rectangular plies is left for a future study.

The remaining issue is how the grippers should move during draping. As an aid, the final locations of the grippers on the mold or *target points* can be predicted using a kinematic mapping algorithm (Van Der Weeën, 1991). The basic idea is to preserve the fabric length in the fiber directions on the mold while allowing shearing. Details of the calculation of the target points can be found in Krogh et al. (2019a).

With the above challenges in mind, the task is to determine the path from the initial position of the grippers to their respective target points by means of optimization. Without making any limiting decisions a priori, one possible parameterization would be to employ interpolating functions, for instance splines as shown in Figure C.4. Here, it is envisioned that a number of control-point design variables define splines which will determine the trajectory of a gripper together with the corresponding velocity profile. The objective function to be minimized could be a *drape quality measure* involving the mold-ply distance for the draped ply. Hereby, an objective function evaluation necessitates a simulation of the entire draping sequence. The control points are updated until the drape quality measure is sufficiently low.

Another idea is to take a more heuristic approach, employing information from manual layup. Here, the operator tends to choose some initial contact or *seed point* from where the ply is draped in an incremental manner. The contact front thus advances away from the seed point in a manner where the movement of the ply mimics a wave. This motion is continued until the entire ply is draped. This drape motion helps to mitigate wrinkles and issues with entrapped air that occur due to bridging.

A parameterization based on the heuristics of manual layup is depicted in Figure C.5. The draping of the ply is divided into iterations. In each iteration, an optimization problem is solved where the design variables are the gripper positions, and the objective is to bring the ply closer and closer to a draped configuration. Careful choice of optimization criteria will generate

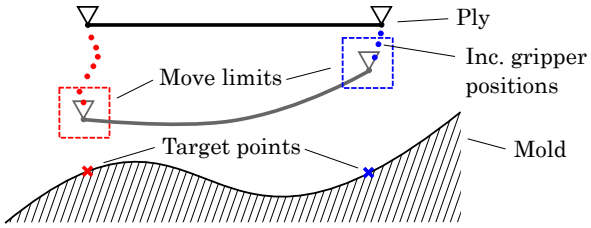

Fig. C.5: Parameterization using incremental optimization with inspiration from manual layup.

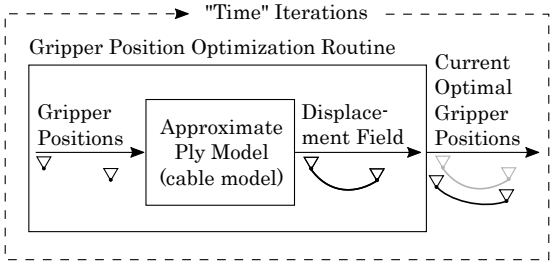

Fig. C.6: Flowchart of the incremental optimization scheme. "Time Iterations" denote the iterations in which the discrete trajectory points are obtained.

the wave-shaped drape motion. Move limits are imposed to make sure the grippers travel in small increments. Then, a call to the objective function only requires an evaluation of the ply model in a single gripper configuration. When all the grippers eventually make contact with the mold, the process is terminated, and the locus of the incremental positions of a gripper constitute its trajectory.

Due to the well-proven wave-shape drape motion and the fact that the incremental optimization scheme is more computationally efficient than the spline-interpolation scheme, it is employed in the present study. A flowchart of the gripper optimization process is presented in Figure C.6.

C.3 The Cable Model

The key concept of the approximate model is to suspend cable curves between the center points of the grippers. By this simplification, the actual gripper geometry is ignored in the model. The material properties are chosen to be linear elastic for computational efficiency. The following gives an overview of the model and details can be found in Krogh et al. (2019b).

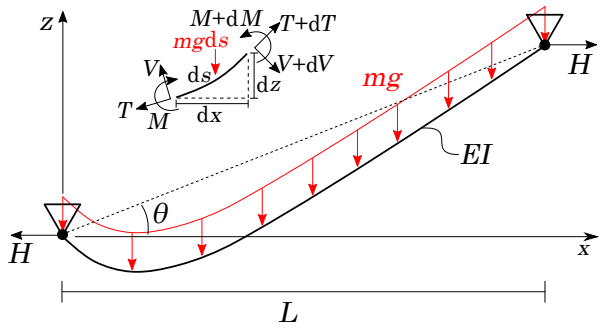

Fig. C.7: Free body diagram of cable with bending stiffness (Hsu and Pan, 2014).

C.3.1 2D Cables

The basis of the model is a 2D inextensible cable with bending stiffness or more generally, an *Euler elastica*. Accounting for large rotations, the force equilibrium on the infinitesimal cable segment in Figure C.7 can be used to set up a nonlinear differential equation (Hsu and Pan, 2014). In the figure, H is the horizontal component of the cable force T and M and V are the bending moment and shear force, respectively. EI is the flexural rigidity, and mg is the *weight per unit length*.

Assuming small sag (less than 1/4 of the span) such that the gravity load can be assumed uniformly distributed between the support points and also a linear curvature definition, a linearization can be carried out (Irvine, 1981). The linear differential equation becomes:

$$Hz''(x) - EIz''''(x) = \frac{mg}{\cos(\theta)} \tag{C.1}$$

Here θ is the tilt angle between the support points. A closed form solution can be obtained which predicts the z-coordinate of the cable as function of the x-coordinate, the material properties EI and mg, but also the horizontal component of the reaction force, H. Thereby, the arc length of the cable does not explicitly enter into the solution but rather, it depends on H. This matter is addressed later in this section.

Two different boundary conditions are used for the cable end points depending on the gripper to which it is attached: either a zero moment ($z'' = 0$) or a prescribed slope ($z' = s_{pre}$). The former is used with grippers attached to free ends of the ply where the slope is free. The latter is used to ensure C^1 continuity when multiple cables attach to the same gripper in the interior of the ply. Here, the value of s_{pre} needs to be determined. The prescribed slope boundary condition is also used to enforce the maximum gripper rotation of 40°.

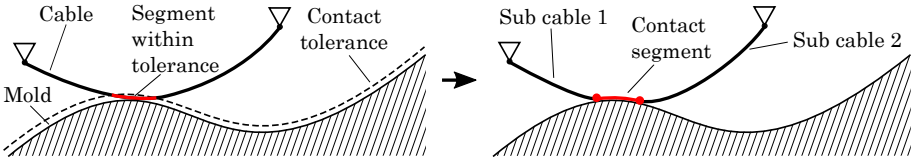

Fig. C.8: Contact formulation for cable model. Left: segment of cable is within contact tolerance. Right: contact segment is fixed and two sub cables are created.

The above description leaves two families of unknown variables for the model to be determined: the horizontal components of the reaction forces H and the prescribed slopes for shared grippers, s_{pre}. This determination is achieved by a minimization scheme, where the arc lengths of the cables are constrained to their prescribed lengths and the sum of squares of the reaction forces are minimized. Details can be found in Krogh et al. (2019b).

An advantage of the cable model is that it can easily be split into segments as mold contact occurs. The contact formulation employed is outlined in Figure C.8. A contact tolerance with respect to the mold surface is specified. In each iteration of the draping process, possible contact is evaluated. That is, if a portion of a cable is within the specified tolerance, that portion is considered in contact with the mold. Thereafter, it will be fixed on the mold surface and two independent sub cables are created. This contact formulation corresponds to an infinite friction condition which can be justified for the current material system by the tackiness of resin.

C.3.2 A Preliminary Numerical Result Highlighting the Challenges

By means of a 2D cable model with three grippers, the challenges with regard to trajectory generation pointed out in Section C.2.2 can be demonstrated. Consider a 160-mm long ply with the gripper attachment points located at the left end, halfway and at the right end of the ply. The initial gripper points have z-coordinates of 60 mm and x-coordinates of 5 mm, 80 mm and 155 mm, respectively. This configuration corresponds to the topmost gray dashed line (It. 1) in Figure C.9. The mold definition is provided in the appendix to the paper. The first target point is located at an x-coordinate of 5 mm, i.e. directly below the starting point of the leftmost gripper. The second and third target points are located 80 mm and 160 mm away, respectively, along the arc length of the mold. Notice, that the target points preserve the ply length on the mold surface. For this 2D example, the material properties are chosen to be $EI = 10^{-5}$ Nm^2 and $mg = 12$ N/m as it was found to provide a reasonable output. Material properties for the 3D cable model are treated in further detail in Section C.3.4.

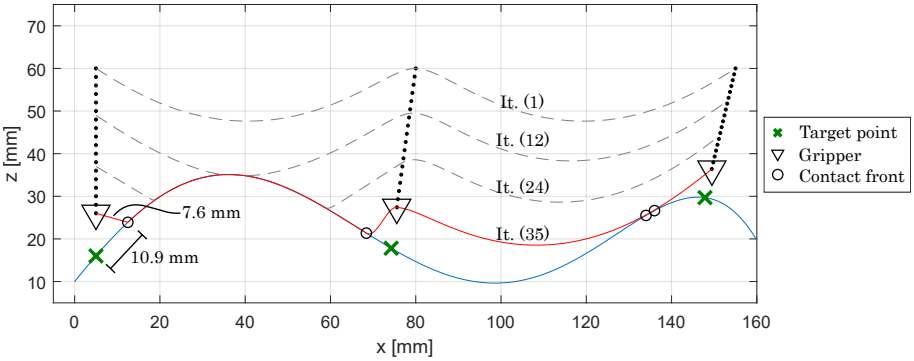

Fig. C.9: Draping of 2D ply onto mold with gripper trajectories prescribed as linear interpolations. The gray dashed lines show the ply in iterations 1, 12 and 24.

The grippers are moved by means of simple trajectories (black dots in Figure C.9) created as linear interpolations between the initial position and the target point of each gripper. Thereby, the grippers will in theory reach their target points, but as is evident from the following, it does not necessarily lead to an acceptable draped configuration. The ply is shown in iterations 1 (initial), 12 (upon first mold contact) and 24 as gray dashed lines and in the current iteration 35 in solid red line.

Although the grippers have not yet reached their target points, two issues can be identified in Figure C.9. First, the ply is not aligned on the mold with respect to the target points. For example, the distance from the leftmost target point to the leftmost mold-ply contact front is more than 3 mm larger than the corresponding free ply length. Second, two separate portions of the ply are in contact with the mold, i.e. for $x \in [12; 68]$ mm and $x \in [134; 136]$ mm, respectively. Because the arc length of the non-draped ply between the contact segments is larger than the corresponding arc length of the mold, this situation will eventually lead to a wrinkle. As a consequence, further gripper movement is meaningless in the absence of ply sliding on the mold. These defects are small but serve to illustrate the principle of an infeasible draping sequence.

C.3.3 3D Effects

As of now, only 2D cables has been considered. When modeling a 3D ply, some extra aspects must be taken into account. The basic idea is still to suspend cables between the grippers and in 3D, diagonal cables are also employed as sketched in Figure C.10 such that *unit cells* are created. The purposes of the diagonals are to improve the representation of the ply in the center of the unit cell and to account for *shearing* which was introduced in

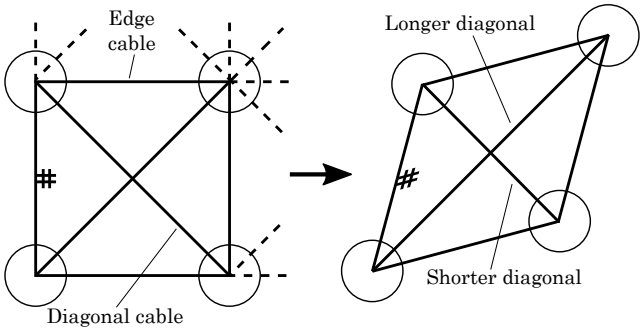

Fig. C.10: Assembly of cables into unit cells which can undergo shearing. Grippers are shown as circles but do not have any physical extent in the model. Fiber angles are indicated at the left edges.

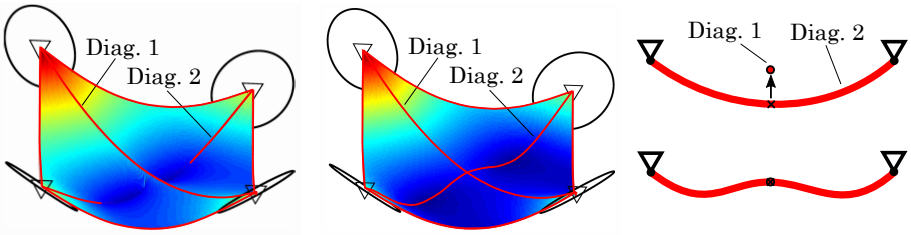

Fig. C.11: The postprocessing approach for ensuring continuity with the diagonals. Left: before postprocessing. Center: after postprocessing (diagonals are coincident). Right: 2D view of postprocessing.

Figure C.2. It is assumed that a unit cell behaves like a parallelogram, and the diagonals change their lengths accordingly. This behavior of the diagonals can appear counter-intuitive but notice that they do not represent actual fiber tows (See Figure C.10).

When the two diagonals are suspended across a unit cell, it does not necessarily follow that they will intersect. To ensure continuity in the model, a *post-processing* approach is adopted: the lowest diagonal is split up in two half segments which are re-evaluated such that the new center point is coincident with the highest diagonal. This approach is depicted in Figure C.11.

C.3.4 Cable Model Material Data

The ply material has a thickness and areal mass density of 0.3 mm and 314 g/m^2, respectively. The force-elongation response in the various deformation modes, i.e. fiber direction tension, in-plane shear and out-of-plane bending are nonlinear and rate-dependent. Here, the response is modeled as linear elastic.

The 2D cable model is based on the physical quantities “flexural rigid-

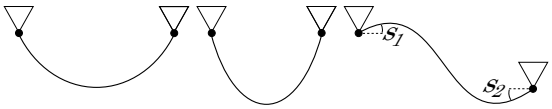

Fig. C.12: Different shapes of cable solutions. Left: cable under tension ($H > 0$). Middle: cable under compression (1st buckling mode, $H < 0$). Right: cable under compression with prescribed slopes (2nd buckling mode, $H < 0$).

ity" and "weight per unit length", but it is not obvious what values these parameters should assume. Both can be related to material properties and geometrical parameters, but this connection is not clear when the cables are assembled into 3D unit cells. Therefore, it was decided to use a least squares approach to match the cable model with a linear elastic FE model which is based on input from material tests (Krogh et al., 2017). Two compression tests with different out-of-plane rotation boundary conditions were simulated for a unit cell which yielded maximum deflections of approximately 29 mm. By considering the difference in the predicted displacement fields, EI and mg for the cable model were determined to $EI = 9 \cdot 10^{-5}$ Nm^2 and $mg = 12.26$ N/m. The norm of the residual vector was $3 \cdot 10^{-2}$ mm.

C.3.5 Behavior in Compression

Equation (C.1) is a differential equation of a general nature which allows the value of H (horizontal component of the reaction force) to assume both positive and negative values. When H is positive, corresponding to tension, the cable solution predicts a parabola-shaped sag (see the left of Figure C.12), where a lower value of H equals more sag. On the other hand, if H goes towards infinity, the cable solution will approach a straight line between the supports.

In compression, i.e. with H negative, the response is quite different. In fact, it corresponds to a buckling problem where multiple solutions, i.e. buckling modes, can have the same cable arc length. Upon comparing Equation (C.1) to the differential equations that are used to study buckling of Euler columns and beam-columns, it can be seen that they take the same form (Timoshenko and Gere, 1961). A cable with multiple solutions yielding the same length of 150 mm is illustrated in Fig C.13.

The fact that multiple solutions have the same length causes some issues when evaluating the cable model. In practice, higher modes are not physical because they correspond to unstable equilibria. Nevertheless, some buckling modes must be considered in the model. For instance, if slopes are prescribed as in the right of Figure C.12, the 2nd buckling mode can be a quite physical configuration.

To limit the number of possible length solutions, the critical loads, i.e.

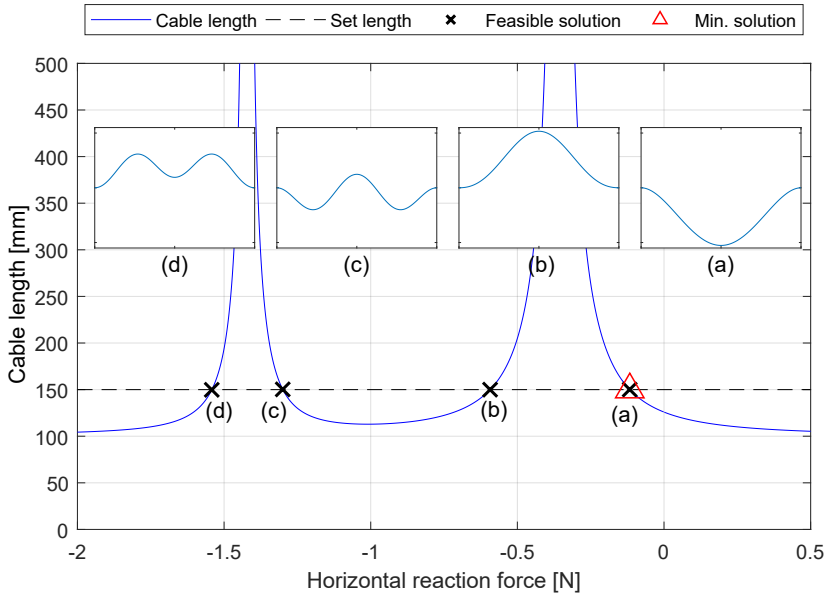

Fig. C.13: Cable length vs. horizontal reaction force for cable with 100 mm span and fixed end point rotations. Four values of the reaction force yield the sought length of 150 mm. The peaks located at -0.355 N and -1.42 N correspond to the singularities in the differential equation.

reaction forces that produce buckling can be determined and used as the lower bounds for the reaction forces in the cable model. The first critical load suffices in many cases but as stated above, the second critical load can also come into play. If the length of the cable computed with the first critical load is smaller than the prescribed length, then the second critical load must be used as the lower bound. This situation would be the case for the configuration to the right in Figure C.12.

For determining the critical loads, the classical Euler solutions are valid due to the similarity of the differential equations as noted above. The critical load H_{cr} depends on the mode number and the boundary conditions, but the equation takes the general form (Timoshenko and Gere, 1961):

$$H_{cr} = \frac{\alpha \beta \pi^2 EI}{L^2} \tag{C.2}$$

The values of α (mode number dependent) and β (boundary condition dependent) are given in Table. C.1. The flexural rigidity EI was determined in Section C.3.4, and the length L, as seen in Figure C.7, is the horizontal length between the supports. The reason why, the horizontal length must be used is that the differential equation for column buckling is derived for a straight column in the undeformed configuration, where the force is likewise parallel

Table C.1: Parameters α and β used in the Euler buckling Equation (C.2) (Timoshenko and Gere, 1961).

	Free-Free	Fixed-Fixed	Free-Fixed
1st mode	$\alpha = 1^2$	$\alpha = 1^2$	$\alpha = 1$
	$\beta = 1$	$\beta = 4$	$\beta = 2.046$
2nd mode	$\alpha = 2^2$	$\alpha = 2^2$	$\alpha = 2.72$
	$\beta = 1$	$\beta = 4$	$\beta = 2.046$

to the column. By using Equation (C.2) for the problem in Figure C.13, the critical reaction forces are predicted to be -0.355 N and -1.42 N respectively, which are identical to the values determined from the graph.

C.4 Optimization Setup

This section presents the optimization setup used for generating gripper trajectories. The criteria used for the incremental optimization approach from Figure C.5 are elaborated. The algorithm used for the optimization is the *SQP* (Sequential Quadratic Programming) from MATLAB's built-in function *fmincon*. This algorithm was chosen for its ease of implementation. In principle, any gradient-based optimization algorithm would work.

C.4.1 Optimization Criteria

The purpose of the optimization criteria is to guide the ply during draping in a manner which resembles manual layup as discussed in Section C.2.2. The observations from the preliminary 2D example in Section C.3.2 provide useful information as well. In the following, the optimization problem and criteria are presented in 2D and additions applicable to 3D are explained afterwards.

The draping sequence is split up into two parts: before mold contact and after mold contact. The former concerns the proper alignment of the ply using a seed point such that the ply border will eventually match the boundary. The latter concerns the wave movement where the ply is draped in directions away from the seed point.

From the 2D example in Figure C.9, it can be seen that the first mold-ply contact occurs at the highest point on the mold. This result makes sense because the ply is sagging. With this result in mind, a natural choice for the seed point on the mold, $\mathbf{S_{mold}}$, would indeed be the highest mold point. The corresponding point on the ply, $\mathbf{S_{ply}}$ which is to reach the mold seed point, can then be determined based on preservation of ply arc length on the mold. Thereby, the first objective is to minimize the distance between the

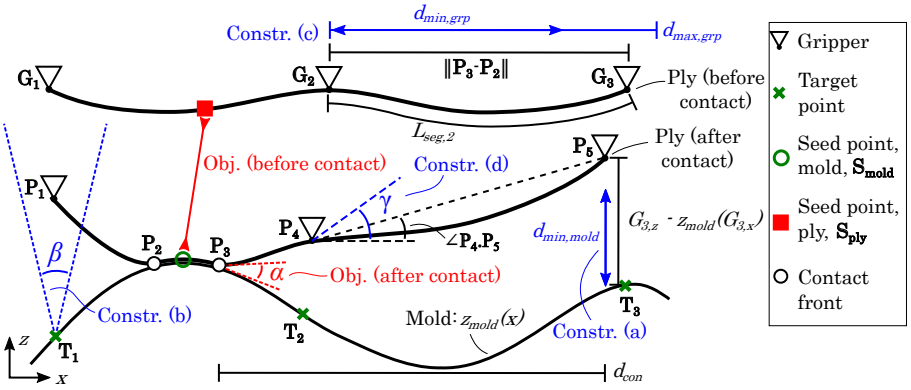

Fig. C.14: Graphical representation of objectives and constraints in optimization setup. For ease of viewing, each criterion is only shown once, but e.g. "Constr. (b)" applies for all target points.

aforementioned points. This criterion is depicted as "Obj. (before contact)" in Figure C.14. Notice, that any point on the mold could be chosen as the seed point.

Next, to advance the draping, the portions of the ply near the contact fronts are considered. Specifically, the angle between the mold and the ply in the contact fronts, α_i, are minimized. This criterion corresponds to "Obj. (after contact)" in Figure C.14.

The issue highlighted in the 2D example (Figure C.9) was multiple contact segments of the ply, which in general is likely to result in either wrinkling or bridging. In the optimization, it is alleviated by forcing the part of the ply which is not in proximity of the current contact fronts to remain some distance above the mold. Thereby it can be assured that only one contact segment will exist during draping. The constraints are implemented at the grippers, and the minimum distance above the mold is denoted $d_{\text{min,mold}}$, which is dependent on the distance to the contact point, d_{con} (elaborated later in the section). This condition is shown as "Constr. (a)" in Figure C.14.

To add robustness (and alignment during draping in 3D) an additional family of constraints is specified. "Constr. (b)" in Figure C.14 forces each gripper to remain inside an inverted triangle (cone in 3D) with the apex located at the corresponding target point. The criteria mentioned above serve to control the draping of the ply. In addition some criteria are implemented to keep the ply behavior within its physical limits:

- Penalization of mold-ply penetrations added as a term, Φ, to the objective function. Φ is a sum of all penetration distances.
- Constraints on the maximum and minimum distance between adjacent edge cable grippers. Because the fabric is virtually inextensible in the

fiber direction, gripper sliding could occur in practice, if the gripper distance exceeds the segment length. Also, too small a distance between grippers will result in excessive sagging which violates the cable model assumptions. This family of constraints is exemplified as "Constr. (c)" in Figure C.14.

- Constraints on the maximum inclination angle between adjacent edge cable grippers as seen in "Constr. (d)" in Figure C.14. These constraints serve to avoid extreme gripper positions which cannot be achieved by the robot tool.

The design variables of the problem, i.e. the gripper positions, are collected in the vector $\mathbf{G} = \{x_1, z_1, ..., x_{nGrp}, z_{nGrp}\}^{\mathrm{T}}$ where $nGrp$ denotes the number of grippers. For convenience, a double index notation is introduced where the first index $(1, ..., nGrp)$ denotes the gripper number and the second index (x, z) denotes the coordinate. Thus, $G_{2,x}$ corresponds to the x-coordinate of the 2nd gripper. On the other hand, if only the first index is specified, e.g. $\mathbf{G_j}$, the resulting quantity is the vector of coordinates for the jth gripper. When contact occurs, cables will be suspended between the contact fronts and the grippers as sketched in Figure C.8. The cable end points are thus obtained by augmenting $\mathbf{G}$ with the contact front points, whereby the vector $\mathbf{P}$ is obtained. Notice that $\mathbf{G}$ and $\mathbf{P}$ are equivalent before contact. The double index notation is also applied to $\mathbf{P}$ and the vector of target points $\mathbf{T}$. The optimization problem is formulated as follows:

$$
\begin{aligned}
\underset{\mathbf{G}}{\text{minimize}} \quad & \overbrace{||\mathbf{S_{mold}} - \mathbf{S_{ply}}||}^{\text{Before contact}} \quad \text{OR} \quad \overbrace{\sum_{i=1}^{nCon} \alpha_i}^{\text{After contact}} \quad + \Phi \\
\text{s.t.} \quad & (a)\ G_{j,z} - z_{\text{mold}}(G_{j,x}) \geq d_{\text{min,mold},j} \\
& (b)\ |G_{j,x} - T_{j,x}| \leq (G_{j,z} - T_{j,z}) \tan(\beta/2) \\
& (c)\ d_{\text{min,seg},k} \leq ||\mathbf{P_{k+1}} - \mathbf{P_k}|| \leq d_{\text{max,seg},k} \\
& (d)\ |\angle \mathbf{P_k}, \mathbf{P_{k+1}}| \leq \gamma \\
& \quad \forall j\ ,\ j = 1, ..., nGrp \\
& \quad \forall k\ ,\ k = 1, ..., nSeg
\end{aligned}
\tag{C.3}
$$

Here $nCon$, $nGrp$ and $nSeg$ are the number of contact fronts, number of grippers and number of cable segments, respectively, Φ is the mold-ply penetration penalty, and β and γ are the target point triangle and gripper inclination constraint angles, respectively (See Figure C.14). The quantity $d_{\text{min,mold,j}}$ from constraint (a) is calculated as follows:

$$
d_{\text{min,mold},j} = \min\left(d_{\text{con},j} c_{\text{dist,mold}}\ ,\ c_{\text{sat,mold}}\right) \tag{C.4}
$$

Thus, the vertical distance that the jth gripper must keep to the mold is its distance to the contact front $d_{\text{con},j}$ (see Figure C.14) scaled by a parameter $c_{\text{dist,mold}}$. Further, a saturation value of $c_{\text{sat,mold}}$ is specified. The quantities $d_{\text{min,seg,k}}$ and $d_{\text{max,seg,k}}$ in constraint (c) are calculated as follows:

$$d_{\text{min,seg},k} = c_{\text{min,seg}} L_{\text{seg},k} \tag{C.5}$$

$$d_{\text{max,seg},k} = c_{\text{max,seg}} L_{\text{seg},k} \tag{C.6}$$

Thus, the grippers must remain within a distance of each other defined by the segment arc length L_{seg} and two scaling parameters $c_{\text{min,seg}}$ and $c_{\text{max,seg}}$ which naturally must be defined according to $0 \leq c_{\text{min,seg}} \leq c_{\text{max,seg}} \leq 1$.

Notice that this formulation of constraints is efficient because it does not require the evaluation of the ply model. That is, the constraints only operate on $\mathbf{P}$. Common to all constraints is that they vanish when either the distance between a particular gripper and its target point or the length of the cable segment attached to the gripper is less than a tolerance, L_{tol}. The exception is constr. (c) where the parameter $c_{\text{max,seg}}$ is relaxed to unity. This unity state implies, that the corresponding cables are allowed to be fully stretched.

For 3D optimization problems, another horizontal coordinate, y, is included. Regarding the choice of seed point, the highest mold point is not a robust option because the corresponding point on the ply might not be defined. That is, the ply is only defined at the cables. Therefore, in 3D, the grippers and their corresponding target points are considered as possible seed points. Specifically, the highest target point that is also in a direction of shear on the mold is chosen. Mold contact of the seed point gripper will mark the transition to the wave motion draping.

In addition, the 3D alignment of the ply now requires more than just the seed point. For this purpose, the (up to four) grippers connected to the seed point gripper by edge cables, will act as "alignment grippers". Before contact of the seed point gripper, an alignment term is added to the objective function. This term is the sum of the horizontal distances between each alignment gripper and a line connecting the seed point with the target point of the corresponding alignment gripper.

Finally, shearing during alignment of the ply is not desired which is why it is penalized in the objective function before contact of the seed point gripper. After contact, a large difference between the diagonal gripper distances can cause sagging of one diagonal cable, e.g. as shown in Figure C.11. This sagging is mitigated by a penalization term added to the objective function when the vertical distance between the diagonal crossover point and the mold surface is less than a tolerance, $c_{\text{diag,sag}}$.

This section has presented an elaborate optimization scheme with a number parameters whose values must be specified. To this end, it should be

Table C.2: Common optimization settings for all examples in Section C.5. *ConTol* and *GrpTol* are the ply and gripper contact tolerances, respectively.

ConTol [mm]	*GrpTol* [mm]	$c_{\text{sat,mold}}$ [mm]	$c_{\text{max,seg}}$ [-]	γ [°]
0.3	0.35	50	0.99	35

Table C.3: Optimization settings used for 2D example in Figure C.15. ΔG is the move limit per iteration.

L_{tol} [mm]	ΔG [mm]	$c_{\text{dist,mold}}$ [-]	$c_{\text{min,seg}}$ [-]	β [°]
10	± 4	0.2	0.93	70

noted that all parameters have a physical meaning and that some parameters, e.g. γ, can be determined based on the specifications of the robot tool.

C.5 Numerical Results

This section presents numerical results with the cable model. Mold definitions can be found in the appendix to the paper. For visualization purposes in the 3D models, the grippers are drawn as circles, and a surface is interpolated in the unit cells, where the colors scale with the z coordinate. For the optimization examples, some common settings are given in Table C.2. These settings are believed to be generally applicable.

C.5.1 2D Optimization Example

Recall the 2D example from Section C.3.2 and Figure C.9 where a linear interpolation was employed as the trajectory for each gripper. This simple draping strategy resulted in multiple contact segments and possibly wrinkling. Consider now the same setup, but with the difference that the optimization scheme described previously is used to determine the trajectories of the grippers. The result is shown in Figure C.15. From this figure, it can be seen that the ply is draped in a wave movement as desired. Only one contact segment exist throughout the draping and the grippers are within half a millimeter of their respective target points in the draped configuration. The optimization settings used for this result are provided in Table C.3.

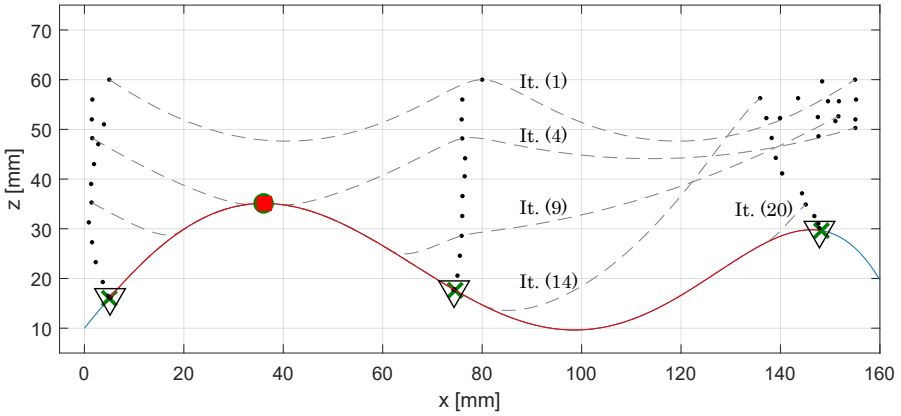

Fig. C.15: Draping of 2D ply onto mold with gripper trajectories generated from optimization. The gray dashed lines show the ply in iterations 1, 4, 9, 14 and 20. The red line shows the ply in the final iteration 24.

C.5.2 Validation of 3D Cable Model

As a validation of the cable model and in particular its ability to account for shearing, consider the example in Figure C.16. The example is a comparison between the cable model and the non-linear rate-dependent FE model from Krogh et al. (2019a). The latter will be the baseline for the comparison. The setup concerns draping of a 300 mm by 150 mm ply onto a flat parallelogram-shaped mold where the mold shear angle is 20°. The gripper trajectories are prescribed linear interpolations from the initial gripper positions to the respective target points. The draping time is 10 s, which is a reasonable time for the robot system. Recall though, that the cable model is time-independent.

Figures C.16 (a) and (b) show the initial configurations with the ply suspended 40 mm above the mold and with gripper (1,1) located directly above its target point. The initial grid spacing of the 300 mm by 150 mm ply is 148 mm which is why both models exhibit sag. The deformation field is slightly different between the two models, and this difference is a result of the difference between the gripper boundary conditions in the respective models. However, the maximum vertical displacement is only overpredicted by 2.5 mm by the cable model. Figures C.16 (c) and (d) present the results at 10% of the draping sequence. The ply is now beginning to shear while there is still some slack in the fiber directions. This shearing induces the diagonal waves. Finally, Figures C.16 (e) and (f) present the results at 75% of the draping sequence. The diagonal waves are now more distinct than at the 10% state. Due to these waves, both models predict small diagonal wrinkles in the draped

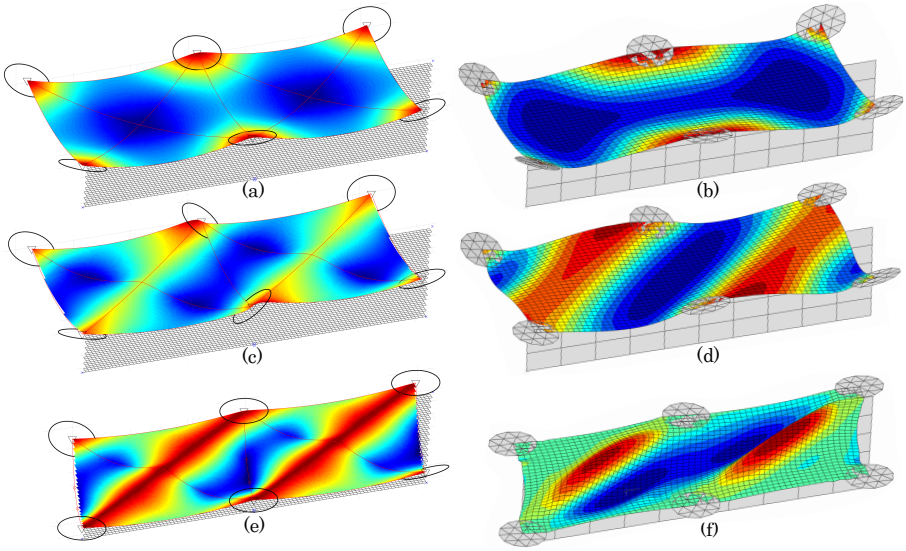

Fig. C.16: Draping onto flat parallelogram mold with cable model ((a), (c) and (e)) and FE model ((b), (d) and (f)). The rows correspond to the initial configuration, 10% done and 75% done respectively.

configuration. Based on the comparison of the two models, it is concluded that the cable model can give predictions of the displacement field of the ply during draping that are comparable to the FE approach.

C.5.3 3D Optimization Example 1

The first 3D example is shown in Figure C.17 and involves a grid of 2×2 grippers draping a ply onto a region of the mold surface with low and primarily convex curvature. In this region, the minimum positive and negative radii of curvature are 320 mm and -148 mm, respectively. The initial configuration is presented in Figure C.17 (a) where the seed point gripper (1,1) is located 50 mm above its target point. Contact with the seed point is established in Figure C.17 (b) and hereafter the drape movement follows a wave in a direction towards gripper (2,2) as seen in Figure C.17 (c)-(f). In the draped configuration the ply is positioned such that the grippers are within 1.8 mm of their target points. The optimization settings used for this example are provided in Table C.4.

C.5.4 3D Optimization Example 2

The second 3D example is presented in Figure C.18 and involves a grid of 3×2 grippers. In this example, the chosen region of the mold has a higher

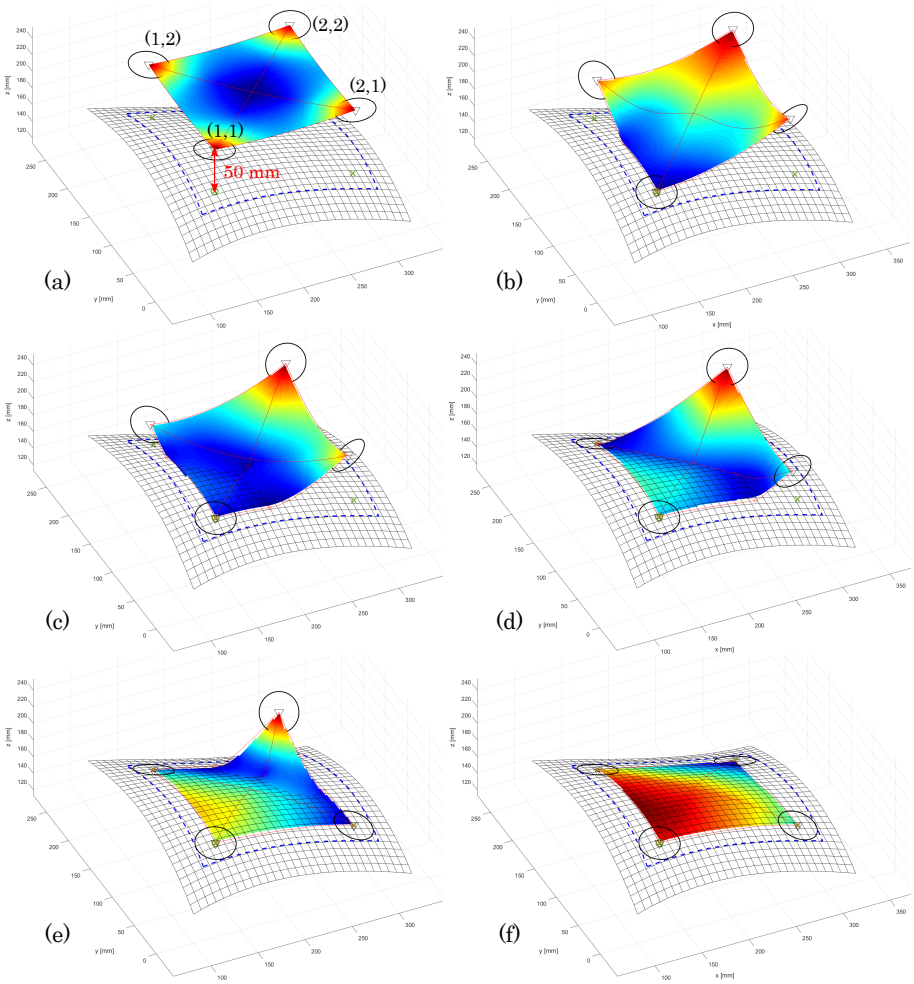

Fig. C.17: Draping of ply with a 2 × 2 gripper grid onto mold. Iterations 1, 12, 17, 26, 34 and 56 are presented in (a)-(f). The blue dashed line indicate the prescribed boundary.

Table C.4: Optimization settings used for 3D examples in Figure C.17 and C.18. ΔG is the move limit per iteration.

L_{tol} [mm]	ΔG [mm]	$c_{\text{dist,mold}}$ [-]	$c_{\text{min,seg}}$ [-]	β [°]	$c_{\text{diag,sag}}$ [mm]
20	±5	0.25	0.96	35	15

curvature than in 3D Example 1 with the minimum positive and negative radii of curvature equal to 175 mm and -144 mm, respectively. In addition,

it is a more difficult problem than 3D Example 1 because it contains convex and concave regions. In Figure C.18 (a), the ply is in the initial configuration with the seed point gripper (2,1) located 50 mm above the seed point, and in Figure C.18 (b) the seed point gripper has reached the mold surface. Figures C.18 (c)-(e) present three intermediate iterations where the grippers in the left unit cell progressively make contact with the mold. Figure C.18 (f) is the final draped configuration where the grippers are located within 2 mm of their target points. The ply is in contact with the mold surface everywhere except for the concave region near gripper (3,2). Here the ply is bridging with a maximum distance to the mold of 3 mm. This issue of bridging is revisited in the Discussion section. The optimization settings are the same as in the

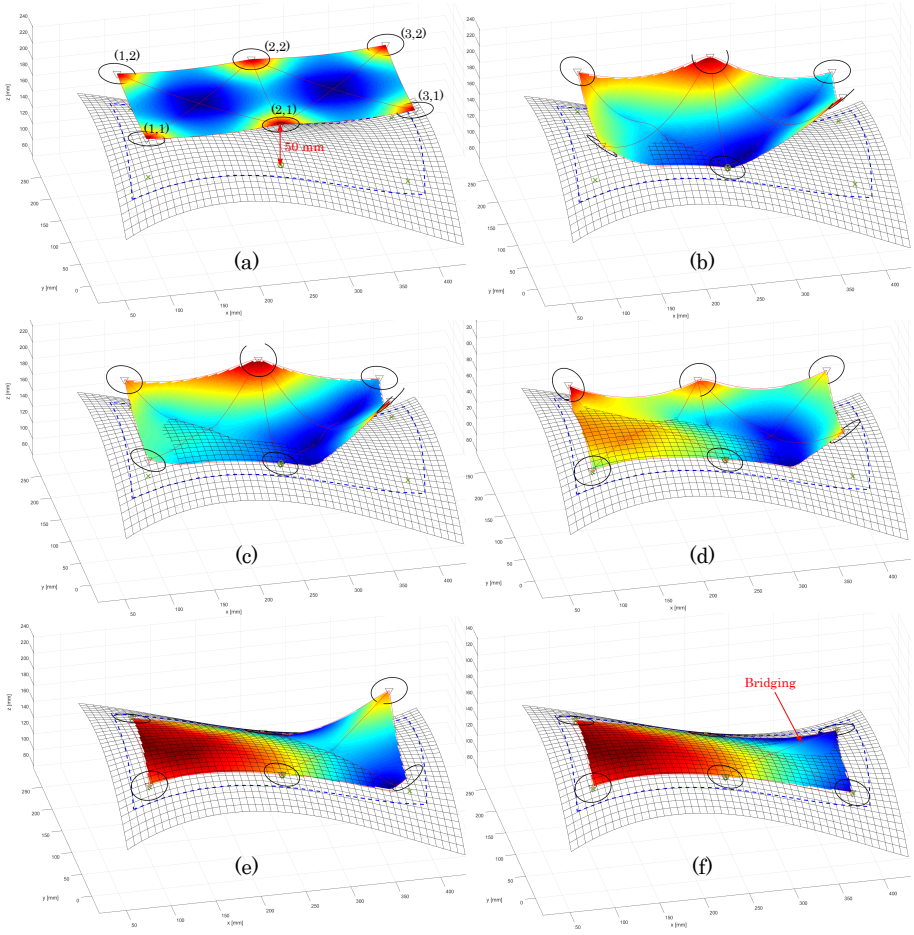

Fig. C.18: Draping of ply with a 3 × 2 gripper grid onto mold. Iterations 1, 13, 23, 36, 47 and 60 are presented in (a)-(f). The blue dashed line indicate the prescribed boundary.

previous example, i.e. as given in Table C.4.

C.6 Discussion

The results in the preceding section show promise in terms of generation of feasible gripper trajectories. The quality requirement of close conformity to the mold surface was, however, not fulfilled in the second 3D example (Figure C.18). A number of remedies to this situation exist. Because the bridging portion of the ply is in a diagonal direction, the ply can be stretched locally via an increase in shear. Therefore, the bridging portion could maybe be put onto the mold by means of a push from a gripper subsequent to draping. Another solution would be to use a smaller grid spacing or, if the grid is non-rectangular, make sure that a gripper is located in this particular spot on the mold. A final solution is to pre-shear the ply which could be achieved either when the ply has been picked by the robot or in a preceding operation.

The optimization approach presented in this study involves some settings that define the "tightness" of the constraints. To that end, some degree of tuning could be necessary when considering a new draping problem. Yet, the settings have a direct physical meaning which aids the process. For instance, if multiple contact segments develop during draping, the parameter $c_{\text{dist,mold}}$ from Equation (C.4) must be increased. In a future study, it could be investigated if the settings can be changed adaptively during the iterations: with the occurrence of multiple contact segments, the program can jump back a few iterations, change settings and then continue.

Other improvements to the present implementation include the use of a cable model accounting for large displacements and curvatures as well as having the ability to model non-rectangular ply shapes. For the former, an increase in computational time is expected which must be assessed with regard to the increase in accuracy. The latter is important for implementation in an industrial context.

Lastly, an interesting discussion is that of optimal vs. feasible gripper trajectories. Even though optimization is utilized in this study, it is far from certain that the generated gripper trajectories are optimal. Of course, "optimality" would have to be precisely defined. Nonetheless, because the optimization is merely used to incrementally fulfill the defined criteria and the problem is path dependent, the combined trajectory is likely not to be optimal.

C.7 Conclusion

This paper has presented an approach to generation of feasible gripper trajectories for an automatic composite draping system. The grippers of the robot

end effector can be controlled in the three translational degrees of freedom, and these movements must be determined such that the draped ply conforms closely to the mold surface and is placed inside a prescribed boundary.

The study takes as its starting point an approximate ply model based on cables suspended between the grippers. The cable model is able to take large deflections, mold contact and fabric shearing into account. The cable model was validated against a non-linear rate-dependent finite element (FE) model based on material test data. It was concluded that the cable model can predict the ply displacement field nearly as well as the computationally more expensive FE model.

The optimization routine is split up into two parts. First, a seed point on the ply must reach its corresponding point on the mold while ensuring proper alignment of the ply. Thereby, mold contact is established. Next, the ply is draped away from the seed point my minimizing the difference in angles between the ply and the mold in the contact fronts. Constraints are included to ensure that only one contact segment exists. This draping strategy is chosen to mimic manual layup. In addition, a number of optimization criteria are implemented to make sure that the ply is moved within its physical limits.

The numerical results show that the optimization approach can determine a draping sequence such that the quality requirements can be met. Minor misalignment and bridging was observed, but it is believed that these matters can be taken into account when transforming the output from the optimization routine to actual robot sequences. The latter is necessary when the results from this study will be validated in practice.

Acknowledgements

The research presented in this paper is part of the FlexDraper research project. The authors wish to thank the Innovation Fund Denmark (grant no. 5163-00003B) for the support.

References

Björnsson A, Jonsson M, Johansen K (2017) Automated material handling in composite manufacturing using pick-and-place systems – a review. Robotics and Computer-Integrated Manufacturing 51:222–229, DOI 10.1016/j.rcim.2017.12.003

Brinker J, Prause I, Kosse P, Früh HC, Printz S, Henke C, Hüsing M, Corves B, Schmitt R, Gries T, Jeschke S (2017) Automated handling and draping of reinforcing textiles-challenges and developments. In: Mechanisms and Machine Science, vol 46, pp 485–493, DOI 10.1007/978-3-319-45450-4_49

Coutandin S, Brandt D, Heinemann P, Ruhland P, Fleischer J (2018) Influence of punch sequence and prediction of wrinkling in textile forming with a multi-punch tool. Production Engineering 12(6):779–788, DOI 10.1007/s11740-018-0845-9

Eckardt M, Buchheim A, Gerngross T (2016) Investigation of an automated dry fiber preforming process for an aircraft fuselage demonstrator using collaborating robots. CEAS Aeronautical Journal 7(3):429–440, DOI 10.1007/s13272-016-0199-y

Eischen JW, Kim YG (1993) Optimization of Fabric Manipulation during Pick/Place Operations. International Journal of Clothing Science and Technology 5(3-4):68–76, DOI 10.1108/eb003021

Flixeder S, Glück T, Kugi A (2017) Force-based cooperative handling and lay-up of deformable materials: Mechatronic design, modeling, and control of a demonstrator. Mechatronics 47:246–261, DOI 10.1016/j.mechatronics.2016.10.003

Hsu Y, Pan C (2014) The static WKB solution to catenary problems with large sag and bending stiffness. Mathematical Problems in Engineering 2014:1–11, DOI 10.1155/2014/231726

Irvine HM (1981) Cable Structures. MIT Press

Krogh C, Glud JA, Jakobsen J (2017) Modeling of prepregs during automated draping sequences. In: AIP Conference Proceedings, AIP Publishing, vol 1896, p 030036, DOI 10.1063/1.5008023

Krogh C, Glud JA, Jakobsen J (2019a) Modeling the robotic manipulation of woven carbon fiber prepreg plies onto double curved molds: A path-dependent problem. Journal of Composite Materials 53(15):2149–2164, DOI 10.1177/0021998318822722

Krogh C, Jakobsen J, Sherwood JA (2019b) Development of a Computationally Efficient Fabric Model for Optimization of Gripper Trajectories in Automated Composite Draping. In: EngOpt 2018 Proceedings of the 6th International Conference on Engineering Optimization, Springer International Publishing, Cham, pp 1107–1118, DOI 10.1007/978-3-319-97773-7_96

Lin H, Wang J, Long A, Clifford M, Harrison P (2007) Predictive modelling for optimization of textile composite forming. Composites Science and Technology 67(15-16):3242–3252, DOI 10.1016/j.compscitech.2007.03.040

Lin H, Clifford M, Taylor P, Long A (2009) 3D mathematical modelling for robotic pick up of textile composites. Composites Part B: Engineering 40(8):705–713, DOI 10.1016/j.compositesb.2009.07.006

Molfino R, Zoppi M, Cepolina F, Yousef J, Cepolina EE (2014) Design of a Hyper-flexible cell for handling 3D Carbon fiber fabric. Recent Advances in Mechanical Engineering and Mechanics pp 165–170

Nagele L, Macho M, Angerer A, Hoffmann A, Vistein M, Schonheits M, Reif W (2015) A backward-oriented approach for offline programming of complex manufacturing tasks. In: ICARA 2015 - Proceedings of the 2015 6th International Conference on Automation, Robotics and Applications, pp 124–130, DOI 10.1109/ICARA.2015.7081135

Newell GC, Khodabandehloo K (1995) Modelling Flexible Sheets for Automatic Handling and Lay-up of Composite Components. Proceedings of the Institution of Mechanical Engineers, Part B: Journal of Engineering Manufacture 209(62):423–432, DOI 10.1243/pime_proc_1995_209_106_02

Reinhart G, Ehinger C (2013) Novel Robot-Based End-Effector Design for an Automated Preforming of Limb Carbon Fiber Textiles. In: Future Trends in Production Engineering, Springer Berlin Heidelberg, Berlin, Heidelberg, pp 131–142, DOI 10.1007/978-3-642-24491-9

Timoshenko SP, Gere JM (1961) Theory of Elastic Stability, 2nd edn. McGraw-Hill Book Company: New York

Van Der Weeën F (1991) Algorithms for draping fabrics on doubly-curved surfaces. International Journal for Numerical Methods in Engineering 31(7):1415–1426, DOI 10.1002/nme.1620310712

Zhu B, Yu T, Zhang H, Tao X (2008) Experimental investigation of formability of woven textile composite preform in stamping operation. International Journal of Material Forming 1(SUPPL. 1):969–972, DOI 10.1007/s12289-008-0219-5

Appendix: Mold definitions

The 2D mold surface used in Figure C.9, Section C.3.2 and Figure C.15, Section C.5.1 is given by the following 5th order polynomial:

$$z_{\text{mold}}(x) = -17113x^5 + 5413x^4 - 440x^3 - 5.45x^2 + 1.24x + 0.01 \qquad \text{(C.7)}$$

Here $x \in [0, 0.16]$. The 3D mold surface used in 3D Example 1 in Figure C.17, Section C.5.3 and 3D Example 2 in Figure C.18, Section C.5.4 is defined by a 3rd degree polynomial surface:

$$\begin{aligned} z_{\text{mold}}(x, y) = 1.004x + 1.089y - 3.667x^2 - 4.4x\,y - \\ 3.75y^2 + 3.086x^3 + 8.889x^2\,y + 4.321y^3 \end{aligned} \qquad \text{(C.8)}$$

Table C.5: Target points for 3D examples.

Example #	1	2
Target Point 1,1	$\{0.1477, 0.0522, 0.1832\}$ m	$\{0.0956, 0.0504, 0.1755\}$ m
Target Point 2,1	$\{0.2948, 0.0522, 0.1577\}$ m	$\{0.2440, 0.0528, 0.1720\}$ m
Target Point 1,2	$\{0.1502, 0.1992, 0.1707\}$ m	$\{0.1081, 0.1967, 0.1800\}$ m
Target Point 2,2	$\{0.2961, 0.1984, 0.1357\}$ m	$\{0.2539, 0.1979, 0.1450\}$ m
Target Point 3,1	-	$\{0.3877, 0.0608, 0.1303\}$ m
Target Point 3,2	-	$\{0.4017, 0.2084, 0.1270\}$ m

Here $x \in [0, 0.45]$, $y \in [0, 0.45]$. The target points used with the mold are presented in Table C.5. The target points have been calculated using the kinematic mapping algorithm.

ISSN (online): 2446-1636
ISBN (online): 978-87-7210-514-7

AALBORG UNIVERSITY PRESS